INNOVATIVE HYBRID COMPOSITE NANOMATERIALS

A DISSERTATION SUBMITTED TO
THE GRADUATE SCHOOL OF ENGINEERING AND SCIENCE
OF BILKENT UNIVERSITY
IN PARTIAL FULFILLMENT OF THE REQUIREMENTS FOR
THE DEGREE OF
DOCTOR OF PHILOSOPHY
IN
MATERIALS SCIENCE AND NANOTECHNOLOGY

By
Zeliha Soran Erdem
September 2016

INNOVATIVE HYBRID COMPOSITE NANOMATERIALS

By Zeliha Soran Erdem

September 2016

We certify that we have read this dissertation and that in our opinion it is fully adequate, in scope and in quality, as a dissertation for the degree of Doctor of Philosophy.

Hilmi Volkan Demir(Advisor)

Dönüş Tuncel

Emrah Özensoy

Menemşe Gümüşderelioğlu

Adil Denizli

Approved for the Graduate School of Engineering and Science:

Ezhan Karaşan
Director of the Graduate School

ABSTRACT

INNOVATIVE HYBRID COMPOSITE NANOMATERIALS

Zeliha Soran Erdem
Ph.D. in Materials Science and Nanotechnology
Advisor: Hilmi Volkan Demir
September 2016

Digital lighting and bio-imaging are two emerging crucial research fields. Nanotechnology stands in the center of these applications by providing nano-scale particles possessing large surface-to-volume ratios, high efficiency, and low toxicity while allowing for functionalization, efficient quality lighting and improved biocompatible bio-imaging. Some of the frequently employed nanoparticles in optoelectronics and imaging are colloidal semiconductor quantum dots, colloidal conjugated polymer nanoparticles, and colloidal iron oxide nanoparticles, all of which we have studied using colloidal approaches to make hybrid composites for lighting and imaging in this thesis.

Fluorescent inorganic nanoparticles of colloidal quantum dots (QDs) attract significant interest for many optoelectronic and biomedical applications. Although they possess numerous advantages including broad absorption band, high quantum yield, and narrow emission spectrum, there are serious concerns on their recycling due to their cadmium-based composition. Alternatively, relatively low toxic organic fluorescent polymer nanoparticles or oligomer nanoparticles have stepped forward. However, their reduced emission efficiency and stability in solid state is an important limitation for their use in wide-spread solid-state lighting applications. To address these problems, in the first part of this thesis, we proposed and demonstrated the design of new hybrid composite material systems of oligomer nanoparticles to be used in solid-state lighting. We first showed that the emission efficiency and stability of the oligomer nanoparticles in solid state are significantly improved based on our proposed crystallization technique. Here, using this simple and low-cost approach, oligomer nanoparticle monoliths were obtained from the powders of these crystals.

Despite the disadvantages of using QDs, their high quantum efficiency and narrow-band emission still make them a valuable asset for solid-state lighting. However, the decrease in solid-film efficiencies is still an important issue to be addressed. With this perspective, in this thesis we utilized the incorporation

of QDs into crystalline matrices allowing for the nonradiative energy transfer (NRET) to improve the emission capability of the nano-emitters. Since it is an interesting crystalline semiconductor organic molecule, we employed anthracene as the host donor medium and incorporated the quantum dots being exciton acceptors. Here, we systematically investigated the NRET from each anthracene emission peak to QDs and demonstrated the use of this composite system on LEDs as color converters and the polarization ratio change of quantum dots within this crystal system.

Magnetic resonance imaging (MRI), for which we also developed colloidal contrast agents using nanoparticles (NPs) as the second part of this thesis, is a powerful diagnostic tool providing good soft tissue contrast and high spatial resolution. It produces T_1- and T_2-weighted images, in which the region of interest is observed as brighter and darker contrast, respectively. Superparamagnetic iron oxide (IO) NPs are an important member of T_2-weighted contrast agents possessing low toxicity. However, they suffer from poor anatomic details due to their darker contrast. Therefore, combining T_1- and T_2-weighted features in a single IO NP (dual-modal contrast) is a major step for improving MRI contrast. In order to meet the requirement for dual-modal contrast agents, which possess both T_1- and T_2-weighted imaging capability, in this thesis we synthesized highly monodisperse superparamagnetic cubic IO NPs. Magnetic characterizations along with in vivo MRI experiments demonstrated that these nanoparticles hold great promise for dual-modal imaging. This increased dual-modal effect without paramagnetic material doping or decreasing the size of nanoparticles smaller than 5 nm directed us to understand the relation of the T_1 and T_2 relaxations depending on the IO NP size and shape. Here, we showed the presence of intrinsic paramagnetic phase in magnetite IO NPs. Moreover, we demonstrated that this contribution is higher in IO NPs possessing cubic shape compared to the spherical counterparts, which explains the increased dual-modal effect in the monodisperse superparamagnetic nanocubes.

Keywords: Oligomer nanoparticles, quantum dots, light-emitting diodes (LEDs), nonradiative energy transfer, superparamagnetic iron oxide nanoparticles (SPIONs), magnetic resonance imaging (MRI).

ÖZET

YENİLİKÇİ HİBRİT KOMPOZİT NANOMALZEMELER

Zeliha Soran Erdem
Malzeme Bilimi ve Nanoteknoloji, Doktora
Tez Danışmanı: Hilmi Volkan Demir
Eylül 2016

Dijital aydınlatma ve biyogörüntüleme gelişmekte olan önemli araştırma alanlarındandır. Nanoteknoloji, sunduğu geniş yüzey/hacim oranına sahip, yüksek verimlilikli ve düşük toksisiteye sahip nanoboyuttaki parçacıkların yanı sıra fonksiyonelleşmeyi, verimli kaliteli aydınlatmayı ve gelişmiş biyouyumlu görüntülemeyi mümkün kılması nedeniyle bu uygulamaların merkezinde bulunmaktadır. Optoelektronik ve görüntüleme alanlarında sıklıkla kullanılan, aynı zamanda tümü bu tez kapsamında aydınlatma ve görüntüleme için kolloid yaklaşımlar kullanılarak geliştirilen hibrit kompozitlerde çalışılan nanoparçacıklar (NP) arasında kolloidal yarıiletken kuvantum noktacıklar (KN), kolloidal konjuge polimer nanoparçacıklar ve kolloidal demir oksit nanoparçacıklar (DO NP) yer almaktadır.

Işıyan inorganik nanoparçacıklar olarak kolloidal KN'ler, birçok optoelektronik ve biyomedikal uygulamalar için oldukça ilgi çekicidir. Bu yapılar, geniş soğurma bandı, yüksek kuvantum verimliliği ve dar ışıma spektrumu gibi birçok avantaja sahip olmalarına rağmen, kadmiyum içerikli yapıları nedeniyle geri dönüşümleri için ciddi endişeler barındırmaktadırlar. Alternatif olarak, göreceli olarak daha az toksik yapıdaki ışıyan polimer nanoparçacıklar veya oligomer nanoparçacıklar öne çıkmaktadır. Ancak, katı fazda azalan ışıma verimlilikleri ve dayanıklılıkları, bu malzemelerin yaygın katı hal aydınlatma uygulamalarında kullanımları için büyük bir engel teşkil etmektedir. Bu problemlere çözüm olarak bu tezin ilk kısmında, katı hal aydınlatmada kullanımları için oligomer nanoparçacıkların yeni hibrit kompozit malzeme sistem tasarımlarını önerdik ve gösterdik. İlk olarak, önermiş olduğumuz kristalizasyon yöntemi ile katı haldeki oligomer nanoparçacıkların ışıma verimliliklerinin ve dayanıklılıklarının istatistiksel olarak anlamlı derecede arttığını gösterdik. Burada, bahsi geçen basit ve ucuz yaklaşım ile oligomer nanoparçacık yekpare taşlar, bu kristallerin tozlarından oluşturulmuştur.

Kuvantum noktacıkların kullanımındaki birtakım dezavantajlara rağmen, yüksek kuvantum verimlilikleri ve dar bant ışımaları, bu malzemeleri katı hal

aydınlatma için halen çok değerli kılmaktadır. Ancak, düşük katı film verimlilikleri, halen üzerinde durulması gereken önemli bir problemdir. Bu bakış açısıyla, bu tezde, nanoışıyıcıların ışıma kapasitelerinin artırılması amacıyla ışınımsız enerji transferine izin veren KN yüklenmiş kristal matrislerden yararlandık. Antrasin ilginç bir kristal yarıiletken organik molekül olduğu için antrasini mesken verici ortam olarak ve kristale gömülen KN'leri ise eksiton alıcı olarak kullandık. Burada, antrasin ışıma tepelerinin her birinden kuvantum noktacıklara olan ışınımsız enerji transferini sistematik olarak inceledik. Ayrıca, hazırlanan bu kompozit sistemin ışık yayan diyotlar (LEDs) üzerinde renk dönüştürücü olarak kullanımını ve KN'lerin bu kristal sistemi içerisindeki polarizasyon oranlarının değişimlerini de gösterdik.

Bu tez çalışmasının ikinci kısmında, kolloidal nanoparçacıkları kullanarak kontrast malzemesini geliştirdiğimiz manyetik rezonans görüntüleme (MRG), iyi bir yumuşak doku kontrastı sağlayan ve yüksek üç boyutlu çözünürlüğe sahip güçlü bir tanısal cihazdır. Bu yöntem, ilgilenilen bölgenin daha aydınlık görünmesini sağlayan T_1- veya daha karanlık görünmesini sağlayan T_2-ağırlıklı görüntüler oluşturmaktadır. Süperparamagnetik DO NP'ler, T_2-ağırlıklı kontrast ajanlarının önemli bir üyesi olup, düşük toksisite özelliğine sahiptir. Ancak, oluşturdukları karanlık kontrast nedeniyle anatomik detayların ayırt edilmesi konusunda ciddi problemlere neden olmaktadırlar. Bu nedenle, T_1- ve T_2-ağırlıklı özelliklerin tek bir DO üzerinde birleştirilmesi (çift-modlu kontrast) MRG için önemli bir gelişmedir. T_1- ve T_2-ağırlıklı görüntüleme yeteneğine sahip çift-modlu kontrast ajanlarına duyulan gereksinimi karşılamak amacıyla, bu tezde yüksek tekil dağılımlı süperparamagnetik küp DO NP'ler sentezledik. In vivo MRG deneyleriyle birlikte yürüttüğümüz manyetik karakterizasyon çalışmaları, bu nanoparçacıkların çift-modlu görüntüleme için umut vaat edici özelliklere sahip olduğunu gösterdi. Paramagnetik malzemelerin yüklenmesi veya nanoparçacık boyutunun 5 nm altında olacak şekilde küçültülmesi gibi yaklaşımlar kullanılmadan görülen bu çift-modlu görüntüleme etkisindeki artış, bizi T_1 ve T_2 relaksasyonlarının DO NP'lerinin boyutuna ve şekline bağlı ilişkisini araştırmaya yöneltti. Bu çalışmada, magnetit DO NP'lerin kendiliğinden içlerinde barındırdıkları bir paramagnetik faz olduğunu bulduk. Ayrıca, bu paramagnetik katkının küp yapıdaki nanoparçacıklarda küre şeklindekilere kıyasla daha fazla olduğunu ve tekil dağılıma sahip süperparamagnetik nanoküplerde de bu nedenle çift-modlu görüntüleme etkisinin daha kuvvetli görüldüğünü gösterdik.

Anahtar sözcükler: Oligomer nanoparçacıklar, kuvantum noktacıklar, ışık yayan diyotlar (LEDs), ışınımsız enerji transferi (NRET), süperparamagnetik demir oksit nanoparçacıklar (SPIONs), manyetik rezonans görüntüleme (MRG).

Acknowledgement

It has been a long journey for me, which becomes sometimes very hard and backbreaking, and sometimes very enjoyable, great and thankful. I have met many people contributing to my scientific and social life throughout my PhD thesis work. I want to thank all of them with all my heart.

First, I would like to acknowledge my advisor Prof. Hilmi Volkan Demir. I have always felt his support and guidance during my PhD work. I have learnt from him the importance of being professional in every aspect of life. I will always take his optimistic way, kind attitude and guidance as a role model in my life. In addition, I would like to thank Prof. Dönüş Tuncel for her support and for the valuable collaboration we had. I would also like to thank Prof. Emrah Özensoy for his support. I owe many thanks to Prof. Menemşe Gümüşderelioğlu and Prof. Adil Denizli for accepting to be in my thesis committee. It is a pleasure for me to start my academic career with Prof. Menemşe Gümüşderelioğlu and again to be together with her in this important step of my life.

I am also thankful to the past and present members of Demir Group. I always feel their help and support and will never forget the great times that we had together. First, I would like to thank Talha Erdem, Vijay Kumar Sharma, Akbar Alipour and Pedro Ludwig Hernandez Martinez for their grateful performance in various studies. Next, I would like to thank other group members that my way crossed: Ozgun Akyuz, Emre Unal, Prof. Emre Sari, Can Uran, Burak Guzelturk, Aydan Yeltik, Sayim Gokyar, Veli Tayfun Kilic, Kivanc Gungor, Shahab Akhavan, Yusuf Kelestemur, Prof. Nihan Kosku Perkgoz, Prof. Urartu Ozgur S. Seker, Manoj Sharma, Ashma Sharma, Murat Olutas, Savas Delikanli, Didem Dede, Nima Taghipour, Onur Erdem, Mehmet Zafer Akgul, Berkay Bozok, Halil Akcali, Ibrahim Akcali, Can Firat Usanmaz, and Ahmet Mesut Alpkilic. It was a pleasure for me to work with you. In addition, I would also like to thank Dr. Marcus Adam and Dr. Nikolay Gaponik from TU Dresden for the excellent collaboration we had.

Next, my special thanks is for my husband Talha who makes my life more beautiful and colorful. I would like to thank him for his love, patience and support in every aspect of my life. To share both professional and unprofessional

life with him was very funny and valuable for me. I love you so much, I know that this finish line is a new starting point for both of us which will bring more happiness :)

I also owe special thanks to my family. They always have supported me and my decisions, and truly guided me whenever I'm lost... My mom and dad, thanks a lot for your love, support and guidance. My brothers Serdar and Ahmet, you have been always close to me despite the long distance we have, thank you. My sister İffet, you deserve special thanks for your friendship, support, and sacrifice; thanks for your presence. And finally one of my cute nephews, Ömer Batu, my bead, your smile is enough to absorb all of my stress everytime and you made everything easier :)

Since this thesis cannot be completed without their help, I dedicate this thesis to my love Talha and my family...

Contents

List of Figures

List of Tables

Chapter 1
Introduction

Being at the interface of physics, chemistry, biology, and engineering, materials science has always been an integral part of our civilization. The science of materials address important problems of the human kind. With this perspective, during this graduate study we have used the tools of the materials science to study two fundamentally different problems. The first one that we have worked on during this time frame is related to the need for high-quality, high-efficiency light-emitting devices. Considering the facts that the general lighting is responsible for nearly 20% of the electrical energy consumption [1] and that the display market grows at a significantly high rate owing to the wide-spread use of mobile devices,[2] developing efficient light-emitting devices turns out to be an important topic of interest for the industry and researchers worldwide. To decrease this energy consumption, light-emitting diodes (LEDs) offer significantly lower energy consumption compared to existing technologies including incandescent lamps and fluorescent lamps.[3] Currently, the LED technology mainly relies on the use of an LED chip, which emits high energy photons in ultraviolet or blue part of the electromagnetic spectrum, together with a color-converting layer.[4], [5] The conventional color-converters are based on the phosphors made of garnets doped with rare-earth ions.[6] Despite their high photon quantum yields, these materials exhibit a significantly broad emission spectrum, which is not apt for to achieve high-quality lighting. In addition, the problems associated with their supply[6] further threaten the LED industry. As an alternative, colloidal semiconductor quantum dot (QD) nanocrystals (NC) step forward as they enable spectrum tuning by size and shape control leading to high-quality lighting.[7] Furthermore, their narrow-band emission spectra allow for the generation of spectrally pure colors, which significantly helps increasing the color definition of the displays.[4]

However, the efficient QDs mainly employ cadmium, which makes them unfriendly for the environment and health, especially when the cadmium is

ionized.[8] A solution to this problem may arise from the use of organic semiconductor polymer nanoparticles. However, despite the reports proving their potential, their low solid-film efficiencies and low emission stabilities limit their use in the solid-state applications. To address this problem of these fluorescent polymer nanoparticles, in Chapter 3 of this thesis, we present our study on embedding oligomer nanoparticles into nonionic organic sucrose crystal to increase their emission efficiency and stability to make them suitable materials as color-converters on LEDs.

The use of crystalline matrices was also shown to offer significant advantages for obtaining efficient and stable solid films of QDs.[9]–[13] Especially studying the interactions of the incorporated QDs within the host medium may allow for improving the emission intensity and stability of the QDs. In addition, the effect of the host medium on the emission of the incorporated QDs is an interesting phenomenon to study. With this motivation, in Chapter 4 of this thesis, we present our design on a composite material system including QD-incorporated macro-scale anthracene crystals. This hybrid structure allows the energy to be transferred nonradiatively from the host matrix to the acceptor QDs while providing polarization anisotropy to the otherwise-isotropic QD emission.

During this graduate study at Bilkent University, the second problem that we aimed to address is on obtaining nanoparticles that are capable of providing high contrast in bioimaging. Today, bioimaging has become an essential part of the medical diagnosis and particularly enables the detection of the tumours. Among the many bioimaging approaches such as fluorescence imaging, positron emission tomography (PET) and computer tomography (CT), magnetic resonance imaging (MRI) steps forward thanks to its sensitivity and safety. Furthermore, this sophisticated noninvasive diagnostic tool provides high-resolution imaging in three dimensions.[14] However, the requirement to the contrast agents that allow for the differentiation of anatomical details by enhancing the contrast and image quality directed researchers to the synthesis of high-quality magnetic nanoparticles. These agents are classified as positive (T_1-weighted) and negative (T_2-weighted) contrast agents. Among them, T_1-weighted contrast agents shorten the longitudinal relaxation times and results in

bright images in the region of interest, while T_2-weighted contrast agents shorten the transverse relaxation time, which leads the formation of a darker image. The most widely studied T_1-weighted contrast agents are gadolinium- and manganese-based nanoparticles and they are frequently employed in clinics owing to their high signal intensity resulting in high resolution between tissues. Despite their qualified imaging features, it is reported that the regular use of gadolinium-based contrast agents may cause nephrogenic systemic failure (NSF) disease in the patients suffering from renal failure.[15] These reports have focused the interest of the researchers on the superparamagnetic iron oxide nanoparticles, which are commonly used T_2-contrast agents in MRI.[16] However, due to the magnetic susceptibility artifacts and negative contrast, it is believed that the iron oxide nanoparticles possessing dual-modal imaging capability are very promising.[17] To achieve this goal, the first approach is based on the doping of the superparamagnetic iron oxide nanoparticles with paramagnetic materials.[18] On the other hand, the second method is to decrease the diameter of the nanoparticles to a few nanometers, which enhances the paramagnetic contribution.[19] In Chapter 5 of this thesis, we demonstrated another method to obtain dual-modal iron oxide-based contrast agents for the first time. In this study, we present the synthesis of highly monodisperse iron oxide nanocubes, their characterizations, and *in vivo* MRI experiments showing dual-modal effect.

Since the iron oxide nanoparticles are commonly used as T_2-contrast agents, the literature lacks of information on their T_1-relaxation dynamics and there is no systematic study on the change of r_1 relaxivity depending on the size and shape of the iron oxide nanoparticles. To address these points, in Chapter 6, we present our study on the investigation of r_1 and r_2 relaxation mechanisms of cubic and spherical iron oxide nanoparticles having different sizes between 7 and 14 nm. We believe that this study may be a further step on the development of dual-modal iron oxide contrast agents simply by tuning their size and shape.

We organized this thesis as follows: In Chapter 2, we start with a brief scientific background on the materials used during this graduate study, then present our research work in detail in Chapters 3-6, and finally conclude in Chapter 7 with the results produced during this period and a future outlook.

Chapter 2

Scientific Background

In this thesis work, we mainly employed the colloidal quantum dots (QDs) and oligomer nanoparticles (OL NPs) as color convertors and the superparamagnetic iron oxide nanoparticles (SPIONs) as contrast agents in magnetic resonance imaging (MRI). Prior to giving experimental details, here we provide brief background information on these materials. We will begin with the synthesis techniques of inorganic semiconductor nanocrystals and continue with the optical properties and application fields of these nanocrystals. Then, we will introduce the synthesis methods of organic semiconductor nanoparticles along with their optical properties and fields where these nanoparticles can be applied. Finally, we will focus on the superparamagnetic metal oxide nanoparticles. Here, after discussing the importance of iron oxide nanoparticle (IO NP) synthesis with uniform size and shape, we will briefly discuss the mostly employed IO NP synthesis routes. We will finish this chapter with the surface modification approaches of IO NPs that are very important for the organic-to-water phase transition and decreased toxicity.

2.1 Colloidal Inorganic Semiconductor Nanocrystals

Fluorescent nanoparticles have attracted significant interest for optoelectronic and biomedical applications, especially within the last two decades.[3], [4], [20] Semiconductor colloidal quantum dot nanocrystals (QD NCs) are an important group of inorganic fluorescent nanocrystals, which reveal unique optical features enabling their use as color-converters and active materials in optoelectronic devices.[3], [4], [21] To date, different types of these nanocrystals have been synthesized by employing from II-VI, III-V and IV-VI group elements. Among the II-VI group elements, we can count CdSe, CdTe, and CdS, which are most widely used in the QD NCs emitting in the visible regime. Cd-free ZnSe and ZnS

QDs are also among the QDs composed of II-VI group elements; however, they emit in the ultraviolet (UV) part of the electromagnetic spectrum. Another class of QDs is based on III-V group elements and can be exemplified with InP QDs that emit visible light. The last group of QDs is based on IV-VI group elements and include PbSe and PbS NCs that emit in the near-infrared (near-IR) and IR emission range. In this thesis work, we synthesized and used II-VI type QD NCs. Therefore, here we will focus on the synthesis of these Cd-based NCs in organic solution.

In this section, we will first introduce the synthesis techniques of colloidal QD NCs. Subsequently, we will summarize the optical properties of these semiconductor nanocrystals and give information on the applications of these QD NCs.

2.1.1 Synthesis of inorganic nanocrystals

For the synthesis of QDs, two main routes have been reported to date. One of these techniques is epitaxial growth (such as molecular beam epitaxy), and the other one is the wet-chemistry method, which is also known as colloidal chemistry (including competitive reaction chemistry, hot-solution etc.).[22] Since the colloidal chemistry is cheaper than the epitaxial techniques for obtaining semiconductor nanoparticles,[23], [24] we will only focus on this type of materials in this part of the thesis.

Typically, colloidal semiconductor quantum dots are atomic clusters composed of few hundreds to millions of atoms. They are typically fluorescent nanoparticles that in general comprise of a small (~1-10 nm) inorganic semiconductor core, an inorganic shell and a layer of organic passivating ligands.[25] While the core is a quasi-zero dimensional quantum dot, the shell is used to improve the optical properties including quantum yield and emission stability, and ligands enable their dispersibility and prevent them from forming agglomerates. Moreover, the type of the ligands governs the final solvent dispersing the nanoparticles, which can be nonpolar or polar, organic or inorganic solvents.

For the synthesis of colloidal QDs, basically three different structures have been developed. These are the synthesis of "core" QDs, the synthesis of "core/shell type composite QDs" that are grown using core QDs, and "core/alloyed shell" QDs, which are synthesized in a single step and thus, also referred to as QDs synthesized in one-pot (Figure 2.1). Among the most widely used core QDs, we can include CdTe, CdSe, CdS, ZnSe and ZnS. They can be dispersed in organic[26], [27] or aqueous[11], [28] solvents depending on the ligand that is attached to QDs. However, the main challenge for the core QDs is the decreased quantum yield and low emission stability. Furthermore, the difficulty in obtaining small QDs emitting at shorter wavelengths arises as another problem.[29]–[31]

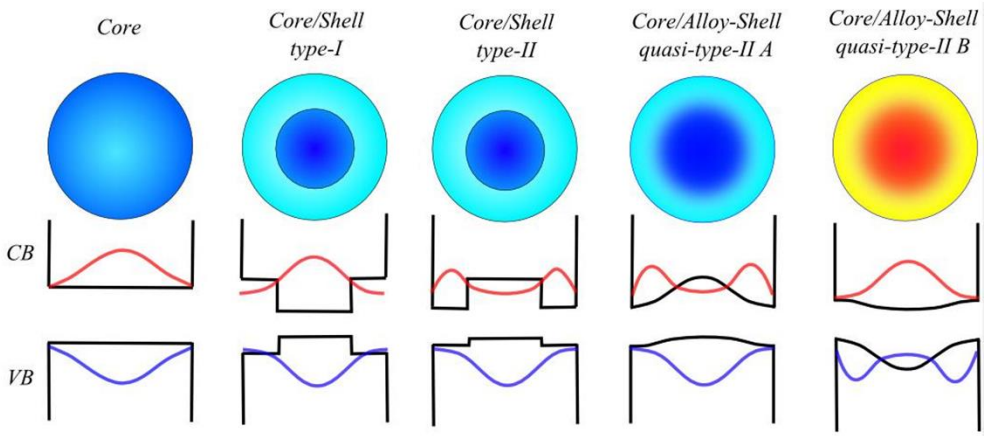

Figure 2.1. Representative drawings of different architectures of QDs along with their electronic bands (black), electron (red) and hole (blue) wavefunctions. Reproduced with permission from Ref.[32]. Copyright The Royal Society of Chemistry 2013.

The core/shell QDs constitute an important class of these semiconductor nanocrystals. In this material system, nonradiative recombination sites on the surface of core QDs are passivated better, which results in higher photoluminescence quantum efficiencies.[33] Moreover, the shell protects the structure from photo-oxidation leading to improved emission stability at higher temperatures and under high photon fluxes. Depending on the band alignments of the materials used in the core and shell of the QDs, the core/shell QDs can

possess type-I or type-II band alignment. In type-I QDs, both of the electrons and holes are confined within the core. However, in type-II QDs, electrons and holes prefer to localize in different parts of the QDs.[34] Most common Cd-based core/shell QDs are CdSe/CdS and CdSe/CdS/ZnS QDs that have type-I band alignment together with CdSe/ZnTe and CdTe/CdSe QDs possessing type-II band alignment.

To obtain these core/shell QDs, first, only core QDs are synthesized and then the growth of a shell layer around this core QD follows. After synthesizing the core QDs, the size and concentration of the core nanocrystals are calculated by absorption spectroscopy. Using these calculations, appropriate amounts of precursors for the shell growth are determined, and the shell is coated over the core QDs. The most mature form of CdSe core synthesis was reported by Bawendi group, in which these cores were used to produce core/shell quantum dots.[35] A typical synthesis procedure of these core/shell composite QDs is summarized as follows:

Step 1. CdSe core synthesis:

CdSe core QDs can be synthesized in two different crystal structures referred to as wurtzite-CdSe (W-CdSe) and zinc-blende-CdSe (ZB-CdSe) cores using different procedures. Firstly, we will give information on the W-CdSe synthesis procedure. For this type of core synthesis, a mixture of 60 mg cadmium oxide (CdO), 280 mg of octadecylphosphonic acid (ODPA) and 3 g of trioctylphosphine oxide (TOPO) are prepared in a 50 mL three-neck flask. In order to remove the undesired residues, the reaction solution is degassed at 150 °C for 1 h under vacuum. Then, the solution is heated up to 320 °C under nitrogen or argon flow and 1.0 mL of trioctylphosphine (TOP) is added into the flask at this temperature. Subsequently, the temperature of the reaction mixture is increased to 380 °C. The injection solution prepared by mixing 60 mg selenium powder (Se) and 0.5 mL TOP is injected into the flask quickly and reaction is cooled down to room temperature when the CdSe core nanoparticles are obtained with the desired size. As-synthesized nanocrystals are precipitated by adding acetone and dispersed in hexane for further experiments.

On the other hand, ZB-CdSe cores can be synthesized using the following procedure. For this purpose, 0.1 mmol of selenium dioxide powder, 0.1 mmol of cadmium myristate and 5.0 g of 1-octadecene (ODE) are mixed in a three-neck flask and degassed under vacuum at room temperature. After 10 min, the reaction solution is heated to 240 °C at a heating rate of 25 °C/min under argon flow. The growth of the nanocrystals takes place within 2 min at 240 °C and then 0.1 mL of oleic acid (OA) is added into the solution dropwise to stabilize the growth. Finally, the solution is cooled down to room temperature and the nanocrystals are precipitated using acetone. Cores are dispersed in hexane and stored as a stock solution for further experiments or shell growth.

Step 2. CdS shell growth on CdSe core:

In order to synthesize core/shell QDs, one or more inorganic shell is grown on the core QDs as described below. 100 nmol of CdSe core QDs dispersed in hexane is mixed with the mixture of 3 mL oleylamine (OAm) and 3 mL ODE in a three-neck flask for the shell growth. The reaction mixture is degassed under vacuum at room temperature for 1 h and then at 120 °C for 20 min. Afterwards, the temperature of the reaction solution is increased to 310 °C at a constant heating rate of 18 °C/min under nitrogen flow. While the temperature of the mixture is increasing, the mixtures of cadmium (II) oleate (Cd-oleate) in 6 mL of ODE and octanethiol (1.2 equivalent amounts of Cd-oleate) in 6 mL ODE are injected dropwise with a constant rate of 3 mL/h at 240 °C. After injection, 1 mL of oleic acid (OA) is added quickly and the reaction is kept for further 60 min at 310 °C. For the cleaning, the obtained nanoparticles are precipitated with acetone and dispersed in hexane. This step is repeated for two times and CdSe/CdS core/shell QDs are stored by dispersing them within a nonpolar solvent such as hexane or toluene (Figure 2.2).

Figure 2.2. Real color images of core/shell QDs under UV light.

Although the core/shell QDs have high photoluminescence quantum yields (QY) and narrow photoluminescence peaks, their synthesis procedure is very difficult. One-pot technique (core/alloyed shell), on the other hand, is an easier procedure than the sequential core/shell QD synthesis. The QY of the red-emitting core/alloyed shell QDs obtained by one-pot method is lower than the standard core/shell QDs; however, green- or yellow-emitting QDs can be obtained to be efficient using this technique. Briefly, one-pot synthesis of these QDs is based on the rapid injection of semiconductor precursors into a vigorously stirring hot reaction system where the specific organic solvents and surface attaching molecules are present. [29], [31] This single-step QDs emitting at various wavelengths in the range of 500-610 nm are first reported by Bae *et al.* [36]

In this thesis work, QDs synthesized via one-pot technique have been studied and its synthesis procedure is summarized below. For a typical synthesis of CdSe/CdZnSeS/ZnS nanocrystals, zinc acetate ($Zn(acetate)_2$), cadmium oxide (CdO), selenium powder (Se) and sulphur powder (S) are used as precursors, TOP and oleic acid (OA) or dodecanethiol (DDT) are used as surfactants and ODE is used as the solvent having a high boiling point. Briefly, a mixture of 4 mmol of $Zn(acetate)_2$, 0.4 mmol of CdO, 5.6 mL of OA and 20 mL of ODE are prepared in a three-neck flask and degassed for 1 h at 100 °C under vigorous stirring to remove oxygen, humiditiy, and other undesired residues. Subsequently, the temperature of the reaction solution is raised to 310 °C under argon flow. For Se and S precursor solutions, a mixture of 0.1 mmol of Se powder

and 4 mmol of S powder are prepared in 3 mL of TOP separately, and injected into the reaction flask quickly at 310 °C. After 1 min, another solution consisting of 0.3 mL of DDT and 0.8 mL of ODE is injected dropwise into the reaction flask. The nanoparticles are allowed to grow at 300 °C for 10 min to obtain green-emitting core/alloyed shell QDs and the solution is cooled down to room temperature quickly. For cleaning, QDs are precipitated with hexane/acetone mixture. Finally, QDs are dissolved in hexane or toluene and stored for further experiments.

2.1.2 Optical properties and applications

Within the last few decades, QDs have attracted significant interest because of their unique optical properties including broad absorption bands, narrow emission spectra, and high photostability. Tuning of the emission peak and absorption band edge is basically governed by the quantum size effect occurring due to the small nanoparticle dimensions, which is why the QDs are also called artificial atoms. While the size is decreasing toward the Bohr exciton radius, the energy states in the bulk semiconductors start to separate apart so that the energy band gap increases, which leads to a blue shift in the absorption and emission spectra of the QDs.[34] (Figure 2.3) If the confinement occurs in three dimensions, quasi-zero dimensional (0D) quantum dots are obtained. Confinement in two dimensions creates 1D quantum wires or nanowires, whereas carrier confinement in one direction produces 2D quantum wells or nanoplatelets.[37]

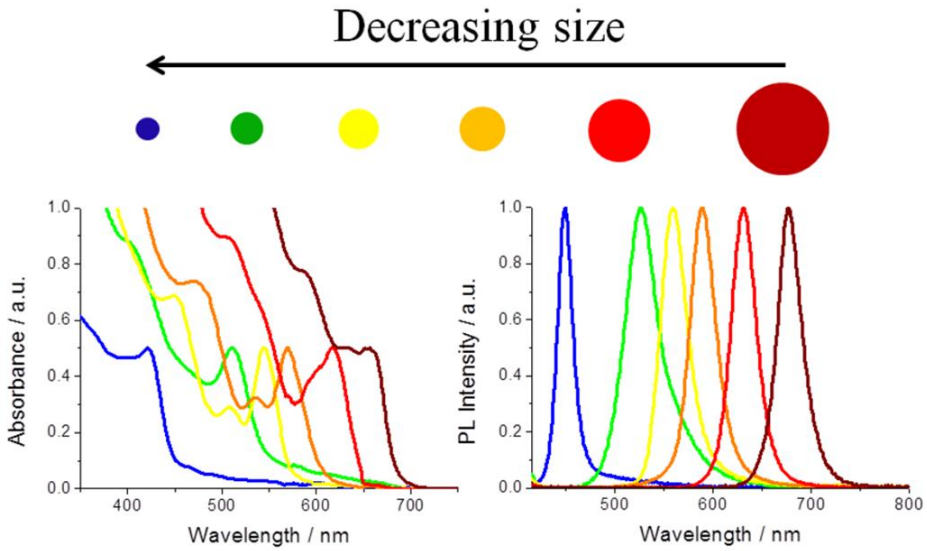

Figure 2.3. Absorption (left) and photoluminescence (right) spectra of QDs with varying sizes under UV light excited at 380 nm. Reproduced with permission from Ref.[38] Copyright MDPI AG 2012.

In addition to core dimensions governing many optical features, size uniformity is another important criterion for high-quality lighting and display applications. This is because the homogeneity in the QD size leads to decreasing the inhomogenously broadened full-width at half-maximum (FWHM) of the emission spectra, which increases color purity. The emission wavelengths of the QDs can be tuned by changing the composition of core and/or shell in addition to controlling the size. For example, while the emission of CdSe and CdTe QDs is within visible region, ZnS emits in the UV/blue spectral region. Additionally, the choice of shell coating material can also affect the emission spectrum of the QDs. Many core/shell QDs are prepared by coating the emissive cores with the ZnS, CdS and ZnSe layers having higher bandgap. However, the bandgap of the shell material still remains below the bandgap of the ligands, which enables a weaker exciton confinement compared to only core QDs. Therefore, we observe a red shift upon coating the core QDs with a shell material.

Since the bandgap energy can be tuned to cover the whole visible regime and their optical properties can be controlled by altering their size and composition, QDs are promising materials for a wide range of optoelectronic and biomedical

applications. QD-based light-emitting diodes (LEDs) are especially promising materials to obtain high efficiency and high-quality lighting owing to their narrow-band emission spectra that enable us to control the emission spectra of the color-converted LED electroluminescence spectrum.[4], [10] This narrow-band emission also allows for obtaining very pure colors; therefore, QDs are good candidates for next generation lighting and displays since they enable a significantly broad color gamut. This potential of the QDs has already attracted the attention of the display manufacturers including Sony, Samsung, and Kindle.[3], [4] Another important application area of the QDs is lasers. The main problem of the current semiconductor lasers includes the challenges to access the green and yellow regions of the spectrum.[39] To address this issue, QDs have been used in numerous studies thanks to their tunable optical gain and emission spectrum.[39]–[41]

QDs are valuable materials not only for optoelectronics, but also for biomedical applications. Because of their high efficiency and photostability, QDs are good alternatives to dyes for labeling biomolecules and cells. In order to obtain water-soluble QDs or protect them from immune system, many biomolecules have been attached to the surface of the QDs and it is reported that these bindings have no significant negative effect on the optical signatures of QDs and the functionality of the biomolecules.[20] Many works have been reported on the labelling of QDs for tracking intracellular/extracellular dynamics of a single cell[22] and biomolecule imaging *in vivo* and *in vitro*.[42] In addition to imaging, biosensing is another important application of the QDs. Within this framework, for example, glucose sensing has been successfully reported[43], [44] and pH-sensors/probes have also been developed using QD-dopamine composite materials.[45]–[47]

2.2 Colloidal Organic Semiconductor Nanoparticles

π-conjugated systems make another important group of fluorescent nanoparticles attracting considerable attention. Their small sizes, high fluorescence capabilities, and photochemical stabilities make these conjugated systems especially promising for optoelectronics and biological applications. These materials can be investigated mainly in two groups that are conjugated polymer nanoparticles (CPNs) and self-assembled small-molecule nanoparticles that are also known as oligomer nanoparticles (OL NPs). These particles can be synthesized by three different techniques: miniemulsion, reprecipitation and self-assembly. In this part of the thesis, we reviewed the synthesis methods of these π-conjugated nanoparticle systems, their optical properties, and applications.

2.2.1 Synthesis of organic nanoparticles

Inorganic nanoparticles such as QDs exhibit outstanding optical properties in addition to a remarkably high photostability. However, possible toxicity problem of Cd-based QDs along with the difficulties in their surface modification have directed researchers to fluorescent organic nanoparticles. In this part, we discuss three different techniques to obtain conjugated polymer nanoparticles (CPNs) and conjugated small-molecule nanoparticles (CSMNPs).

Polymers are mainly organic macromolecules that constitute of monomers. Conjugated polymers are a specific class of polymers exhibiting conducting or semiconducting properties. These features stem from the presence of conjugated double bonds allowing electrons to move throughout the polymer on the p-orbitals.[48] CPNs and CSMNPs are usually prepared from these conducting polymers using techniques reviewed below.[49]

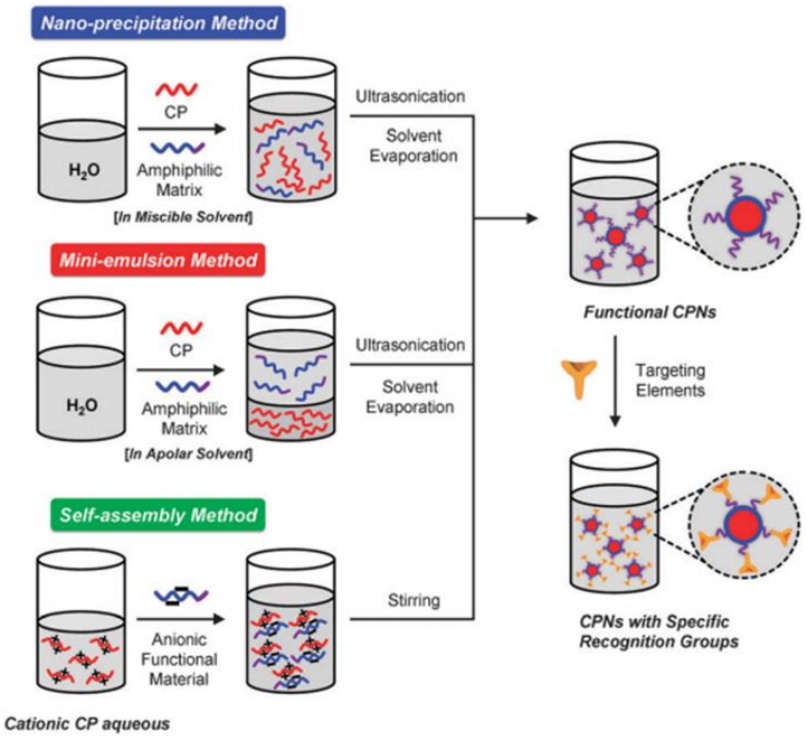

Figure 2.4. Schematic representation showing different strategies to prepare CPNs. Reprinted with permission from Ref. [49] Copyright The Royal Society of Chemistry 2013.

CPNs can be typically synthesized by miniemulsion, reprecipitation and self-assembly techniques (Figure 2.4). Among them, the miniemulsion method is the most frequently used technique based on the nanoparticle formation based on a mixture of water and nonpolar solvent. Briefly in this method, desired polymer is dissolved in an organic solvent, which is immiscible with water, and then is injected into water to generate phase difference. Subsequently, this prepared mixture is stirred swiftly using an ultrasonicator to obtain small polymer droplets. Finally, the solvent of the CPNs is completely evaporated and particles are dispersed in water. The diameter of the CPNs can be in the range of 30-500 nm. Ostwald ripening and flocculation can be observed sometimes; however, they can be avoided by adding additives.[50]

Another approach to obtain CPNs is the reprecipitation (nano-precipitation) method. In this technique, a hydrophobic polymer is dissolved in a good solvent and injected rapidly into a poor solvent while stirring with an ultrasonicator. As

a result of the injection, polymers start to aggregate to decrease the contact with poor phase and form nanoparticles. In many studies, it is reported that the concentration of starting polymer solution affects the size of resulting CPNs.[51], [52]

After the discovery of silole molecules in the beginning of 2000s, synthesis and use of self-assembled conjugated small-molecule nanoparticles have been initiated by Tang *et al.* who reported that nonfluorescent small silole molecules turn out to be highly emissive after aggregation.[53] The physical reasoning of this phenomenon is explained by the rotational change of phenyl groups around the core silole owing to the aggregation, which was shown to weaken the nonradiative energy transfer. Similar aggregation induced emission observations are also reported by other groups.[54]–[56] Compared to their conjugated polymers counterparts, these small-molecule nanoparticles have advantages of possessing well-defined molecular structures in addition to the capabilities of extremely pure synthesis and having well-controlled molecular weights.[57], [58] The self-assembly process of these structures is mainly directed by non-covalent interactions such as electrostatic interactions, π–π stacking, van der Waals interactions, and hydrophobic effects.[59] Briefly in this method, nanoparticles are obtained by mixing separately prepared polymer solutions under stirring and formed nanoparticles are collected by centrifugation at high speeds.[49]

Within the framework of this thesis work, we used oligomer nanoparticles obtained by self-assembly technique. In order to obtain them, first red-emitting oligomers are synthesized in three steps and dispersed in tetrahydrofuran (THF). Subsequently, water-dispersible oligomer nanoparticles are obtained by reprecipitation method using oligomer solution in THF. The experimental details on the nanoparticle synthesis can be obtained from Refs. [60], [61]

2.2.2 Optical properties and applications of organic semiconductor nanoparticles

CPNs are promising fluorescent materials particularly for biological applications thanks to their low toxicity, biocompatible nature and small diameters. Considering the large absorption cross-section and high quantum yield of π-conjugated systems,[62] these materials are good alternatives to the inorganic

semiconductor materials (Figure 2.5). The optical features of conjugated polymers mainly depend on the intra- and inter-chain interactions and can be tuned by adding numerous functional groups or backbone molecules. For example, addition of the functional groups to the molecule was shown to change both of the color and targeting functions.[63], [64] Also, size and aggregation are other important parameters for emission color and quantum yield. Typically, lower quantum yields are observed with the increasing size of conjugated polymers and polymer nanoparticles. This is mainly attributed to the energy transfer mechanism within the structure. While the particle size is increasing, the configuration and interaction of many fluorescence quenching sites on the molecules affect the efficiency of energy transfer. Until 2013, it was believed that conjugated small molecules and polymers with the same sizes reveal similar properties. However, Fischer *et al.*[65] compared these two groups in terms of size and found that they have significant differences in optical features. Conjugated polymers are good candidates as drug carries whereas conjugated small nanoparticles release the drug within a shorter time. On the other hand, conjugated small-molecule nanoparticles are shown to possess superior optical features with quantum yields as high as 90% and reported to be as good candidates for imaging applications.

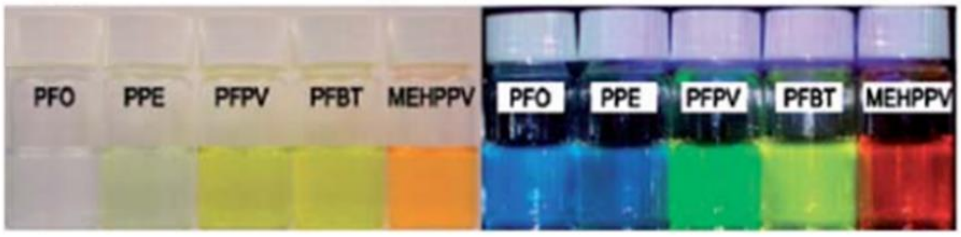

Figure 2.5. Real color images of aqueous CPNs under day light (left) and UV light (right). Reproduced with permission from Refs. [62], [66] Copyright The Royal Society of Chemistry 2008 and 2010.

In these nanoparticles, the modification of absorption spectrum depends on the preparation conditions. If conjugated nanoparticles are prepared by miniemulsion or reprecipitation techniques, a blue shift is observed in the absorption spectrum due to the unordered conformation and conjugation length reduction.[52] However, in self-assembly method, nanoparticles have time to be well-organized, which shifts their absorption spectrum toward longer

wavelengths.[67] The absorption cross-section is correlated with the diameter of the nanoparticles and increases with the increasing size. Considering this, the absorption cross-sections of small-conjugated nanoparticles and CdSe quantum dots (in the visible and near-UV range) with similar sizes turn out to be comparable with each other.[62], [68] Additionally, these conjugated small-molecule nanoparticles reveal higher absorption cross-sections and florescence brightness compared to their conjugated polymer counterparts.[69] The structure-dependent optical features along with high photostability and brightness make these organic semiconductor nanoparticles suitable for biological applications and optoelectronics, which we will survey below.

For biological applications, biocompatibility, low toxicity, and dispersibility in water (or physiological environment) are important parameters in addition to their chemical functionalization capability. Basically, three different strategies are carried out to functionalize CPNs. The first and second techniques are based on the binding of specific groups such as targeting groups, amino or carboxyl groups, and alkoxyl chains. In general, two strategies can be followed to bind these groups. In the first method, polymerization is performed following the binding of groups while the second strategy involves linking the functional groups to the naked CPNs by employing electrostatic and hydrophobic interactions. The latter strategy consists of two steps that include i) binding specific groups such as amino/carboxyl groups to the CPN surfaces and ii) covalently binding targeting/functional groups such as peptides, proteins, antibodies, and drugs to the molecules linked in the first step. Some of the functional groups/molecules and their linking modes are represented in Figure 2.6.

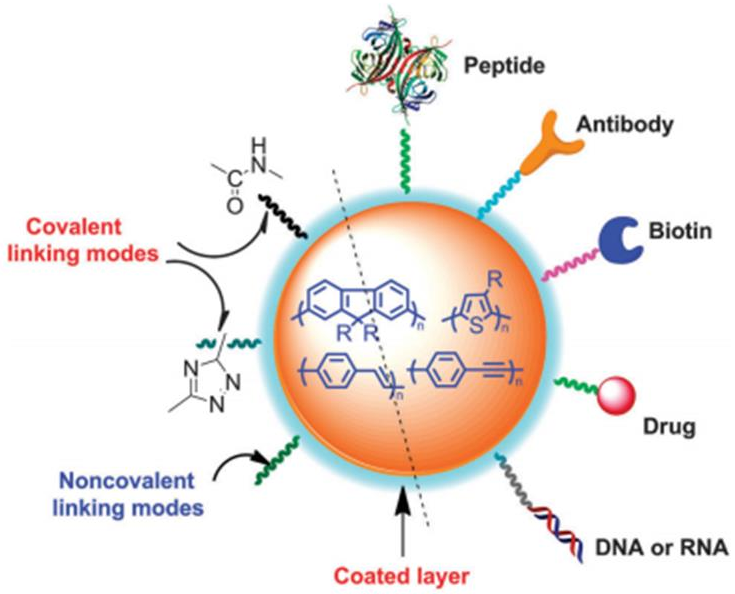

Figure 2.6. Schematic representation of attachment modes and some of the functional groups. Reproduced with permission from Ref. [49]. Copyright The Royal Society of Chemistry 2013.

The biological use of these functionalized CPNs can be grouped as fluorescence imaging, antibacterial/antitumor activities and drug/gene delivery. Both of the targeted and non-targeted CPNs have been reported for fluorescence imaging. In a study by Li *et al.*,[70] folic acid was linked to poly(DL-lactide-*co*-glycolide)/conjugated polymer co-encapsulated nanoparticles and targeted to MCF7 breast tumor cells. Under fluorescence imaging, it was observed that folic acid functionalization significantly enhances cellular uptake of the nanoparticles through receptor-mediated endocytosis. Non-targeted NPs can also be uptaken by cells, however, their uptake efficiency turns out to be very low. Another application field of CPNs is photodynamic therapy (PDT). This was discovered by Whitten *et al.*[71] in 2005. Researchers found out that cationic poly(phenyleneethynylene) (PPE) derivative have antibacterial effect on gram-negative *Escherichia coli* and gram-positive *Bacillus anthracis*. Moreover, antitumor activity of CPNs are also demonstrated by Chong *et al.*[72] CPNs are also preferred as gene or drug carrier due to their low toxicity and optical properties. In this respect, there are additional reports on the delivery of small interfering RNA[73] and plasmid DNA.[74] Also, drug delivery studies were

carried out by different groups.[60], [75] In a study reported by Pennakalathil *et al.*,[60] hydrophobic anticancer drug loaded pH sensitive red-emitting CPNs were synthesized and shown to be as a good candidate for drug delivery.

CPNs are good materials not only for biological applications, but also for optoelectronic applications. Photovoltaic devices [76], [77], energy transfer systems [78]–[80] and LEDs [76], [81], [82] are among the main fields that CPNs are employed. Since we used conjugated small nanoparticles as color-converters on blue-emitting LEDs in this thesis, here we will focus on lighting applications of CPNs in this part. In this respect, white-emitting CPNs have been synthesized and optically characterized in a study reported by Park *et al.* [81] In this work, crosslinking via UV exposure was shown to create a core/shell type nanoparticle that allows for controlling the photoluminescence spectra. The use of these nanoparticles on LEDs enabled obtaining a cool-white shade LED having a moderate color rendition performance. The researchers reported that these materials have high efficiency under low optical power levels, and can be used in lighting application as color-converters. In another study, methyl-substituted ladder-type poly(p-phenylene) nanoparticles were synthesized by miniemulsion method and used for LEDs. Results showed that LEDs obtained by this approach have better optoelectronic properties compared to polymer based organic light emitting diodes (OLEDs) [82]. In another work, Huyal *et al.* demonstrated the use of polyfluorene based CPNs for white LEDs exhibiting a successful color rendition capability.[83] In another work reported by the same group, these nanoparticles were shown to exhibit a high quantum yield reaching ~70% in solid films, which proves the suitability of the CPNs on LEDs as color-converters for high-efficieny white LEDs.[84] The hybridization of the CPNs with semiconductor QDs was also shown as another technique for obtaining high-quality lighting. Within this framework, Demir *et al.* co-integrated blue-emitting CPNs together with yellow-, green-, and red-emitting QDs to obtain white light. The resulting material system exhibited a warm white shade with a reasonable color rendering capability.[85]

Usually, solution-processed CPNs have been used in most of the studies due to the decreased efficiency problems following the film preparation. This decrease occurs depending on the aggregation and increased inter- and intra-chain interactions of CPNs in the film state, which also causes a red shift in the

emission spectrum.[84], [86] To address this problem, we developed a new technique to increase the fluorescence efficiency of conjugated small nanoparticles (OL NPs) in the film state for the lighting applications, which will be explained in detail in Chapter 3.

2.3 Colloidal Superparamagnetic Metal Oxide Nanoparticles

Another class of nanoparticles used in this thesis is based on metal oxides. Metal oxide nanoparticles can be considered as an important material system for nanotechnology in its broadest sense. For instance, zinc oxide nanoparticles can be used as electron transport layers in light-emitting and light-harvesting devices,[87] titanium dioxide nanoparticles are preferred in solar cells and in catalysis applications[88] whereas nanoparticles having magnetic character such as manganese oxide, cobalt oxide, and iron oxide are promising for magnetic resonance imaging (MRI) and hyperthermia.[89] In this thesis work, we studied the potential of iron oxide nanoparticles possessing various sizes and shapes for use as contrast agents in MRI. Therefore, here we focus on the iron oxide nanoparticles (IO NPs). In this section, after discussing the importance of size and shape controlling of IO NPs, we provide a concise introduction on their crystal structures and synthesis and the strategies for their surface modification, which is very important for the toxicity issues and organic-to-water phase transition.

2.3.1 Synthesis of metal oxide nanoparticles

Iron oxide nanoparticles are very promising materials owing to their low toxicity and magnetic properties. Because of their superparamagnetic nature, they can be manipulated by an external field and lose their magnetization after the removal of magnetic field, which prevents agglomeration in the physiological environment. Thanks to these advantages, they especially find use in biomedical applications, particularly in magnetic resonance imaging (MRI).[90]

Before providing information on the synthesis techniques of IO NPs, we will first discuss the importance of size, shape, microstructure, and uniformity on the magnetic properties and the frequently observed crystal structures of IO NPs. Particle size is one of the most important parameters affecting all of the magnetic features of the IO nanoparticles. While the bulk IO materials have multidomain structures, it changes with the decreasing size and a single magnetic domain is energetically preferred when the size decreases below a critical particle diameter.[91] These single domain nanoparticles exhibit superparamagnetic behavior and no hysteresis loop is observed. On the other hand, ferrimagnetic materials show hysteresis loop as also shown in Figure 2.7.

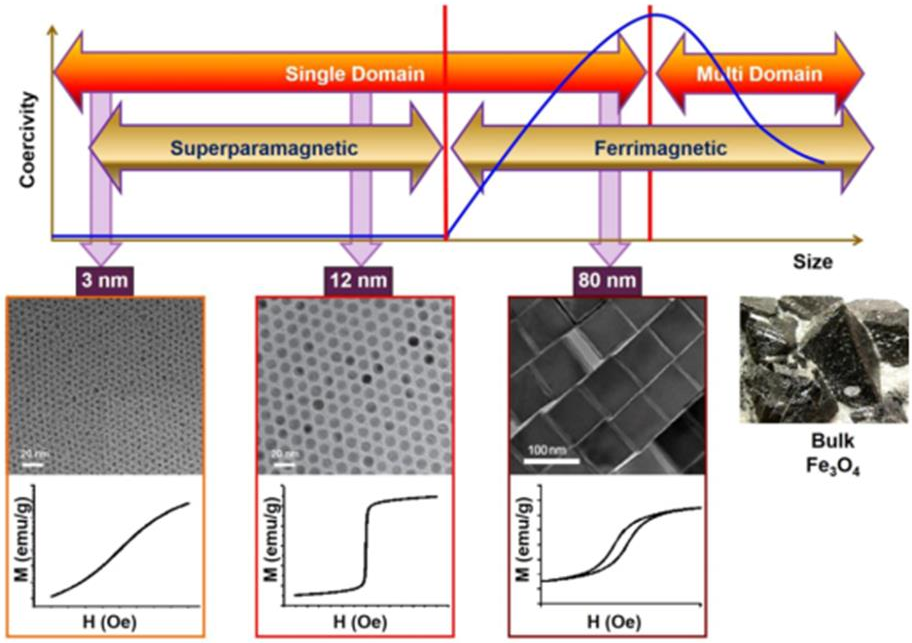

Figure 2.7. Influence of the particle size on the magnetic properties of iron oxide nanoparticles, shown along with their TEM images. Reproduced with permission from Refs. [92]–[95] Copyright American Chemical Society 2008, 2011, and 2015. Copyright Nature Publishing Group 2004.

Particle shape is another parameter affecting magnetic behaviors. For instance, Sayed *et al.* [96] synthesized several uniquely shaped IO NPs such as nanorods, nano husk, nanocube, porous spheres, and self-oriented flowers. They tuned the shapes of the IO NPs by changing the precursor iron salts and

investigated their crystal structures. Results demonstrated that both the size and shape affect the crystal structure, which results in the variation of magnetic features. Since the size and shape of the IO NPs have a significant role in the magnetic properties of the nanoparticles, the nanoparticle uniformity is also an important concern in the iron oxide synthesis. Heterogeneous nanoparticles negatively affect the total magnetic response, while reproducible well-defined magnetic response can be recorded when NPs of homogenous size and shape distribution are obtained.[97]

IO NPs may have different crystal structures including hematite (α-Fe_2O_3), maghemite (γ-Fe_2O_3) and magnetite (Fe_3O_4).[98] Hematite has weak ferromagnetic properties at room temperature, and is very rarely preferred due to this disadvantage. Although maghemite nanoparticles possess ferrimagnetic behavior at room temperature, they become unstable at high temperatures. However, it was reported that doping maghemites with other metals is a good approach to enhance their stability.[92] IO NPs having magnetite crystal structure are among the most widely-studied materials for biological applications and are considered to be more favorable compared to the hematite and maghemite counterparts owing to their biocompatibility and size-dependent magnetic features.[99] Although bulk magnetite has ferrimagnetic property at room temperature, small NPs (<20 nm) have a single domain and display superparamagnetic behavior.[100], [101]

Within the last few decades, various techniques have been reported on the syntheses of metal oxide nanoparticles such as hydrothermal synthesis,[102] microemulsion method,[103] sol-gel syntheses,[104] thermal decomposition method,[17], [105] laser pyrolysis technique,[89] co-precipitation method,[106] sonochemical reactions,[107] flow injection syntheses,[108] and electrospray syntheses.[109] Among these, the most common techniques for the synthesis of iron oxide nanoparticles include co-precipitation, microemulsion and thermal decomposition methods, which will be explained below.

Co-precipitation is a very simple approach for the synthesis of IO NPs. In this technique, aqueous solutions of ferrous and ferric salts are aged following the base addition under inert atmosphere.[97] This process can be carried out at

room temperature or higher temperatures. Although large amounts of NPs can be obtained by this technique, particle size distribution of NPs is limited and controlled by many parameters such as salt type, salt concentration, PH, and ionic strength of the system.[110]

Microemulsion is another technique to obtain IO NPs. In this method, oil is mixed with the surfactant added water to obtain immiscible two phase, where droplets are formed. Some of the widely used surfactant molecules are sodium dodecyl sulfate (SDS), cetyltrimethylammonium bromide (CTAB) and polyvinylpyrrolidone.[111] Here, surfactant is mainly used for stabilization and the ratio of surfactant/water is an important parameter for controlling the particle size and distribution.[97], [112] To date, numerous nanoparticles such as iron oxide,[113], [114] polymer/iron oxide composite nanoparticles [115], [116] and metallic iron nanoparticles [113], [117] have been synthesized using this approach. However, since the low temperature is used in this route, the crystallinity and the magnetic properties of these SPIONs become very poor.

The last synthesis technique, which will be discussed here, is thermal decomposition (pyrolysis) method. It is based on the phase decomposition and oxidation of organometallic compounds such as iron-acetylacetonate ($Fe(acac)_3$), iron (III) chloride ($FeCl_3$) and iron pentacarbonyl ($Fe(CO)_5$) in high-boiling organic solvents consisting of varying surfactants.[112] Frequently used surfactant molecules are fatty acids such as oleic acid, linoleic acid, palmitoleic acid, and fatty amines such as oleylamine. Although thermal decomposition method is an old technique, it made important progress over time. In the first studies involving this method, a further size-selection procedure was required to have monodisperse nanoparticles.[118] However, in 2001, Hyeon *et al.* eliminated the size selection process and synthesized relatively uniform IO NPs with iron pentacarbonyl precursor, oleic acid, and octyl ether without size selection.[119] Three years later, Jana and co-workers [89] applied this technique to numerous magnetic oxide nanoparticles such as chrome, manganese, iron, cobalt, and nickel. They used heat to decompose the metal fatty acids in organic solution and managed to synthesize nanoparticles possessing well-controlled size distribution. At the same time, pyrolysis technique was successfully employed

for the synthesis of highly uniform ultra-large scale iron oxide nanoparticles by Park *et al.* [105]. In this study, researchers synthesized iron-oleate (Fe-oleate) precursor with the reaction of freshly synthesized sodium-oleate (Na-oleate) and iron chloride. Subsequently, uniform superparamagnetic iron oxide nanoparticles (SPIONs) were synthesized by thermal decomposition of Fe-oleate precursor in the mixture of oleic acid and ODE (Figure 2.8). Although high-quality iron oxide nanocrystals can be synthesized using this method, the major problem is the dispersibility of the resulting nanoparticles. These as-synthesized iron oxide nanoparticles can be dispersed only in organic solvents, which is a big challenge for the use of these materials in biological studies.[112] However, this problem can be overcome with ligand exchange or surface coating strategies, which will be described in detail in Section 2.3.2.

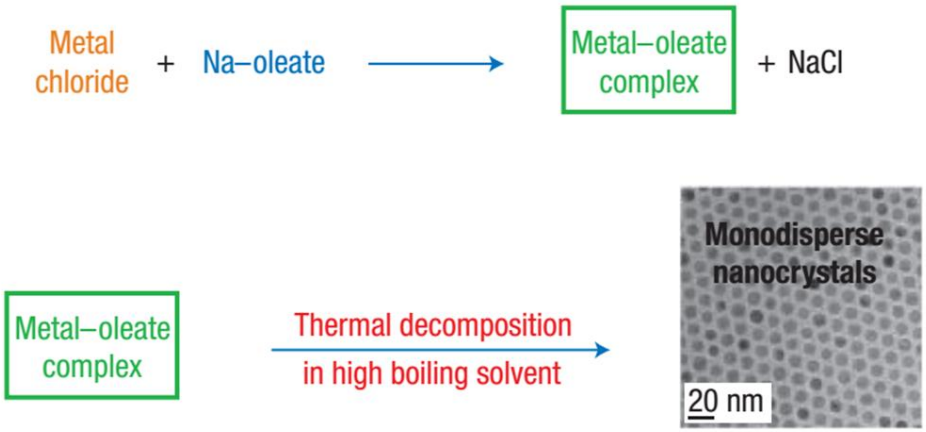

Figure 2.8. Summary of uniform iron oxide nanoparticle synthesis by thermal decomposition method along with TEM image of resulting IO NPs. Reprinted with permission from Ref. [94] Copyright Nature Publishing Group 2004.

2.3.2 Surface modification of iron oxide nanoparticles for organic-to-water phase transition and against toxicity

Since IO NPs are desired to employed for the diagnosis and therapy of diseases in clinics, understanding their toxicity is essential. The reactivity of nanoparticles

is in general higher than their bulk materials due to their large surface area-to-volume ratio, which triggers undesirable reactions within the physiological environment.[120] The main toxic effects of iron oxide nanoparticles arise from their instability over long periods in biological system and the generation of reactive oxygen species (ROS) at high iron concentration levels. Among them, particularly ROS mechanism is responsible for the toxicity of IO NPs by damaging very important structures such as protein, deoxyribonucleic acid (DNA), and mitochondria within the cell, which leads to apoptosis (cell death).[121] For the degradation of IO NPs, mainly endocytosis route is used and, as a result, iron ions are released. Then, the ferritin proteins incorporate these free ions and store them after detoxification process. This mechanism is also known as iron homeostasis and avoids the toxicity of iron oxide nanoparticles.[122] However, if the concentration of iron ions significantly increases in the body, this protection mechanism becomes insufficient and free radical ions start to form, which induces cell death.[123] To address this issue, antioxidants and iron chelation agents can be used.[124] Also, reticuloendothelial system (RES) is a very important mechanism taking role to decrease the IO NP toxicity. Briefly, RES can recognize agglomerations or hydrophobic and charged IO NPs due to the opsonization mechanism and remove them from the circulation within a short time interval [125].

In order to disperse the iron oxide nanoparticles in water and minimize their toxicity, typically two main strategies referred to as encapsulation and ligand exchange are employed (Figure 2.9). Encapsulation is a widely used strategy for the surface modification of IO NPs.[126]–[128] In this technique, a layer of water-soluble materials is formed on the surface of the IO NPs by coating. These surface coating materials can be classified as natural and synthetic polymers, inorganic materials such as silica, and biological molecules such as biotin, proteins, antibodies, and peptides.[98] Among the polymers, polyethylene glycol (PEG) and dextran are two of the frequently used natural polymers for coating the IO NPs owing to their low cost and biocompatibility. For instance, in a study, dextran coated IO NPs were reported nontoxic for human monocyte-macrophages even at their high concentrations.[129] Silica is a transparent inorganic matrix that is also employed as a coating material. Although silica

coating increases the final diameter of the IO NPs, it significantly improves the biocompatibility and stability of the NPs. Also, there are some studies reporting that silica-coated large IO NPs can be cleared from kidney and urinary bladder, which are the main routes for the excretion of molecules typically smaller than 6 nm.[130]–[132] Biological molecules are another large group that have been used for the purposes of targeting and decreasing the toxicity of IO NPs. These molecules can be immobilized on the surface of the IO NPs *via* chemical bonding or physical adsorption. For instance, Lee *et al.* successfully linked streptavitin molecule to γ-Fe_2O_3 IO NPs following the carboxyl group attachment to the surface. They reported that these functionalized nanoparticles can catch biotin-labeled oligonucleotides.[133]

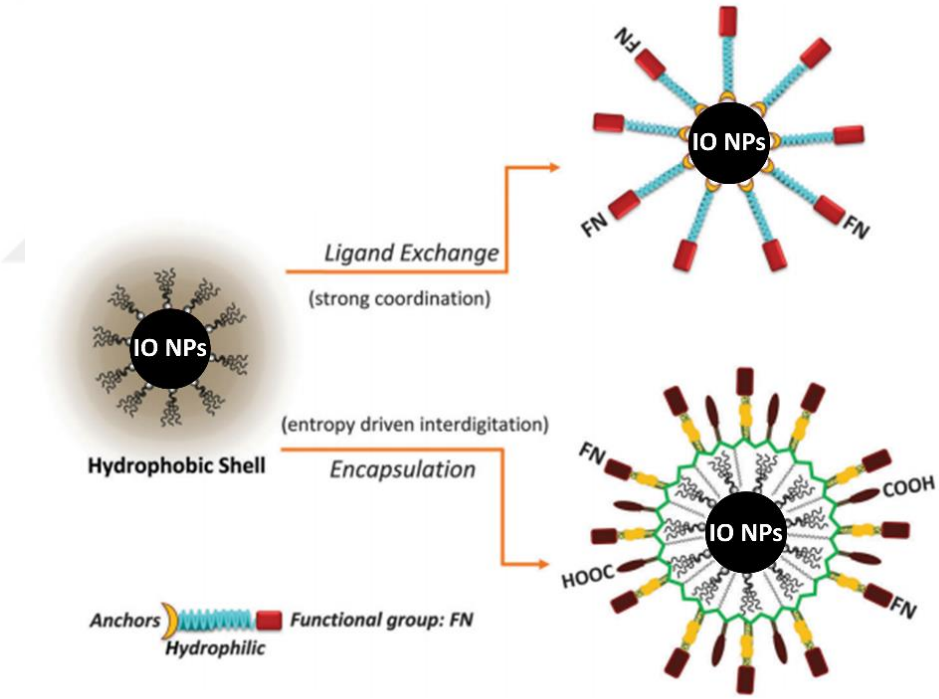

Figure 2.9. Illustration of different approaches for the phase transition of IO NPs. Reproduced with permission from Ref. [134] Copyright The Royal Society of Chemistry 2015.

Another popular approach to produce water-soluble biocompatible IO NPs is the ligand exchange. Briefly, in this method, organic solvent soluble NPs are

transformed into water by exchanging hydrophobic ligands attached to the nanoparticle surface such as oleic acid, oleylamine, hexadecanediol with multifunctional hydrophilic ligands. Some of the frequently used hydrophilic groups are 3-mercaptopropionic acid (MPA), 11-mercaptoundecanoic acid (MUA), and thioglycolic acid (TGA). For effective ligand exchange reaction, excess amounts of ligands are added on organic solvent-dispersible IO NPs solution and vortexed for a while.[135] The stability of these nanoparticles after ligand exchange procedure strongly depends on the number of bounded ligands to the surface. If this process results with low affinity, particles become unstable and aggregates in the water.[92] IO NPs can also be easily transferred to buffer by employing dopamine as a robust anchor and it is reported that this strategy is very effective to prepare stable IO NPs.[136] In another work, hydrophobic ligands were exchanged with octa(tetramethylammonium)–polyhedral oligomeric silsesquioxane (TMA–POSS) and all solution was transferred to water phase successfully.[137]

This review in this chapter allows for the complete introduction of all types of nanoparticles that were colloidally prepared, systematically studied and used in various targeted applications in this thesis.

Chapter 3

Organic Monoliths of Colloidal Oligomer Nanoparticles for High-Stability, High-Efficiency Color Conversion

In this chapter of the thesis, we present our study on increasing the efficiency and stability of the oligomer nanoparticles in solid state. Here, we wrapped oligomer nanoparticles with an organic matrix, which is sucrose in our case, and formed organic emissive monoliths from the powders of these oligomer nanoparticle incorporating sucrose crystals. Using this new approach, we increased the QY of the oligomer nanoparticles by ~7.5 times compared to their drop-casted solid films, which brings their efficiencies to comparable levels with that of inorganic emitters. Moreover, we investigated the temperature stability of these monoliths and observed a ~3-fold improvement compared to drop-casted films of the oligomer nanoparticles. These results revealed that the efficiency and stability of the oligomer nanoparticles can be significantly improved by incorporating them into nonionic organic crystalline matrices.

This chapter of the thesis is mainly based on Z. Soran-Erdem*, T. Erdem*, K. Gungor, J. Pennakalathil, and H. V. Demir, "High-Stability, High-Efficiency Organic Monoliths Made of Oligomer Nanoparticles Wrapped in Organic Matrix" (2016) [61] (*equal contribution). Reproduced with permission from American Chemical Society © 2016.

3.1 Motivation

Conjugated polymers, which gain their semiconducting features from the delocalization of π-electrons along the polymer chain,[138] have attracted

significant interest for numerous applications including light-emitting diodes (LEDs),[81], [139], [140], [66] solar cells,[141]–[143] bioimaging,[62], [144] and sensing.[145] Their easy processability is the main factor making them highly attractive for the aforementioned applications.[146] Additionally, the structure of used monomers allows for tuning their absorption and emission spectra. Attaching various side groups further increases their functionality in terms of the applications.[138] A key acquisition of these conjugated polymers is the capability of their nanoparticle formation resulting in increased dispersibility in water, low toxicity, and reduced sensitivity of the optical features to environmental changes such as thin film formation.[147] However, the problem of significant decrease in the quantum yield (QY) after solution to nanoparticle (NP) and film transition, which is attributed to the aggregate-induced depopulation of the excitons,[84], [86], [148], [149] still persists and strongly restricts the use of conjugated polymers in solid film.

Recently, conjugated oligomer-based nanoparticles have emerged as an alternative to the conjugated polymer nanoparticles.[150] Oligomer (OL) nanoparticles constitute of smaller molecules with well-defined molecular weight compared to conjugated polymer nanoparticles allow for faster guest release, which is especially attractive for drug delivery applications. Furthermore, Fischer *et al.* reported a higher fluorescent quantum yield with comparable stability and molar absorptivity in comparison with conjugated polymer nanoparticles.[151] However, the related literature is still scarce despite the potential of this class of organic nanoparticles. Among the few studies is the work of Dang *et al.*, which reports the synthesis and characterization of copper phthalocyanine oligomer nanoparticles.[152] In another study, Liu *et al.* employed conjugated oligomers to functionalize gold nanoparticles and studied their self-assembly as spherical particles.[153] And recently we demonstrated the use of pH-sensitive orange-emitting conjugated oligomer nanoparticles as drug delivery agents on MCF7 and MDA-MB-231 breast cancer cell lines.[150]

Nevertheless, these OL NPs could not yet be successfully implemented for solid-state lighting application. The main reason behind this has been the inability to obtain strongly emitting color-converting solid films. For example,

spin-coating technique forms only very thin films, limiting the applicability of the nanoparticles as color-converters on LEDs. Drop-casting, on the other hand, allows for the formation of thick films that might be suitable for color conversion; however, in this case the resulting low quantum yields associated with the aggregation remain as the main bottleneck. In addition to these, their emission stability at elevated temperatures is prohibitively low. This problem has to be addressed for possible deployment in industrial use. This is because the light-emitting diode chips driven at high currents that optically excite the nanoparticles expose the nanoparticles to high temperatures. Previously, inorganic semiconductor nanocrystals were investigated using a salt matrix,[9], [13], [154] for which our group studied similar stability issues.[10], [155] However, to date OL NPs have never been investigated to remedy the critical problems of low quantum yield and low temperature stability. Currently, there exists no materials solution to make high-stability, high-efficiency oligomer nanoparticles in solid form.

To address these challenges and achieve highly stable and emissive organic solids applicable to solid-state lighting, in this chapter we show the incorporation of oligomer nanoparticles into a host crystalline matrix and formation of high-efficiency and high-stability all-organic monoliths from their powders. We observed that immobilizing these nanoparticles within a salt matrix does not help to improve their QYs. However, wrapping them in an appropriate organic crystal (in our case, sucrose) increases the QY to ~7.5 times compared to their direct solid film without using a crystal host, also accompanied by a ~3-fold improved temperature stability.

This approach brings the performance of the oligomer nanoparticles in solid state to comparable levels with that of inorganic emitters. We subsequently investigated the emission dynamics of the OL NPs integrated into the host crystal sucrose and attributed the efficiency increase to possible reversible non-covalent interactions between the organic nanoparticles and sucrose lattice. The achieved thickness, size, QY, and stability of the OL NP integrated sucrose monoliths make the oligomer nanoparticles suitable for solid-state lighting applications. With this motivation, we demonstrated a proof-of-concept LED

employing OL NP monoliths as color-converters on a blue LED chip. Considering the simplicity of our methodology along with the significantly improved QY, temperature stability, and low cost of the OL NP monoliths presented here, this approach makes the ubiquitous use of OL NPs achievable for solid-state lighting and possibly other photonic applications.

3.2 Experimental Methodology

3.2.1 Chemicals

All chemicals and solvents to synthesize OL and OL NPs were purchased from Sigma-Aldrich Chemical Co. (Germany). Sucrose was also obtained from Sigma-Aldrich Chemical Co.

3.2.2 Synthesis of 3,3′,3″,3‴-{[(1E,1′E)-2,1,3-benzothia-diazole-4,7-diylbis(ethene-2,1-diyl)]-bis(9H-fluorene-9,9,2-triyl)}-tetrakis(N,N-dimethylpropan-1-amine) oligomer nanoparticles

Before OL NP preparation, oligomer was synthesized according to the procedure reported by Pennakalathil *et al.*[150] In order to convert the OL into nanoparticles, 10 mg of oligomer was dissolved in 10 mL of THF and the resulting solution was filtered through 0.45 µm syringe filter. 1 mL of this OL solution was injected into 20 mL of deionized water slowly under sonication. After 30 min sonication, THF was removed under reduced pressure at room temperature *via* rotary evaporator.

3.2.3 Dynamic light scattering (DLS) measurements

Dynamic volume of OL NPs was measured using Malvern Nano-ZS Zetasizer. Size distribution of number was reported as the average diameter.

3.2.4 Preparation of crystals, monoliths, and films

Sucrose stock solution used in this study was prepared by dissolving sucrose (260 g) in 500 mL Milli-Q water. For the crystallization, 1, 2, 3 and 4 mL of OL NP solution (0.11 mg/mL) was mixed with the 2 mL of saturated sucrose stock solution. Water of the mixtures was evaporated on a vibration minimizing pad purchased from Sorbothane at room temperature. After a few days of drying, formation of macrocrystals was completed (OL NP crystals).

In order to obtain OL NP powders, these crystals were mechanically powdered using a mortar. OL NP monoliths for all concentrations were prepared by applying pressure. Briefly, ~80 mg of OL NP powders were placed between two stainless steel disks and a pressure of 5400 *psi* was applied using a hydraulic press for 5 min at room temperature. The thickness and size of the monoliths were measured as 0.5 and 13.0 mm, respectively. For comparison, films of OL solution in THF and OL NP solution in double distilled water (ddH_2O) were prepared by dropping 100 µL of these solutions onto a glass substrate and dried at room temperature.

3.2.5 Transmission electron microscopy (TEM)

Morphological structure of the OL NPs was investigated using a FEI Tecnai G2 F30 transmission electron microscope. Sample for imaging was prepared by dropping 2 µL of stock OL NP solution on a 200 mesh copper grid and staining with uranyl acetate (2%, w/v) for 1 min.

3.2.6 Focused ion beam scannıng electron microscopy (FIB-SEM)

Oligomer nanoparticle cross-sectional images were taken using FEI NanoSEM dual beam system. OL NPs with the different diameters were spin coated onto a silicon wafer. Prior to imaging, protective platinum layer was coated with electron beam and ion beam, respectively. Careful ion etching was performed at low ion currents and cross-sectional images were obtained after etching.

3.2.7 X-ray diffraction spectroscopy (XRD)

Crystal structures of OL NP crystal, powder, and monolith were investigated using a Panalytical X'pert Pro Multi-purpose X-Ray Diffractometer operated at 45 kV and 20 mA with Cu Kα radiation and a diffracted beam monochromator. XRD spectra were obtained between 10 $^\circ$ to 60 $^\circ$ of the 2θ angle with a step size of 0.01 $^\circ$.

3.2.8 Photoluminescence (PL) and quantum yield (QY) measurements

PL spectra of varying forms of OL and OL NPs were taken using an Ocean Optics Maya 2000 spectrometer equipped with an integrating sphere, a Xenon lamp, and a monochromator at an excitation wavelength of 400 nm. QY of solutions, films, and OL NPs in crystal, powder, and monolith forms were obtained using the method described elsewhere.[10], [156] Statistical analyses were performed using GraphPad Prism 5, and one-way ANOVA and Tukey's multiple comparisons post-tests were employed to determine the statistical difference in quantum efficiencies.

3.2.9 Lifetime and temperature dependent lifetime measurements

Time-resolved fluorescence decays of the OL NP dispersion, drop-casted film, crystals, powders and monoliths were acquired by using a PicoHarp 200 time-resolved single photon counting system (PicoQuant). The time-resolved photon count decay curves were recorded at the wavelengths where the emission maxima were observed in the PL measurements. Amplitude-averaged lifetimes were extracted by exponential reconvolution method using the FluoFit software. Temperature dependent lifetime of OL NP film and OL NP monolith were measured at 50, 100, 150, 200, 250, and 300 K using the same set-up.

3.2.10 LED preparation

The OL NP monoliths were directly placed on an Avago ASMT blue LED. The luminance was recorded under varying current flows between 10-350 mA using an Ocean Optics integrating sphere and spectrometer. Colorimetric and photometric characterizations were carried out employing in-house written codes.

3.3 Results and Discussion

Oligomer nanoparticles were prepared according to a recently reported procedure.[150] To investigate the effect of the incorporated conjugated OL NPs amount on QY, four different OL NPs embedded sucrose crystals were prepared by mixing the varying volumes (1, 2, 3, and 4 mL) of 1.3 mM aqueous dispersion of OL NPs with 2 mL of saturated sucrose solution (1.5 M). Crystals were allowed to grow slowly at room temperature over 10 d. Subsequently, the crystals were powdered by mechanical grinding and then transformed into their disc-shaped monoliths by applying a pressure of 5400 *psi*.

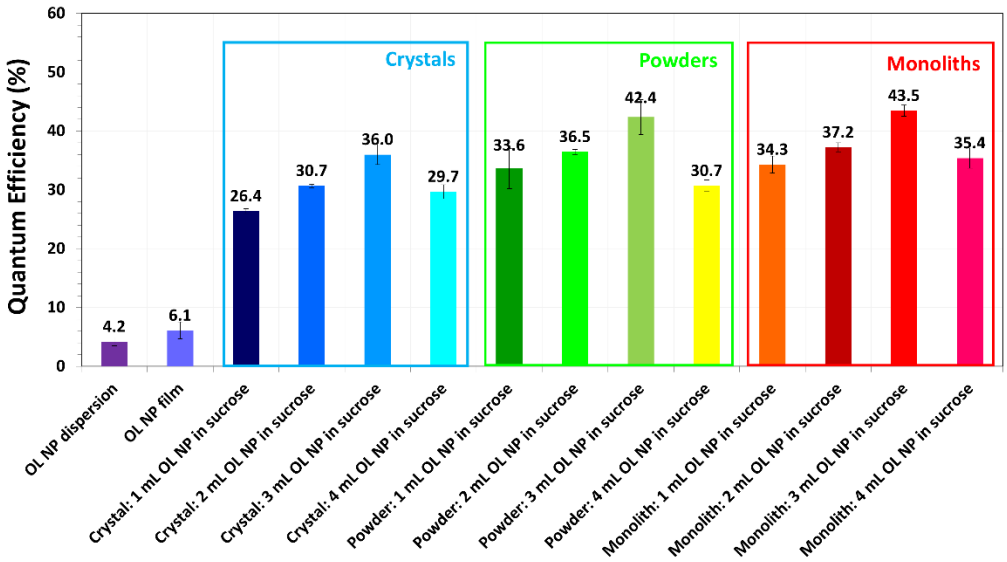

Figure 3.1. (a) Quantum yields of OL NP dispersion, OL NP drop-casted film and OL NPs as a function of concentration in crystal, powder, and monolith

forms. Reprinted with permission from Ref. [61] Copyright American Chemical Society 2016.

As shown in **Figure 3.1**, the QY is maximized in the sample immobilizing 3 mL of OL NP in crystal, powder, and monolith form. Therefore, here we mainly focus on 3 mL OL NP incorporating samples with the highest efficiency throughout the manuscript (unless otherwise stated). For this sample, we calculated the concentration of the oligomer nanoparticles to be 11.8 pmol in 1 mg of the crystals by re-dissolving the crystals in sucrose and recording the absorption spectrum. The OL NP incorporating crystals were denoted as "OL NP crystal", the powders made from these crystals as "OL NP powder", and the monoliths prepared using these powders as "OL NP monoliths". The procedure of obtaining oligomer nanoparticles and the real color images of OL NP dispersion, crystal, powder and monolith are represented in **Figure 3.2**.

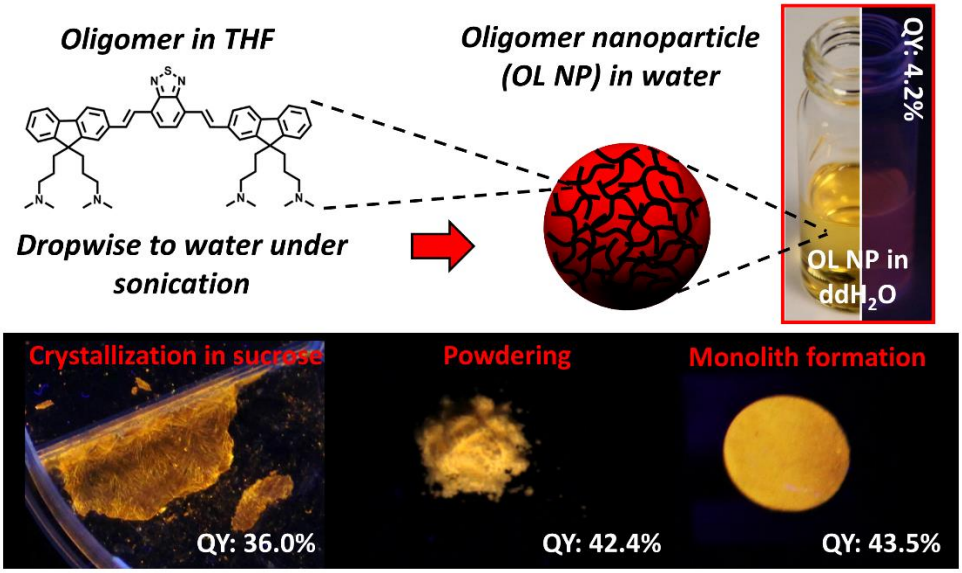

Figure 3.2. Schematic diagram depicting the preparation of oligomer nanoparticles and the real color images of OL NP in dispersion, crystal, powder, and monolith form, along with their quantum yields. Reproduced with permission from Ref. [61] Copyright American Chemical Society 2016.

The photoluminescence (PL) spectra of OL in tetrahydrofuran (THF) and their drop-casted films along with the PL spectra of OL NPs in water, their films, powders, and monoliths were measured and displayed in **Figure 3.3**. The emission peak of the oligomer solution in THF (OL solution) was monitored at 576 nm and this peak red-shifted in solid film and in nanoparticle aqueous dispersion to 596 nm (Figure 3.3a), which we attribute to the nonradiative interaction between oligomer molecules in close proximity. When we compare the PL spectra (Figure 3.3b), we observe that crystal, powder, and monolith emissions blue-shifted and became narrower compared to the OL NP dispersion and its film. Additionally, there is a more profound blue shift in powder and monolith compared to crystals.

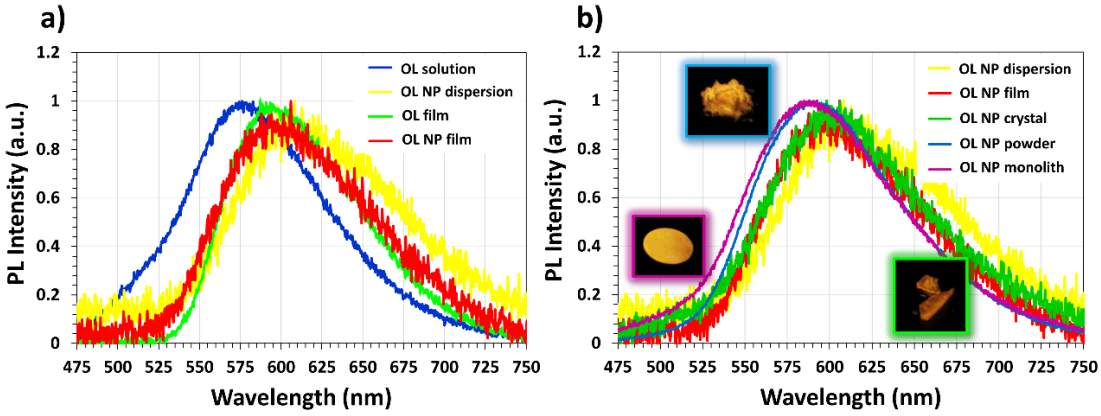

Figure 3.3. (a) Photoluminescence spectra belonging to OL solution in THF, OL NP dispersion in water, and their solid films. (b) Photoluminescence intensity of OL NP dispersion, solid-film and OL NP crystal, powder, and monolith. Insets show the real-color images of OL NP crystal, powder, and monolith. Reproduced with permission from Ref. [61] Copyright American Chemical Society 2016.

We also measured the absorption spectra of the OL NP film, powder, and monolith. Our results presented in **Figure 3.4** show no significant difference between the absorption capabilities of these materials except a slight increase in crystals, monoliths, and powders compared to OL NP film, which possibly stems from the increasing scattering of the excitation photons pumping OL NPs within sucrose matrix leading to improved absorption.

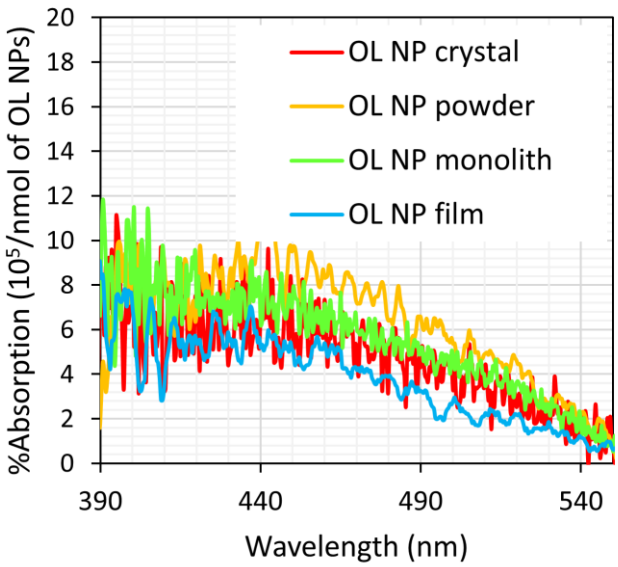

Figure 3.4. Absorption spectra of the OL NP film, OL NP crystal, OL NP powder, and OL NP monolith. These measurements were taken using an integrating sphere equipped with a Xenon lamp due to the scattering nature of these materials. Reprinted with permission from Ref. [61] Copyright American Chemical Society 2016.

We next measured the QY of OL NP dispersion, its solid-film, and crystal, powder, and monolith form of OL NP using the methodology reported in Refs. [10] and [156] The significance of QY differences were analyzed using a one-way ANOVA statistical test. As depicted in **Figure 3.5b**, the QYs of the OL NP dispersion and film turned out to be very similar and were calculated as 4.2±0.7% and 6.1±1.4%, respectively. After the crystallization of OL NP within the sucrose, the QY of the crystal (36.0±1.7%) surprisingly increased by ~6-fold compared to the nanoparticle film.

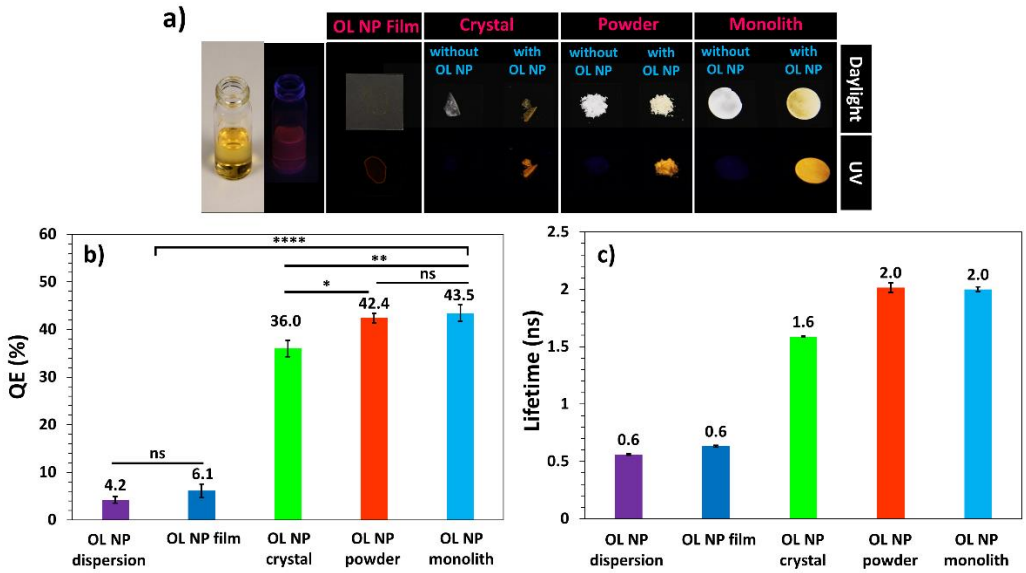

Figure 3.5. (a) Real-color photographs of OL NP in all forms along with sucrose crystals, powders, and monoliths prepared without OL NPs under daylight and UV light excited at 365 nm. (b) Quantum efficiency (ns: nonsignificant) and (c) lifetime of OL NPs in dispersion, solid film, crystal, powder, and monolith form. Reprinted with permission from Ref. [61] Copyright American Chemical Society 2016.

This significant increase in the QY clearly suggests that the sucrose molecules passivate the nonradiative transitions in the OL NPs. It is also possible that sucrose molecules separate the OL NPs, which in turn contributes to both a QY increase and blue-shifts, and narrows the emission spectrum. We also observed that powdering the crystals further increased the QY to 42.4±1.0% and the QY of the OL NP monoliths were measured to be 43.5±1.7%, which is ~7.5 times that of the OL NP film. Since we do not expect any chemical interaction or additional passivation to occur during the powdering of crystals, we hypothesize that removal of unfavorable strain effects in the crystals contributed to the QY increase in powders as well as improved light outcoupling thanks to the scattering nature of powders. Because the roughness of the powder particles significantly decreases during the monolith formation, we expect that the scattering effects weaken and QY decreases in the monoliths. However, the QYs of powders and

monoliths are still very similar, which suggests that it is mainly strain effects that influence QY increase more than scattering effect.

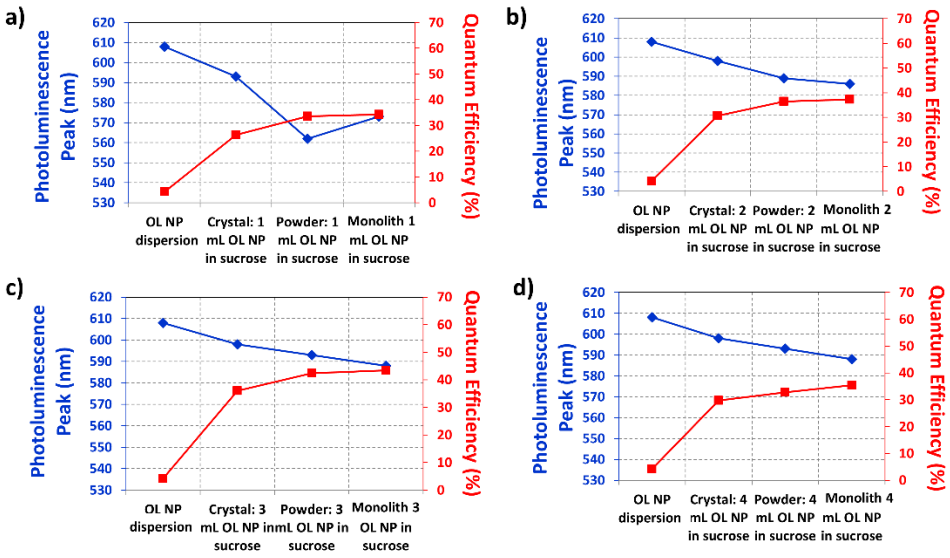

Figure 3.6. Photoluminescence peaks of OL NP crystals, powders, and monoliths as a function of OL NP incorporation along with their quantum efficiencies. Reproduced with permission from Ref. [61] Copyright American Chemical Society 2016.

In our measurements, we observed that the QY increases are correlated with the blue shift of the emission peak (**Figure 3.6 and 3.7**) suggesting a passivation mechanism, which should also affect the fluorescence lifetime of the nanoparticles. In order to reveal these dynamics, we performed time-resolved fluorescence decay measurements.

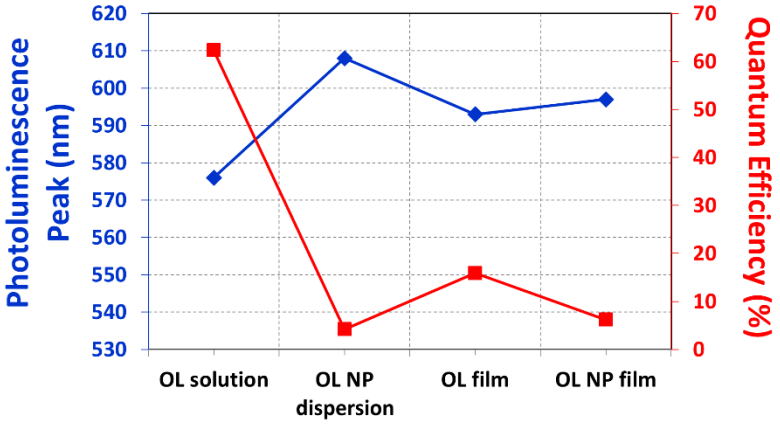

Figure 3.7. Photoluminescence peaks and quantum efficiencies of oligomer in THF, oligomer NPs in water, and their drop-casted films. Reproduced with permission from Ref. [61] Copyright American Chemical Society 2016.

The calculated lifetimes presented in Figure 3.5c showed a clear increasing pattern similar to the QY measurements for all the samples indicating an inhibition of the nonradiative processes. We also performed time-resolved fluorescence decay measurements at reduced temperatures down to 50 K (**Figure 3.8a**). We observed that the lifetime of the OL NP film lengthens more (40.4% change) with decreasing temperature while the lifetime of the OL NP monolith lengthens less (23.6% change) compared to the OL NP film. These results strongly suggest that temperature dependent nonradiative transitions such as diffusion of excitons may dominate in the OL NP film. In the OL NP monolith, however, those transitions seem to be suppressed and the nonradiative transitions with weaker temperature dependence prevail.

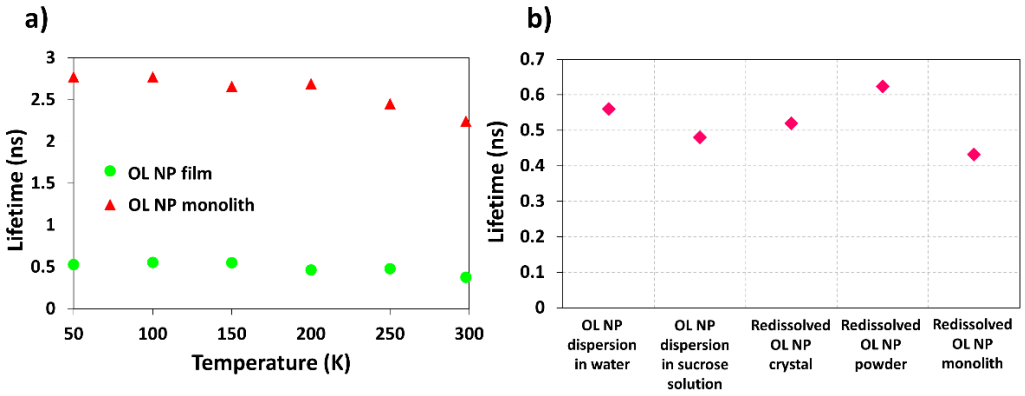

Figure 3.8. (a) Temperature dependent lifetimes of drop-casted oligomer nanoparticle film and OL NP monolith. (b) Lifetime change in re-dissolved crystal, powder, and monolith compared to OL NP dispersion in water and in sucrose solution without crystallization. Reprinted with permission from Ref. [61] Copyright American Chemical Society 2016.

The QY data along with the steady-state PL spectra and time-resolved fluorescence decay measurements show that the optical features of the OL NPs are improved upon incorporation into sucrose. These changes might stem from physical or chemical interactions between the sucrose molecules and the incorporated OL NPs. To reveal the details regarding possible interactions, we compared the fluorescence lifetimes of the OL NP dispersion, OL NP in sucrose solution (without crystallization), and re-dissolved OL NP crystal, powder, and monolith in water. As represented in Figure 3.8b, lifetimes of the re-dissolved crystal, powder, and monolith shorten and converge to the initial lifetime of OL NPs. Similarly, we observed a sharp decrease in the QY of the OL NP crystal, powder, and monolith toward the QYs of the OL NPs in the dispersion. Furthermore, we kept the OL NP sample in sucrose solution for one week and did not record any change in the lifetime and QY. Our attempts to detect any chemical interaction using Raman and X-Ray photoelectron spectroscopies have failed due to the dominance of the sucrose signal. These findings suggest that reversible physical and/or possibly noncovalent interactions (such as hydrogen bonding) between the OL NPs and sucrose molecules may be the main causes of the observed changes in the optical features.

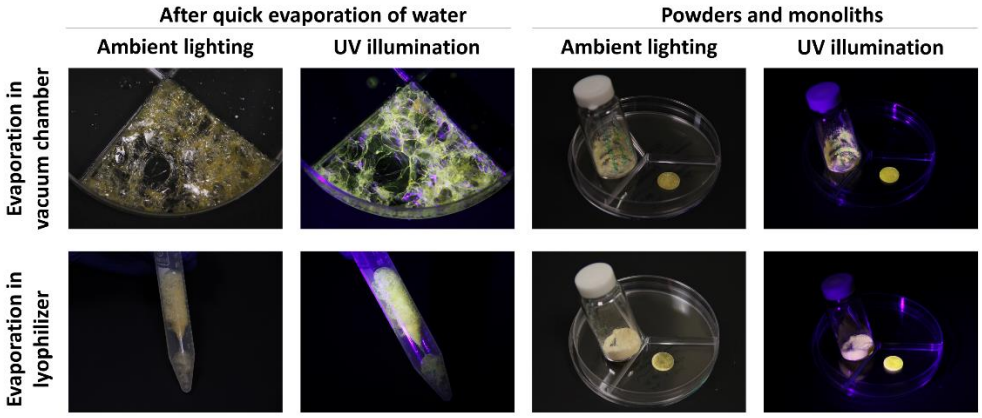

Figure 3.9. Real color photographs of the mixtures consisting of OL NP dispersion and saturated sucrose evaporated in vacuum chamber and in lyophilizer together with the photographs of their powders and monoliths under ambient lighting and UV illumination. Reproduced with permission from Ref. [61] Copyright American Chemical Society 2016.

To understand the effect of the crystal structure on the QY of the OL NPs incorporated into sucrose, we quickly evaporated the solvent of the mixture consisting of saturated sucrose solution and the OL NP dispersion using a vacuum chamber and also using a lyophilizer (**Figure 3.9**), then powdered these highly amorphous solids, formed their monoliths, and measured their QYs. We observed that the samples prepared using these fast evaporation techniques acquire similar QYs compared with the samples prepared by slowly evaporating the water (**Table 3.1**). Therefore, we conclude that having a well-defined crystal structure does not play a significant role in achieving high QYs while the passivation of nonradiative transitions in sucrose host may be the strongest reason of QY enhancement.

Table 3.1. Quantum efficiencies of the OL NP powders and monoliths that are prepared by slowly and quickly evaporating the water of OL NP dispersion and saturated sucrose mixture. Fast evaporation was carried out using two different methods: a vacuum chamber and a lyophilizer.

	Slow Evaporation	Fast Evaporation using Vacuum Chamber	Fast Evaporation using Lyophilizer
Powder	42.4% ± 1.0%	44.1% ± 0.2%	42.4% ± 1.0%
Monolith	43.5% ± 1.7%	43.3% ± 1.5%	42.9% ± 1.1%

Since the improved temperature stability of the color-converting emitters are of significant importance especially for the solid-state lighting, we studied the photoluminescence intensity change of the OL NP film and OL NP monolith at 65 °C and 130 °C, which are carefully chosen for lighting applications (**Figure 3.10** and **Figure 3.11**).

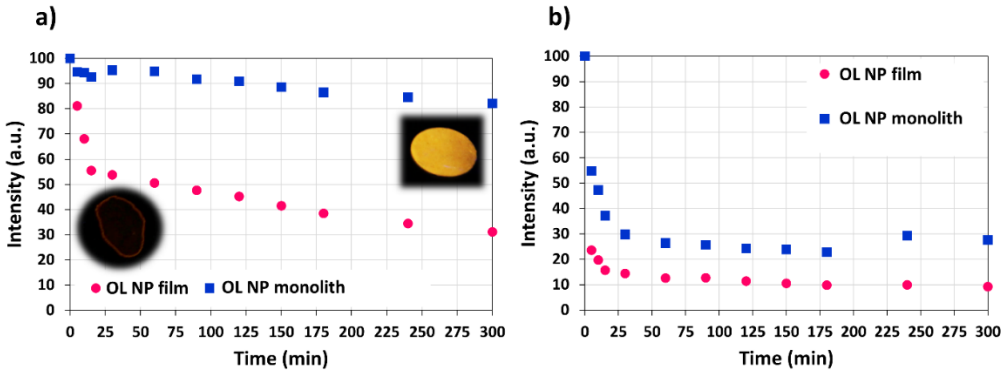

Figure 3.10. Normalized temperature stability of OL NP solid film (pink, circle) and OL NP monolith (blue, square) at (a) 65 °C and (b) 130 °C. Reprinted with permission from Ref. [61] Copyright American Chemical Society 2016.

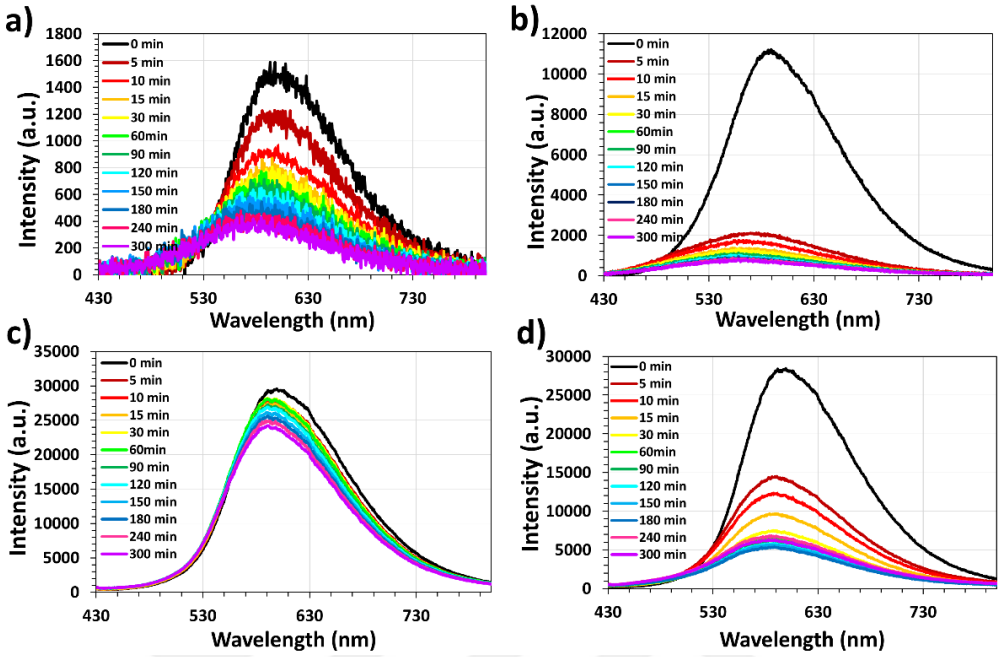

Figure 3.11. Photoluminescence spectra of the drop-casted OL NP film at (a) 65 degrees and (b) 130 degrees along with the photoluminescence spectra of OL NP monolith at (c) 65 degrees and (d) 130 degrees. Reprinted with permission from Ref. [61] Copyright American Chemical Society 2016.

These temperatures were deliberately selected because we measured the temperature of the LED chip around the location, where the monolith is placed, around 65 °C (**Figure 3.12**) using an infrared camera. Moreover, the typical junction temperature of the InGaN/GaN-based LED chips is above 130 °C.[157]

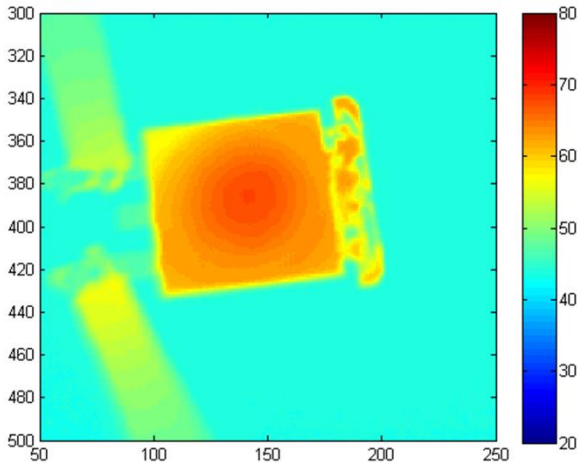

Figure 3.12. Thermal camera image of the LED driven at 350 mA. Reproduced with permission from Ref. [61] Copyright American Chemical Society 2016.

In our emission stability tests, we heated the samples on a hot plate at these temperatures without interruption and recorded their PL intensities at different time points. As shown in Figure 3.10a, the OL NP film lost 45% of its initial PL intensity within 25 min at 65 °C; on the other hand, the OL NP monolith lost only 7% of its PL intensity at the same time interval. After 5 h of exposure, OL NP film lost 69% of its PL intensity, whereas the monolith lost just 18% of its PL. The pattern was similar for the samples heated at 130 °C (Figure 3.10b). After a rapid decrease in the PL intensity, the decrease slowed down and at the end of the test, OL NP film and OL NP monolith lost 91% and 72% of their initial PL intensities, respectively. According to these results, we conclude that OL NP monoliths showed improved stability compared to the OL NP film at both temperatures indicating the suitability of this material system for solid-state lighting applications.

Subsequent to optical characterizations, we carried out the morphological characterizations starting with the transmission electron microscopy (TEM) imaging of OL NPs. Contrast difference was provided by negative staining of the TEM sample and the images are presented in **Figure 3.13a**. As depicted in this figure, OL NPs exhibited well-dispersed spherical shapes with sizes of 56.6±7.7

nm, which is also verified by dynamic light scattering (DLS) measurements to be 57.17 nm.

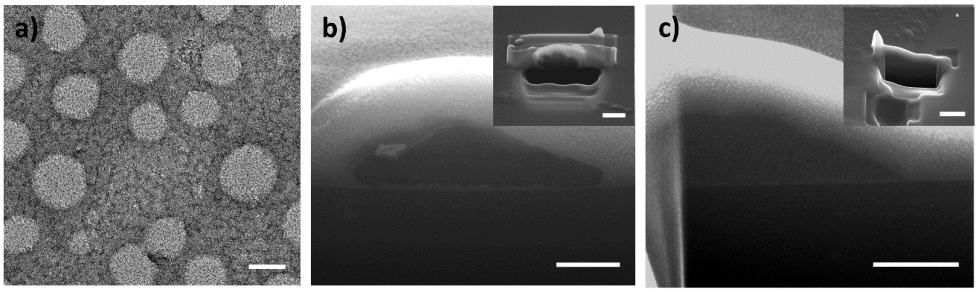

Figure 3.13. (a) Transmission electron microscopy image of OL NPs (Scale bar: 50 nm). Scanning electron microscopy image of (b) a single large OL NP (>500 nm) and (c) an aggregated area consisting of OL NPs with the diameter of 98 nm (Scale bars: 200 nm). Insets show the zoom-out of the imaged area (Scale bars: 500 nm). Reproduced with permission from Ref. [61] Copyright American Chemical Society 2016.

We also imaged the nanoparticles by using scanning electron microscopy (SEM) after etching some portion of the particle with focused-ion beam (FIB) (Figure 3.13b and c). We first etched nanoparticles with the size of 56.6 nm, which are used in the crystallization processes. However, FIB exposure etched the whole nanoparticle due to the small size that they have; therefore, we needed larger nanoparticles. For this purpose, we used two larger OL NPs with the sizes of >500 nm and 98 nm for imaging. Figure 3.13b shows the SEM image of OL NP (>500 nm) on a silicon wafer, which was etched in half using FIB. We subsequently imaged smaller OL NPs (with the diameter of 98 nm) to be more correlated with our experiments (Figure 3.13c). In this case, however, the small sized nanoparticles did not survive after FIB etching. Therefore, we took images from an aggregated area (Figure 3.13c, inset) where we observed flu filamentous structures with very low contrast in the center of the particle indicating the micelle-like structure of the nanoparticle. We believe that these structures allow for the penetration of the sucrose molecules between the oligomer molecules and help passivating the nonradiative transitions during the crystallization, which in turn helps increasing the QY. In addition to these images, we also attempted at

taking the TEM images of the OL NPs in the sucrose matrix by following the technique presented in Ref [11]; however, no contrast could be observed between the organic nanoparticles and the host medium.

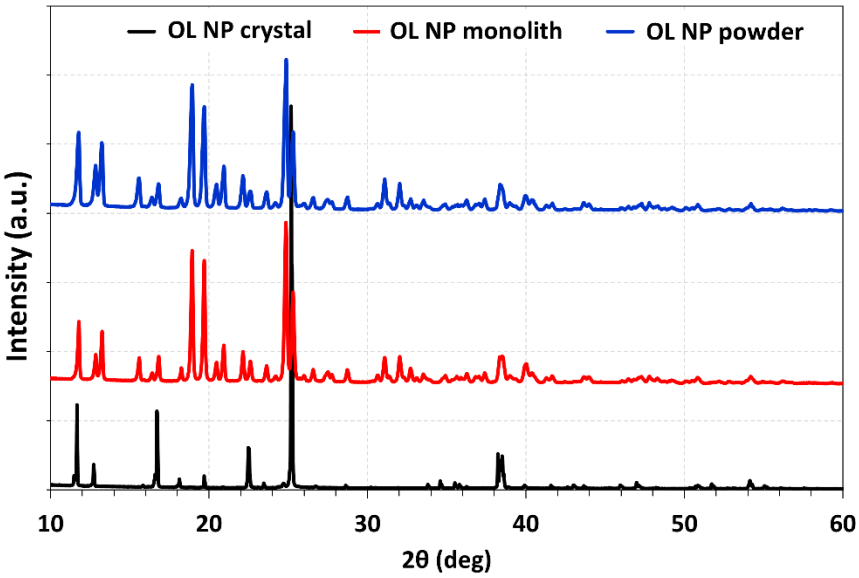

Figure 3.14. X-ray diffractogram of oligomer nanoparticle crystal, monolith, and powder. Reprinted with permission from Ref. [61] Copyright American Chemical Society 2016.

After imaging the nanoparticles, we further characterized the crystal structure of OL NP crystals, OL NP powders, and the OL NP monoliths using X-ray diffraction spectroscopy (XRD) (**Figure 3.14**). The crystal structure of sucrose was identified as monoclinic (JCPDS#24-1977). As shown in the Figure 3.14, OL NP crystals have prominent peaks at 11.6°, 16.7°, 22.5°, 25.2° and 38.3°, which are in line with the literature showing the crystal structure of sucrose.[11] We found out that powdering the crystals increases the polycrystalline character with dominant XRD signal occurring at 22.5°. Furthermore, no significant change in the XRD signal was observed after the formation of monoliths under high pressure. Thus, we conclude that this level of pressure did expectedly not change the crystal structure of OL NP powders in parallel with our observations of insignificant QY and lifetime changes upon monolith formation.

Considering the low QYs of the organic nanoparticle solid films, especially at high particle densities required for solid-state lighting applications, the methodology that we present here makes these nanoparticles suitable color-converters for solid-state lighting. With this motivation, we employed these OL NP monoliths as color-converters on a high power blue LED emitting at 460 nm to obtain a proof-of-concept LED. The spectrum of the resulting OL NP monolith integrated LED is presented in **Figure 3.15**.

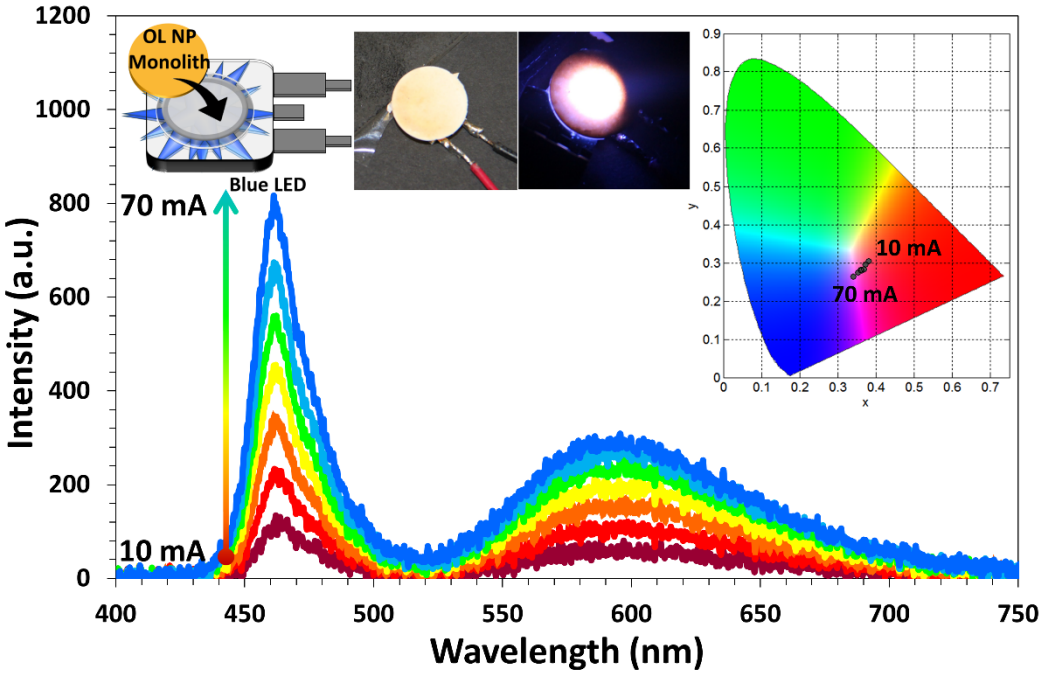

Figure 3.15. Emission spectrum of the OL NP monolith integrated blue LED at increasing currents along with the chromaticity points of the emitted light (inset, right). Moreover, representative image, real color images of OL NP monolith on LED without current flow and with current flow are presented from left to right (inset, left). Reprinted with permission from Ref. [61] Copyright American Chemical Society 2016.

Based on this data, we calculated the chromaticity coordinates and correlated color temperatures (CCTs) of the emission to characterize the shade of the white emission. Results show that the generated white light has a warm white color up to 80 mA as indicated by the color coordinates around (0.37, 0.29) and CCTs

~3200-3700 K (**Figure 3.16**). After this current level, however, the emission from the blue LED chip becomes significantly strong making the appearance of the emitted light bluish as also shown by the chromaticity coordinates around (0.20, 0.15) and CCTs of ~30,000 K.

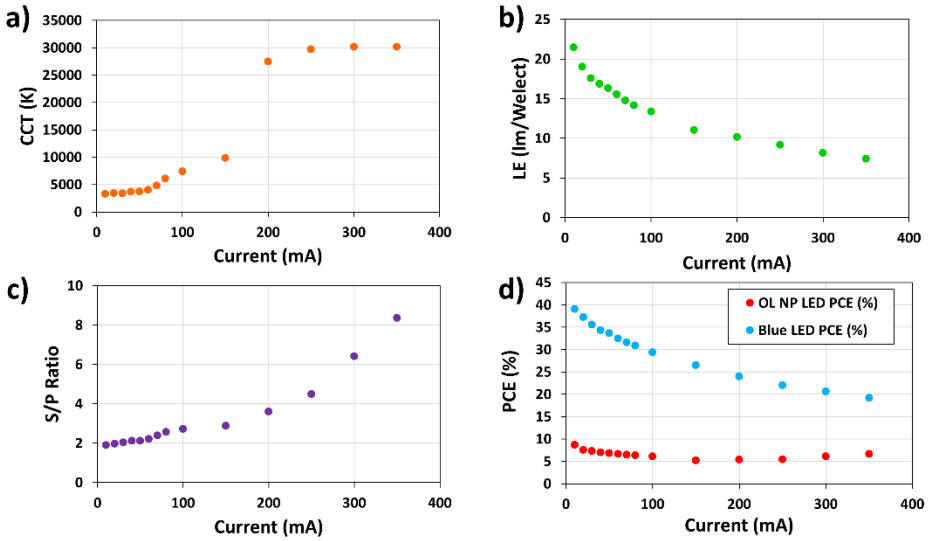

Figure 3.16. (a) Correlated color temperature (CCT), (b) luminous efficiency of the device, (c) S/P ratio and (d) power conversion efficiency of the OL NP monolith integrated LED. Reproduced with permission from Ref. [61] Copyright American Chemical Society 2016.

We also evaluated the color rendition performance of the LED by calculating the color quality scale (CQS) (**Figure 3.17**). The resulting CQS values around 70 at low current ranges indicate that this white LED exhibits mediocre color rendition capability. We later calculated the luminous efficiency of the LED to be in the range of 15-20 lm/W_{elect}. The luminous efficacy of optical radiation (LER) values of this LED escalate around 250 lm/W_{opt} at low current levels indicating a small overlap of the emission spectrum with the human eye sensitivity function. This LER performance, however, can be improved if the narrow emitting nanoparticles with PL peaks close to 550 nm are employed.

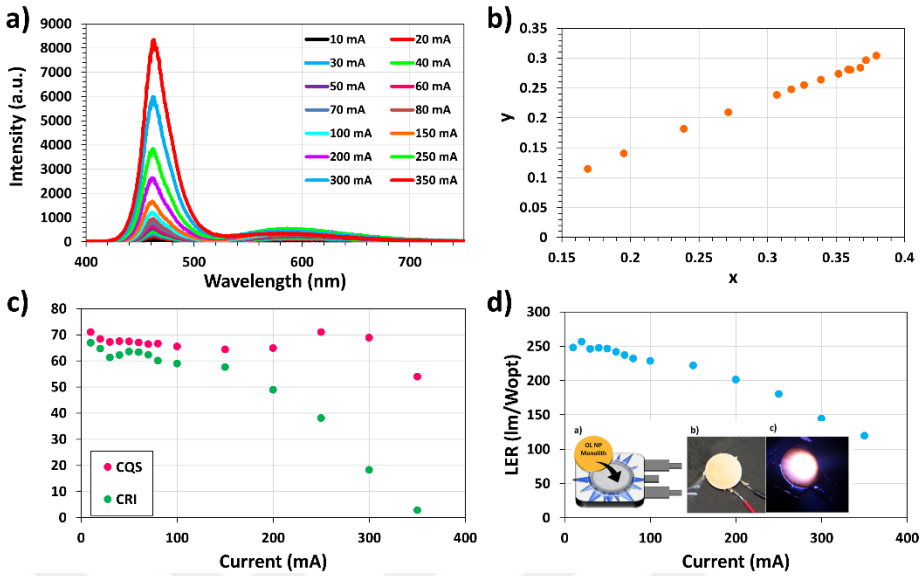

Figure 3.17. (a) Emission spectrum of the OL NP monolith integrated LED, (b) corresponding chromaticity coordinates, (c) calculated color rendering index (CRI) and color quality scale (CQS) values, and (d) luminous efficacy of optical radiation along with a schematic of the OL NP monolith integrated LED and real-color photos of the LED without and with current flow (inset). Reproduced with permission from Ref. [61] Copyright American Chemical Society 2016.

3.4 Summary

In this chapter, we show the incorporation of oligomer nanoparticles into an organic host to obtain highly efficient and highly stable fully organic color-converting monoliths suitable for solid-state lighting. In this presented approach, sucrose is used to wrap oligomer nanoparticles, and the powders of their crystals are employed to form monolith. The fluorescence quantum yields of the resulting solid monoliths reached 43.5% while that of their direct solid film remained only at 6.1%. Furthermore, we showed that these oligomer nanoparticle monoliths improve the temperature stability of the oligomer nanoparticle emission by ~3-fold compared to the bare oligomer nanoparticle solid-film. We believe that the considerably increased quantum yield and temperature stability of the oligomer emission within monoliths, in addition to the low cost and simplicity of the

preparation method presented here, will provide opportunities to deploy oligomer nanoparticles in solid-state lighting and possibly other photonic applications.

Chapter 4
Organic Macrocrystals of Colloidal Semiconductor Quantum Dots for Exciton Transfer and Polarized Emission

In this chapter of the thesis, we present our investigation on the nonradiative energy transfer (NRET) within the core/alloyed shell quantum dot immobilized macro-scale semiconductor anthracene crystals. Here, we obtained this QD-anthracene composite material system by using a simple crystallization technique based on solvent evaporation, and systematically varied the incorporated amount of QDs within the macrocystal. Results demonstrated a stronger exciton transfer with the increasing amounts of QDs. Since anthracene has several photoluminescence (PL) peaks, we investigated NRET efficiency for all of these peaks and found out that NRET efficiency changes at different emission peaks of the host anthracene, which we attribute to the variations in the QY of each emission mechanism. Moreover, we investigated the polarization anisotropy of QDs within the macrocrystals and observed an increase in the polarization ratio reaching ~2.5 at the collection angle of 60°. We finally employed these macrocrystals as color converter on a LED as a proof-of-concept demonstration.

This chapter of the thesis is mainly based on Z. Soran-erdem*, T. Erdem*, P. L. Hernandez-martinez, M. Z. Akgul, N. Gaponik, and H. V. Demir, "Macrocrystals of Colloidal Quantum Dots in Anthracene: Exciton Transfer and Polarized Emission" (2015) [158] (*equal contribution). Reprinted with permission from American Chemical Society © 2015.

4.1 Motivation

In recent years, colloidal nanocrystal quantum dots (QDs) have attracted significant attention in the field of photonics since they provide tunable and narrow-band emission spectra accompanied with broad absorption spectra, large quantum efficiency, and relatively high photostability unlike most organic dyes.[159]–[161] Owing to these unique optical properties, QDs were employed in light-emitting diodes (LEDs),[4], [161], [162] lasers,[163] photodetectors,[164] and solar cells.[165] Furthermore, their photophysical features have allowed for their use as donors and acceptors in nonradiative energy transfer (NRET).[166] These studies were reported for QDs in dispersion[167] and in solid-film.[168], [169] While working with films, QDs were frequently used in functional devices by incorporating them into polymer matrices (e.g., silicone). Another technique, recently reported by Otto *et al.*,[9] relies on the ionic crystal growth around colloidal quantum dots in salt solutions forming macrocrystals of these QDs. The attractive feature of this approach is its simplicity. The previously demonstrated crystalline host matrices[9], [13], [154] include NaCl, KCl and KBr salts and sucrose[11], which were shown to improve the robustness and stability of QDs.

In all these previous demonstrations of macrocrystals, QDs were integrated into water soluble solutes. This has substantially limited the applicability of the QD macrocrystals because only those QDs that can be dispersed in water (aqueous QDs) could be used. For that purpose, QDs either had to be synthesized directly in water, which in the end limits the usable set of appropriate materials, or they had to undergo a phase transfer *via* ligand exchange, which typically reduces the quantum efficiency and may complicate the fabrication process. This creates a major limitation because most of the high-efficiency QDs are synthesized and dispersed in nonpolar solvents. Therefore, the use of a host crystal material that can be dissolved in organic solvents and are compatible with nonpolar QDs will remove this limiting requirement and widely broaden the applicability of the QD macrocrystals. As a candidate material system, in addition to their advantages such as low toxicity, abundance, and affordability, organic crystals that are composed of benzene group gain importance because

they can be dissolved in organic solvents such as chloroform capable of dispersing nonpolar QDs.

In this chapter, we present the first account of organic crystal growth around nonpolar QDs using anthracene ($C_{14}H_{10}$) as the host crystal. In this work, we obtained large scale QD-incorporated anthracene macrocrystals by using solvent evaporation technique. Structural characterization of anthracene with and without red-emitting CdSe/CdZnSeS/ZnS alloy QDs was carried out. It was found that the inclusion of these QDs in the anthracene solution allows for the growth of larger macrocrystals of over 1 cm in one dimension, which is otherwise limited to sub-cm size. Moreover, we systematically studied NRET from the host anthracene acting as the donor to the inorganic QDs employed as the acceptor by benefiting from the strong absorption of QDs in the blue region where anthracene molecules emit strongly. Because anthracene has several photoluminescence (PL) peaks (at 429, 494, and 533 nm), we further investigated the nonradiative energy transfer and lifetime decays at every peak as a function of the QD incorporation, and the maximum NRET efficiency was found to reach 28%. Developing an exciton transfer model, we studied the quantum efficiency of the anthracene emission contributing to each PL peak. We found that the most efficient anthracene emission occurs at the peak of 494 nm. In addition, the polarization of the QD emission inside the anthracene host was analyzed and found to reveal a vertical-to-parallel polarization ratio of ~1.5 starting at 0° collection angle and increasing further to ~2.5 at 60°. Finally, as a proof-of-concept demonstration, a light-emitting diode was constructed employing these QD-incorporated anthracene crystals as tunable color-converters. This study reports for the first time the exciton transfer from the host organic crystal to the incorporated acceptor QDs together with its accompanying anisotropic emission and its application to tunable color-conversion LEDs. Since anthracene is especially important for electronics,[170] optoelectronics,[171]–[173] and physical chemistry,[170]–[174] this work may lead to new opportunities to utilize anthracene in these fields.

4.2 Experimental Methodology

4.2.1 Preparation of anthracene crystals and anthracene-QD macrocrystals

Macrocrystals were obtained by crystallization of oversaturated anthracene solution in chloroform. To prepare oversaturated anthracene stock solution, 2.08 g of anthracene was dissolved in 50 mL chloroform. After the filtration using a filter with a pore size of 0.2 µm, the concentration of the anthracene stock solution was measured to be 27.3 mg/mL. To grow anthracene crystals, 1 mL of this stock solution was dried in a vial in a laminar flow hood at room temperature. The anthracene-QD macrocrystals were formed by mixing the QD solution and anthracene stock solution. For the systematic study, 6.5, 13.1, and 19.6 mg of red emitting QDs were used and these samples were named as MC 1, MC 2, and MC 3, respectively. In order to obtain macrocrystals, 250 µL of chloroform was added to the desired concentrations of QDs (MC 1, MC2 and MC 3) after the evaporation of hexane and the dispersion was mixed with 1 mL anthracene stock solution. Chloroform was evaporated under laminar flow for two days to obtain macrocrystals.

4.2.2 Synthesis of colloidal quantum dots

4.2.2.1 Chemicals

Cadmium oxide (CdO, 99.99 %), zinc acetate ($Zn(acetate)_2$, 99.9 %), sulfur (S, 99.9 %), selenium (Se, 99.99%) and anthracene were purchased from Sigma-Aldrich in powder form. Oleic acid (OA, 90 %), trioctylphosphine (TOP, 90 %), 1-octadecene (1-ODE, 90 %), dodecanethiol (DDT, 99 %) and chloroform were bought from Sigma-Aldrich and used without any purification.

4.2.2.2 Synthesis procedure

Red-emitting CdSe/CdZnSeS/ZnS quantum dots were synthesized following the method in the literature.[36] For a typical synthesis, 1 mmol CdO, 2 mmol

$Zn(acetate)_2$, 5 mL of OA and 25 mL of 1-ODE were loaded into a 50 mL three-neck flask. After degassing the flask for nearly 2 h at 100 °C under vigorous stirring to remove the oxygen, water and other residues, the temperature was raised to 310 °C under Ar flow and a solution of TOP:Se was swiftly injected at this temperature. The TOP:Se solution was prepared *via* dissolution of 0.2 mmol of Se powder in 0.2 mL of TOP and 0.8 mL of ODE mixture. After 1 min, 0.3 mL of DDT dissolved in 0.8 mL of 1-ODE was dropwise injected. Following 20 min. of growth, a solution containing 2 mmol of S dissolved in 1 mL of TOP was injected into the system. Subsequently, the quantum dots were allowed to grow for 10 min. more to complete the synthesis. The mixture was cooled down to room temperature and precipitated with hexane/acetone twice. Finally, the resulting quantum dots were dispersed in hexane and used for further experiments. The concentration of the final QD dispersion was measured to be 26.1 mg/mL.

4.2.3 Calculation of the QD to anthracene weight ratio in the macrocrystals

The weight percentages of the QDs in the macrocrystals to the anthracene molecules were calculated by completely dissolving ~10 mg of each macrocrystal sample in 3 mL of chloroform followed by ultrasonication and measuring the absorbance spectrum. Since the absorbance of the QDs is proportional to the concentration of the QDs in the dispersion, we first calculated the concentration of the QDs in the macrocrystals by comparing with the absorbance of the QDs in dispersion (3.48 mg/mL) that were not embedded in macrocrystals. Since anthracene molecules do not absorb at 623 nm where the QDs have their first exciton peak, we used the measured absorbance levels at this wavelength in our calculations. Using the concentration information, the mass of the QDs in the dissolved macrocrystals was calculated using the volume of the solution (3 mL). Finally, the weight ratios of the QDs inside the macrocrystals to the anthracene molecules were determined as 15.4% for MC 1, 34.5% for MC 2, and 64.6% for MC 3. Correspondingly, the anthracene-to-quantum dot mass ratios are 646.8% for MC 1, 289.8% for MC 2, and 154.7% for MC 3. We estimated the molar concentration of the QDs inside crystals to be between 0.38 and 0.53 µmol/cm^3

for MC 1, between 0.81 and 1.12 µmol/cm^3 for MC 2, and between 1.44 and 1.74 µmol/cm^3. Further details regarding this calculation can be found in Supporting Information.

4.2.4 Calculation of the quantum dot molar concentration in anthracene macrocrystals

Although the exact composition of the CdSe, CdS, ZnSe, and ZnS parts cannot be known within alloyed quantum dots, an estimation leading to molar concentration in the macrocrystals is still possible (ignoring the contribution from ligands). Our calculation starts with the assumption of spherical quantum dots with diamaters of 6.5 nm.[36] This corresponds to a volume of 143.8×10^{-21} cm^3 per QD. If the alloyed QDs were totally made of CdSe, the molecular weight of these QDs would be 5035.7×10^2 g/mol. Similarly, QDs comprising of only CdS would have a molecular weight of 4177.8×10^2 g/mol. The molecular weight of the QDs comprising of only ZnSe would be 4562.1×10^2 g/mol, and that of the QDs comprising of only ZnS would be 3540.6×10^2 g/mol. Since the molecular weight values corresponding to CdSe and ZnS QDs represent two extreme cases, the exact molecular weight of the QDs should remain between two of these values. Therefore, we continue our calculations using the range defined by these two upper and lower values.

Considering the QD-to-anthracene weight ratios given in the Experimental Methods section of the paper, QD weight inside 10 mg of macrocrystal becomes 1.34 mg for MC 1, 2.57 mg for MC 2, and 3.93 mg for MC 3. This means that there are 2.66-3.78 nmol QDs for MC 1, 5.10-7.26 nmol QDs for MC 2, and 7.80-11.1 nmol QDs for MC 3 within 10 mg of macrocrystals.

The total volume of the macrocrystals is estimated by summing the total volume of the QDs and total volume of anthracene (having a density of 1.28 g/cm^3). Consequently, the volume of 10 mg macrocrystal becomes $7.0\text{-}7.1\times10^{-3}$ cm^3 for MC 1, $6.2\text{-}6.4\times10^{-3}$ cm^3 for MC 2, and $5.4\text{-}5.7\times10^{-3}$ cm^3 for MC 3. As a result, the molar concentration of the QDs in macrocrystals becomes 0.38-0.53

µmol/cm^3 for MC 1, 0.81-1.12 µmol/cm^3 for MC 2, and 1.44-1.74 µmol/cm^3 for MC 3.

Furthermore, the distance between each QD can be estimated by assuming a uniform distribution of the QDs inside the macrocrystals. Accordingly, the center-to-center distance (d_{cc}) between each QDs is calculated using d_{cc}=(Volume of Macrocrystal/Number of QDs)$^{1/3}$. The calculated d_{cc} values become 14.6-16.4 nm for MC 1, 11.4-12.7 nm for MC 2, and 9.9-10.5 nm for MC 3. Considering the size of the QDs, the surface-to-surface distance between QDs are thus estimated to be 8.4-9.9 nm for MC 1, 4.9-6.2 nm for MC 2, and 3.4-4.0 nm for MC 3.

4.2.5 Calculation of the förster radius in anthracene macrocrystals

The Förster radius is calculated using Equation 4.1,

$$R_0 = \left(\frac{9000Q \ln(10)\kappa^2 J}{128\pi^5 n^4 N_A} \right)^{1/6} \tag{4.1}$$

where Q stands for the quantum efficiency of the donor, which was measured to be 20%. κ^2 is the orientation factor taken as 2/3, n is the refractive index taken as 1.595, and N_A is the Avogadro's number, and J is the overlap integral. J is defined as in Equation 4.2, where λ stands for the wavelength, f stands for the normalized emission spectrum of the donor, and ε stands for the extinction coefficient of the acceptor in units of M^{-1}cm^{-1}.

$$J = \int \varepsilon(\lambda) f(\lambda) \lambda^4 d\lambda \tag{4.2}$$

The extinction coefficient of the QDs is estimated using Equation 4.3 where $A(\lambda)$ is the measured absorbance of the QDs in dispersion. l is the path length, which is 1 cm in our measurement. Finally, c is the molar concentration of the QDs deduced between 6.91 and 9.83 µM for CdSe and ZnS assumptions using

the absorbance measurements of the QDs with 3.48 g/mL concentration together with the molecular weights found above. The resulting values become 14.1 and 15.1 nm for CdSe and ZnS assumptions, respectively.

$$\varepsilon(\lambda) = \frac{A(\lambda)}{cl} \tag{4.3}$$

4.2.6 Details of the semi-empirical model for nonradiative energy transfer

In this case, the decay rate of the donor in the presence of the acceptor can be written as in Equation 4.4, where R_0 and r_i denote the Förster radius and the distance of the donor molecule from the acceptor QDs, respectively.

$$\gamma_{DA} = \sum_i \frac{1}{\tau_D}\left(\frac{R_0}{r_i}\right)^6 \tag{4.4}$$

Assuming that the acceptor molecules are separated from each other, we can introduce the density of acceptor QDs per donor anthracene molecule ($N_{A/D}$). Furthermore, considering that the acceptor molecules are small, we can treat the summation as an integral over the volume. As a result, the decay rate of the donor emission in the presence of acceptor can be expressed as in Equation 4.5

$$\gamma_{DA} = \int_{R_{QD}}^{\infty} N_{A/D} \Big/ \tau_D \left(\frac{R_0}{r}\right)^6 4\pi r^2 dr = \frac{4}{3}\pi N_{A/D} \Big/ \tau_D \left(\frac{{R_0}^6}{{R_{QD}}^3}\right) \tag{4.5}$$

where R_{QD} stands for the radius of the QD. Since ${R_0}^6$ is proportional to the product of quantum efficiency at the corresponding wavelength ($Q(\lambda)$) and the overlap integral (J), we can find the relative quantum efficiency of anthracene emission at the wavelengths of interest using Equation 4.6.

$${R_0}^6 \propto Q(\lambda)J \tag{4.6}$$

Toward this aim, we first fitted Gaussian functions around each emission peak, but this was not sufficient to fit to the experimental data around the main peak. Therefore, we added a Gaussian to the shoulder of the main emission for

spectral analyses of the anthracene emission (**Figure 4.1**). We did not use the Gaussian at 575 nm in our energy transfer analyses due to its very low emission intensity. The overlap integral (J) was calculated according to Ref. [175] using the absorption spectrum of the QDs in the solid-film and the sum of Gaussians fitted to the anthracene emission, which together acquire reasonable emission intensity at the wavelengths of interest.

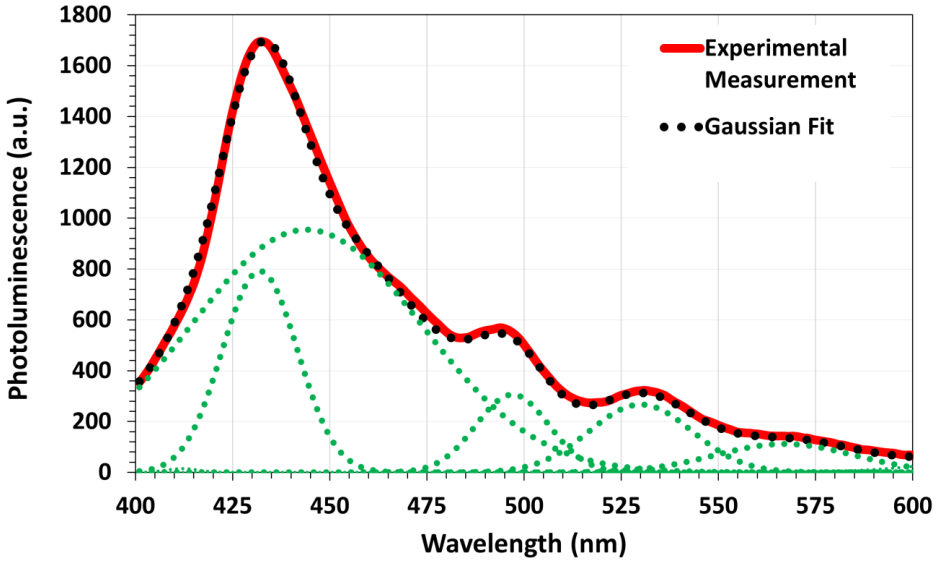

Figure 4.1. Photoluminescence spectrum of anthracene crystal (red continuous curve) along with the numerical fit carried out using the sum of Gaussian functions (black dotted curve). Individual Gaussian functions used during the fitting were presented with green dotted curves. Reprinted with permission from Ref. [158] Copyright American Chemical Society 2015.

4.2.7 Film preparation and light-emitting diodes (LED) fabrication

The films of the anthracene without QD and anthracene-QD macrocrystals (MC 1, MC 2, and MC 3) were prepared by mixing each macrocrystal powder with epoxy. Briefly, anthracene crystals and macrocrystals (MC 1, MC 2, and MC 3) were mechanically grinded to obtain fine powders. Subsequently, ca. 8.5 mg of each of these macrocrystal powders were mixed with the commercially available

two-component epoxy (Bison) of ca. 50 µL and hardened on a 1.0 cm×2.3 cm glass.

The films of the macrocrystals were placed on an Optosource LED emitting at 380 nm driven by an electrical current injection between 10 and 100 mA. The emission spectra of the LEDs integrated with anthracene-QD macrocrystal color conversion films were collected using an optical fiber and recorded employing an Ocean Optics Maya 2000 spectrometer. Color coordinates of these LEDs were calculated using an in-house written MATLAB code.

4.2.8 Optical characterizations

The optical characterizations of the anthracene-QD macrocrystal films were performed by photoluminescence (PL) and time-resolved fluorescence (TRF) spectroscopy. PL spectra of the prepared films were obtained by an Ocean Optics Maya 2000 spectrometer equipped with an integrating sphere, a Xenon lamp, and a monochromator at an excitation wavelength of 375 nm. Photoluminescence excitation spectra were recorded using the same setup; only the excitation wavelengths were changed. TRF spectra were acquired using a PicoHarp 200 time-resolved single photon counting system (PicoQuant). The time-resolved photon count decay curves were measured at the wavelengths where the emission maxima were observed in the PL measurements. The photoluminescence lifetimes were calculated using the amplitude-averaged lifetimes extracted using the FluoFit software by employing exponential reconvolution method to take the instrument response into account during the numerical fitting. The characterization of optical polarization was carried out using two different methods. In the first method, the polarization of the quantum dot emission was investigated using the approach reported in the study of Sherwood and Thomson.[176] In the second method reported in the study of Uran *et al.*,[177] the response of the instrument was determined using the emission intensity of a QD film prepared by drop-casting at various polarization angles and then the polarization behavior of the QD incorporating macrocrystals was measured. The results obtained by both methods were found to be in excellent agreement with a difference of <5%.

4.2.9 Structural characterizations

Morphological structure of the macrocrystals was investigated using optical microscopy and scanning electron microscopy (SEM). For this purpose, samples were freshly prepared and imaged using optical microscopy. For further investigation, the same samples were coated with 4 nm Au/Pd prior to imaging and then were characterized by a FEI Quanta 200 FEG SEM. The crystal structure of the macrocrystals was also studied using X-Ray diffractometry (XRD). Following the powdering of the samples using a mortar, XRD spectra of the macrocrystals were taken between 5°and 65° of the 2θ angle with a step size of 0.013° by using Panalytical X'pert Pro Multi-purpose X-Ray Diffractometer operated at 45 kV and 40 mA with CuKα radiation and a diffracted beam monochromator.

4.3 Results and Discussion

In this work, anthracene macrocrystals incorporating QDs were prepared using solvent evaporation method. Prior to our work, the growth and structure of anthracene crystals have been extensively studied.[174], [178], [179] Following the first report of anthracene crystals in 1948,[179] different crystal growth methodologies including the Bridgman–Stockbarger technique, physical vapor transfer method, and solution method were employed. Unlike the standard heat assisted solution techniques,[178] here, the solvent of the 1 mL anthracene solution (27.3 mg/mL) with and without the QDs was evaporated under laminar flow at room temperature. To systematically study the effect of the QDs on the physical and optical features of the macrocrystals, we grew macrocrystals using 6.5, 13.1, and 19.6 mg of QDs and named these samples as MC 1, MC 2, and MC 3, respectively. We estimated the molar concentration of the QDs inside macrocrystals to be between 0.38 and 0.53 µmol/cm^3 for MC 1, between 0.81 and 1.12 µmol/cm^3 for MC 2, and between 1.44 and 1.74 µmol/cm^3. After the formation of the final macrocrystals, microscopic and macroscopic structures of crystals were investigated using optical microscopy and SEM.

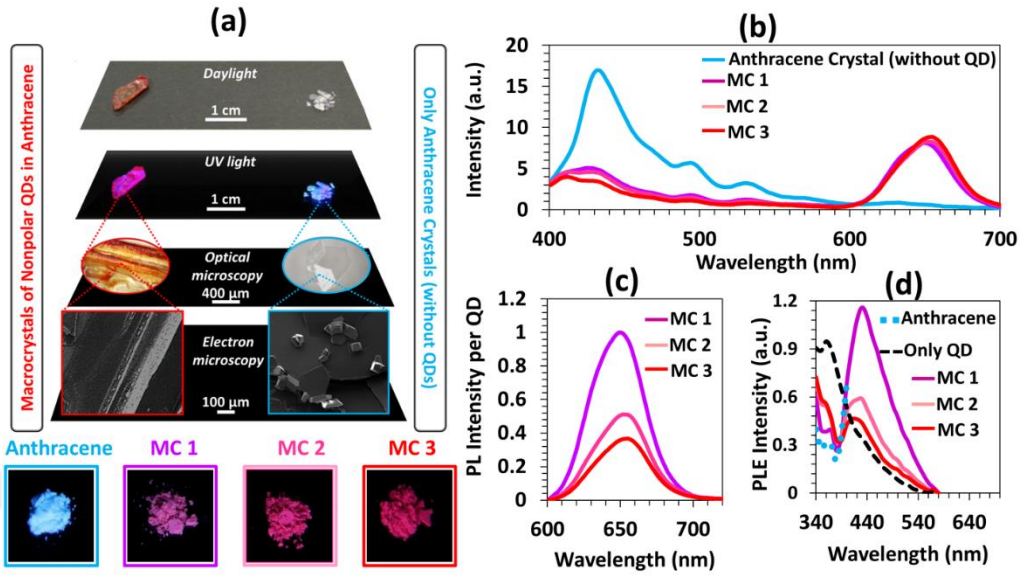

Figure 4.2. (a) Macroscopic images taken under ambient light and UV lamp illumination at 366 nm (scale bars: 1 cm). Imaging of the macrocrystal of nonpolar quantum dots in anthracene (left) and the anthracene crystals without quantum dots (right) performed by optical microscopy (scale bars: 400 µm) and scanning electron microscopy (scale bars: 100 µm) along with real color photographs of the powders belonging to the anthracene crystal, MC 1, MC 2, and MC 3 under UV lamp illumination at 366 nm. (b) Photoluminescence spectra of the films prepared using powders of the anthracene crystal alone (without QD incorporation) and MC 1, MC 2 and MC 3 (with QDs) when excited at 375 nm. (c) Normalized photoluminescence intensity per QD in MC 1, MC 2, and MC 3. (d) Photoluminescence excitation (PLE) spectra of MC 1, MC 2, and MC 3 normalized with respect to the QD amount along with that of the only QD film, all recorded in the emission wavelength range of 600-750 nm to collect the QD emission except the PLE of the anthracene crystal recorded between the emission wavelengths of 430 and 750 nm. Reprinted with permission from Ref. [158] Copyright American Chemical Society 2015.

It is apparent from Figure 4.2a that the resulting QD-anthracene macrocrystal (left) acquires a significantly larger size (cm-scale) compared to the anthracene crystals alone without QD incorporation (sub-cm) (right). Under ultraviolet illumination, the resulting emission color is red-violet in the case of QD-

anthracene macrocrystal while only anthracene crystals appear blue. As seen in Figure 4.2a, the crystal facets were obvious for the anthracene crystals. On the other hand, when QDs were embedded into the anthracene host, instead of clear crystal facets, we observed linear orientation of the crystal edges and the formation of relatively larger crystals. This suggests that QDs take role in the growth and orientation of anthracene in the crystallization process.

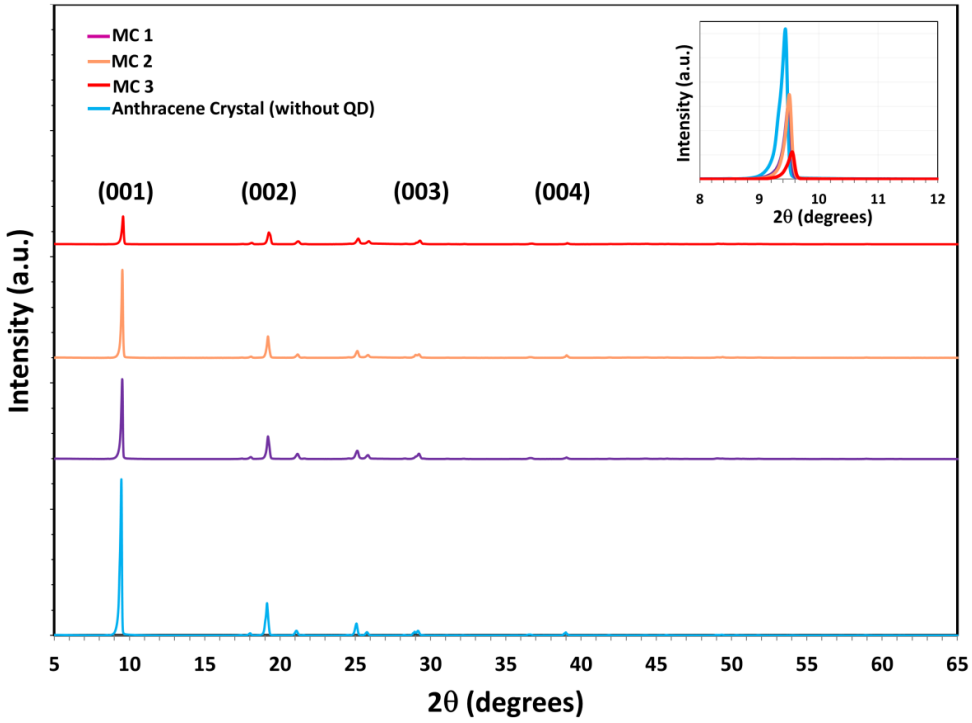

Figure 4.3. X-ray powder diffraction (XRD) pattern of the anthracene crystal and QD-embedded anthracene macrocrystals prepared using 27.3 mg of anthracene and 6.5, 13.1, and 19.6 mg of QDs for MC 1, MC 2, and MC 3, respectively. Zoom-in to the prominent peak corresponding to the (001) plane indicating the shift toward larger angles as the incorporation amount of the QDs increases (Inset). Reprinted with permission from Ref. [158] Copyright American Chemical Society 2015.

X-ray diffraction (XRD) analysis was also performed in powder form to investigate anthracene macrocrystals grown by incorporating varying amounts of QDs (**Figure 4.3**). The crystal structure of anthracene was identified as

monoclinic (JCPDS#04-0300). (001), (002), (003), (004), (005), and (006) crystal planes were observed in all anthracene crystals (**Table 4.1**) being consistent with the earlier reports.[180], [181]

Table 4.1. XRD peak locations (2θ degrees) of anthracene crystals (without QD) and anthracene-QD macrocrystals corresponding to (001), (002), (003), (004), (005), and (006) planes.

Planes	**(001)**	**(002)**	**(003)**	**(004)**	**(005)**	**(006)**
Anthracene crystal	9.44	19.11	29.15	38.97	49.34	58.88
MC 1	9.49	19.18	29.21	39.03	49.39	58.96
MC 2	9.51	19.18	29.22	39.03	49.40	58.95
MC 3	9.55	19.24	29.28	39.08	49.44	58.99

The prominent peak corresponding to the (001) plane was observed at 9.44° (d_{001}=9.36 Å) for the anthracene alone. With the QD addition, the (001) and other equivalent peaks of all macrocrystals shifted toward larger angles. For instance, the diffraction peaks for the (001) plane were observed at 9.49° (d_{001}=9.31 Å), 9.51° (d_{001}=9.29 Å) and 9.55° (d_{001}=9.25 Å) for MC 1, MC 2, and MC 3, respectively (Figure 4.3, inset). The decreasing pattern in the d-spacing suggests smaller lattice constants and increased strain within the macrocrystals owing to the QD incorporation. In addition, we observed an increase in the XRD signal between 24-28°, 41-47°, and 48-55° in the QD-embedded macrocrystals. In the report of Bae *et al.*,[36] zinc blende quantum dots were shown to exhibit XRD peaks at 27.5°, 46.0°, and 55.0°. Consistent with these XRD peaks, here we associate the XRD signals at the observed angles to the QDs incorporated into the anthracene host.

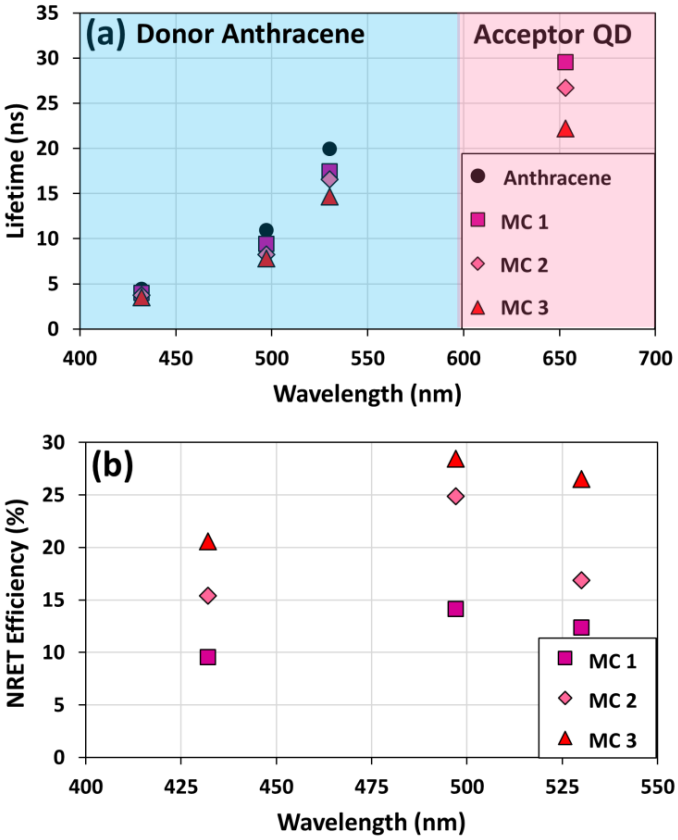

Figure 4.4. (a) Photoluminescence decay lifetimes of the anthracene emission at 429 nm, 494 nm, and 533 nm in the anthracene crystals and anthracene-QD macrocrystals (MC 1, MC 2, and MC 3) together with the lifetimes of the QD emission at 653 nm. All of the samples are excited at 375 nm. (b) The nonradiative energy transfer (NRET) efficiencies at the wavelengths where the donor lifetimes are measured. Reprinted with permission from Ref. [158] Copyright American Chemical Society 2015.

We started the optical characterization by taking the PL spectra of the anthracene crystals and the QD-anthracene macrocrystals. As shown in Figure 4.2b, the anthracene crystals exhibit PL peaks at the wavelengths of 429, 494 and 533 nm when excited at 375 nm. In the case of the QD-anthracene macrocrystals, we also observe another peak around 653 nm owing to the emission from the incorporated QDs. With the increasing incorporation amount of the QDs, we observe a slight red shift in the emission peak of the QDs

suggesting possible formation of some aggregates inside the macrocrystals. In addition, we observed a strong decrease in the emission of the anthracene host accompanied by an increase of the emission intensity per QD (Figure 4.2c). While the radiative energy transfer plays a role for this decrease in the steady-state emission intensity of the anthracene, it does not modify emission kinetics. Therefore, to investigate the nonradiative energy transfer, we analyzed the time-resolved fluorescence decays of the QDs inside the macrocrystals.

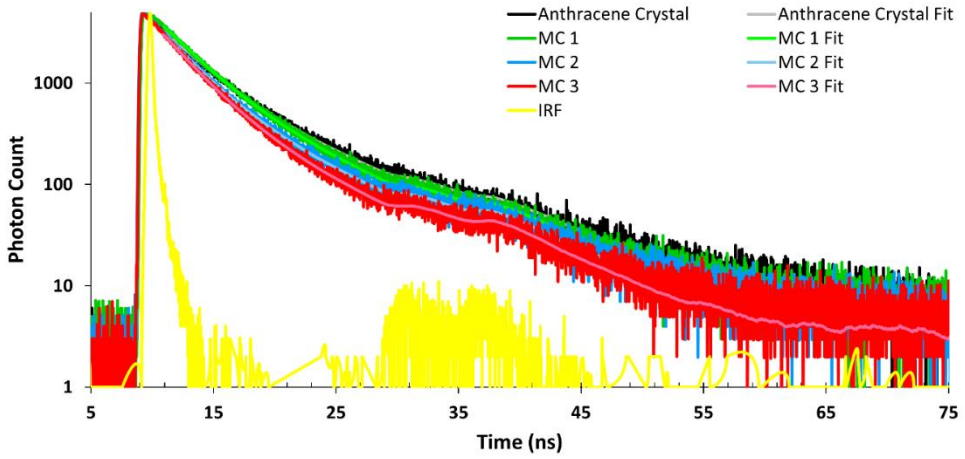

Figure 4.5. Time-resolved fluorescence lifetime decays of the anthracene crystal alone and the anthracene-QD macrocrystals (MC 1, MC 2, and MC 3) at 429 nm by exciting the samples at 375 nm given along with the instrument response function (IRF). Reproduced with permission from Ref. [158] Copyright American Chemical Society 2015.

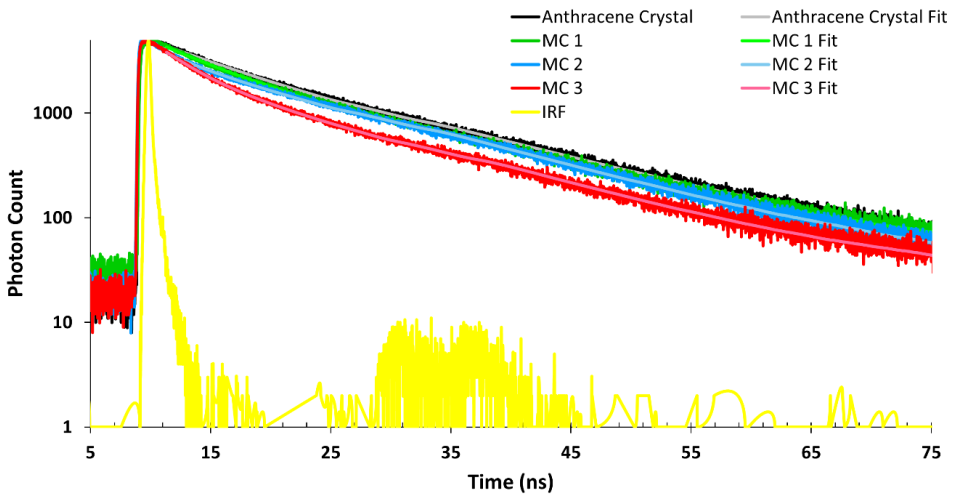

Figure 4.6. Time-resolved fluorescence lifetime decays of the anthracene crystal alone and the anthracene-QD macrocrystals (MC 1, MC 2, and MC 3) at 494 nm by exciting the samples at 375 nm given along with the instrument response function (IRF). Reproduced with permission from Ref. [158] Copyright American Chemical Society 2015.

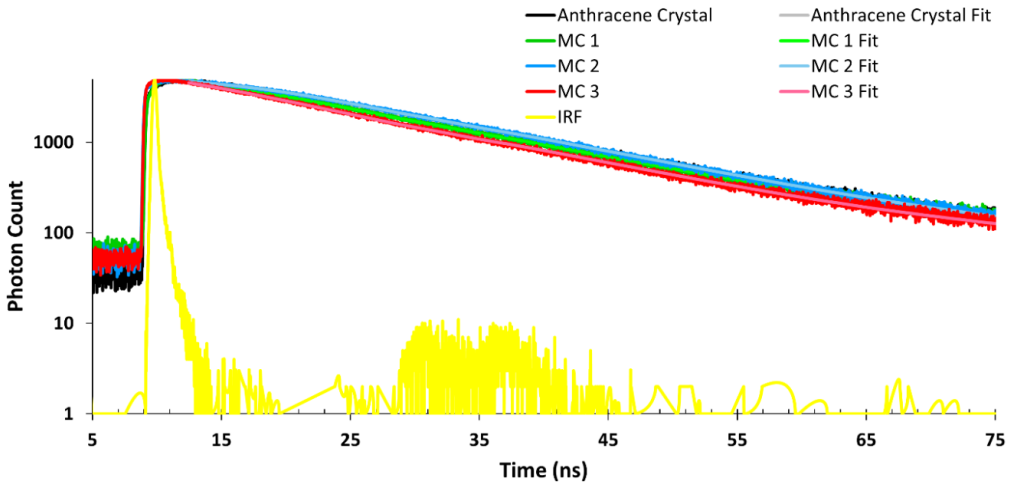

Figure 4.7. Time-resolved fluorescence lifetime decays of the anthracene crystal alone and the anthracene-QD macrocrystals (MC 1, MC 2, and MC 3) at 533 nm by exciting the samples at 375 nm given along with the instrument response function (IRF). Reprinted with permission from Ref. [158] Copyright American Chemical Society 2015.

Our results presented in **Figure 4.4a, Figure 4.5-4.7**, and **Table 4.2** show that the anthracene photoluminescence decay accelerates in the presence of quantum dots. Furthermore, the anthracene fluorescence lifetimes become shorter with the increasing QD incorporation.

Table 4.2. Time-resolved fluorescence decay lifetimes of the anthracene crystal and the macrocrystals with varying QD incorporation (MC 1, MC 2, and MC 3) at the emission peaks of 429, 494, 533, and 653 nm. The samples are excited at 375 nm.

	429 nm	**494 nm**	**533 nm**	**653 nm**
Only Anthracene	4.45 ns	11.0 ns	19.9 ns	-
MC 1	4.02 ns	9. 42 ns	17.5 ns	29.5 ns
MC 2	3.76 ns	8.24 ns	16.6 ns	26.7 ns
MC 3	3.53 ns	7.84 ns	14.7 ns	22.2 ns

On the other hand, the presented results indicate longer lifetimes of the QDs in anthracene with the increasing anthracene-to-QD mass ratio accompanied by an increased delay of the QD decay curve (**Figure 4.8**).

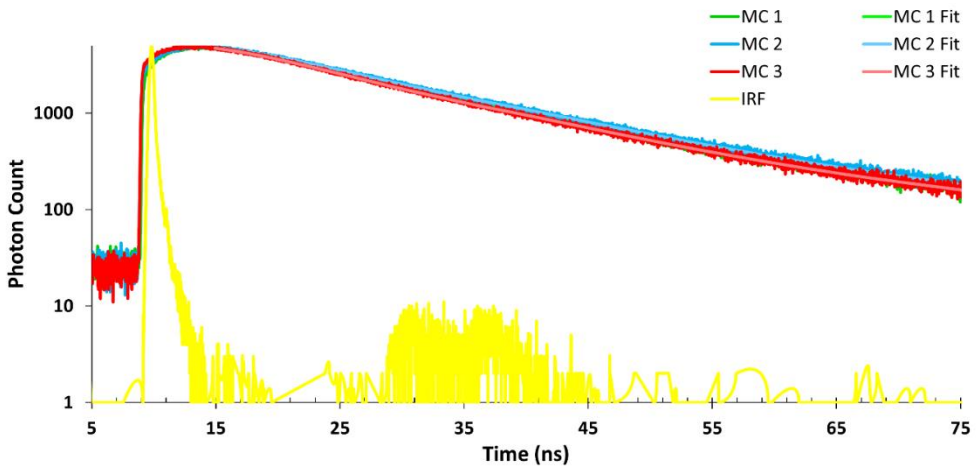

Figure 4.8. Time-resolved fluorescence lifetime decays of the anthracene-QD macrocrystals (MC 1, MC 2, and MC 3) at 653 nm by exciting the samples at 375 nm given along with the instrument response function (IRF). Reproduced with permission from Ref. [158] Copyright American Chemical Society 2015.

Complementary to the decrease in anthracene emission and increase in the emission intensity per QD, these lifetime modifications suggest that the Förster-like nonradiative energy transfer takes place from the host anthracene molecules to the embedded QDs.[182], [183] Additionally, we do not observe any fast decay component in the time-resolved fluorescence decay of the QDs suggesting that there is no significant fast charge transfer,[182] which is prevented by the ZnS shell coating of the QDs.[183] Moreover, the photoluminescence excitation (PLE) spectra of the QDs in the macrocrystals significantly differ from that of the only QDs and mimic the PLE spectrum of anthracene crystal in its absorption range (Figures 4.2(d) and **4.9**).

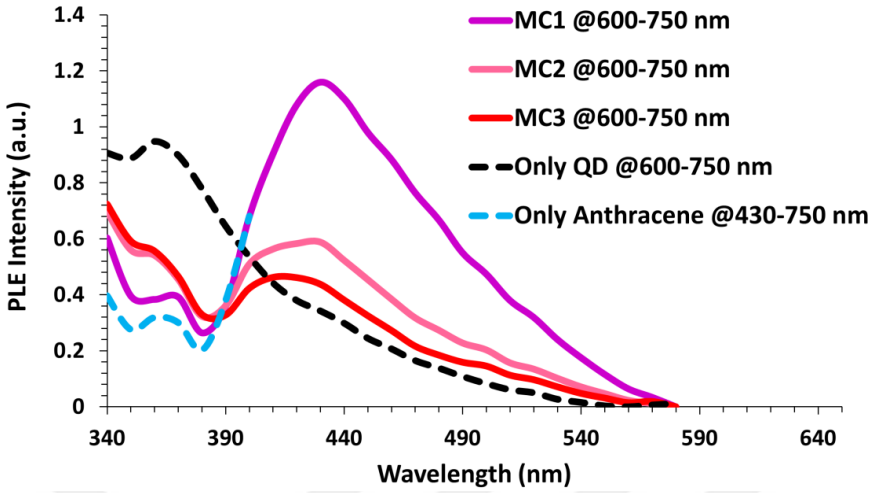

Figure 4.9. Photoluminescence excitation (PLE) spectra of MC 1, MC 2, and MC 3 normalized with respect to the QD amount in the macrocrystals along with that of the only QD film, all recorded in the emission wavelength range of 600-750 nm to collect the QD emission. PLE spectrum of the anthracene crystal was recorded between the emission wavelengths of 430 and 750 nm. Reproduced with permission from Ref. [158] Copyright American Chemical Society 2015.

However, toward shorter wavelengths where the anthracene does not absorb light, the QD emission in the macrocrystals tends to follow the trend of the only QD film. This shows that the excitation of anthracene molecules strongly triggers the emission of the QDs in the macrocrystals. Considering all of these arguments, here we conclude that Förster like nonradiative energy transfer is the most dominant nonradiative energy transfer mechanism in our macrocrystal system.

Table 4.3. Nonradiative energy transfer efficiencies (η_{NRET}) and rates (γ_{NRET}) of the macrocrystals deduced from Table 4.2 at the emission peaks of 429, 494, and 533 nm.

	η_{NRET} (%)			γ_{NRET} (ns^{-1})		
	MC 1	**MC 2**	**MC 3**	**MC 1**	**MC 2**	**MC 3**
429 nm	9.6	15.4	20.6	0.024	0.041	0.058
494 nm	14.1	24.9	28.5	0.015	0.030	0.036
533 nm	12.4	16.9	26.5	0.007	0.010	0.018

In order to analyze the energy transfer mechanism inside the macrocrystals, we systematically recorded the time-resolved fluorescence decay lifetimes at each photoluminescence peaks of the exciton donating anthracene molecules as a function of the incorporated QD amount. We calculated the nonradiative energy transfer efficiency (η) from the donor lifetime modification using the Förster theory employing Equation 4.7 where τ_D and τ_{DA} stand for the amplitude averaged lifetimes of the donor in the absence and presence of acceptor, respectively.

$$\eta = \frac{1/\tau_{DA} - 1/\tau_D}{1/\tau_{DA}} \tag{4.7}$$

At 429 nm, we observe accelerated time-resolved fluorescence decays as a result of the nonradiative energy transfer from the anthracene host to the acceptor QDs. Corresponding lifetimes decrease from 4.45 to 4.02, 3.76, and 3.53 ns for MC 1, MC 2, and MC 3, respectively (Figure 4.5, Figure 4.4a, and Table 4.2). Consequently, the nonradiative energy transfer efficiencies turn out to be 9.6%, 15.4%, and 20.6% for MC 1, MC 2, and MC 3, respectively (Figure 4.4b and Table 4.3). At 494 nm, we observe a similar acceleration pattern in the photoluminescence decays as in the case of 429 nm. The lifetime of the

anthracene emission decreases from 11.0 to 9.42, 8.24, and 7.84 ns for MC 1, MC 2, and MC 3, respectively (Figure 4.6, Figure 4.4a, and Table 4.2). These lifetimes indicate a more efficient exciton transfer process compared to that at 429 nm with η reaching 14.1%, 24.9%, and 28.5%, respectively (Figure 4.4b) and Table 4.3). At 533 nm, the variation of the lifetimes and nonradiative energy transfer efficiencies follow the same pattern as the amount of QD incorporation increases. While the emission decay lifetime of the anthracene crystals without QD incorporation is 19.9 ns, the incorporation of QD decreases this value within macrocrystals to 17.5, 16.6, and 14.7 ns for MC 1, MC 2, and MC 3 (Figure 4.7, Figure 4.4a, and Table 4.2), respectively, corresponding to 12.4%, 16.9%, and 26.5% nonradiative energy transfer efficiencies (Figure 4.4b and Table 4.3). The rates of the nonradiative energy transfer presented in Table 4.3 follow the same increasing pattern as the QD amount increases. We attribute this decrease of the donor lifetimes (and increase of nonradiative energy transfer rates) to the increased nonradiative energy transfer from the anthracene molecules to QDs going from MC1 to MC3. This is because there are more acceptor QDs available per donor anthracene molecule to feed excitons going from sample MC 1 to MC 3. Therefore, a donor anthracene molecule should transfer more excitons going from MC 1 to MC 3. This then results in shorter anthracene lifetimes going from MC 1 to MC 3. In a complementary manner, there are fewer anthracene molecules per acceptor QD going from MC 1 to MC 3. Therefore, a QD has fewer excitons transferred to it going from MC 1 to MC 3; consequently, the QD lifetime decreases as going from MC 1 to MC 3 (Figure 4.8 and Table 4.2). This observation is further supported by the shorter delays of the acceptor decay curves, decreasing PLE intensity per QD (Figures 4.2(d) and 4.9), and decreasing photoluminescence intensities per QD (Figure 4.2c) going from MC 1 to MC 3.

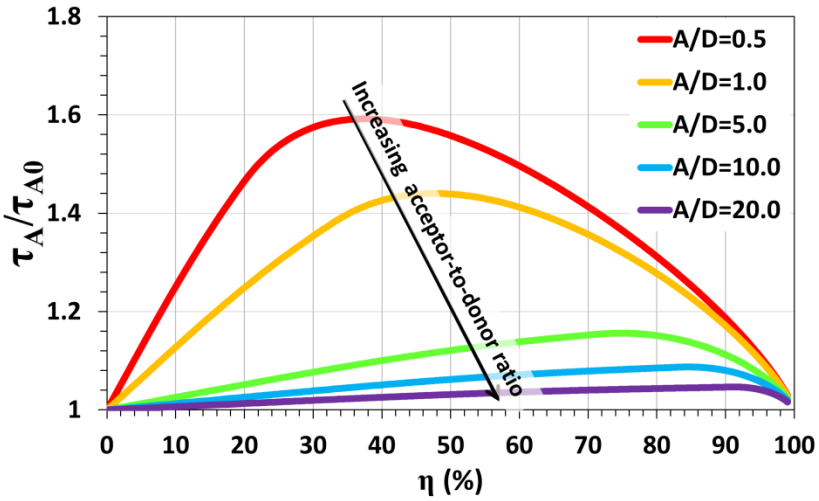

Figure 4.10. Ratio of the acceptor lifetime (τ_A) in the presence of donor to the original acceptor lifetime (τ_{A0}) in the absence of donor as a function of the nonradiative energy transfer efficiency (η). The calculations were parametrized with respect to the acceptor-to-donor ratio. These calculations are based on the decay dynamics reported in Lindhoud *et al.*[184] and use 1/e lifetimes. Reproduced with permission from Ref. [158] Copyright American Chemical Society 2015.

In our experiments, we observe that the acceptor lifetime shortens from 29.5 ns in MC 1, to 26.7 ns in MC 2, and 22.2 ns in MC 3 with increasing QD concentration in macrocrystals. These results are in parallel with the study of Mutlugun *et al.*[167] where acceptor lifetimes shortened with increasing acceptor concentration. However, they always remained longer than the acceptor lifetime in the absence of donor. Our results are also consistent with the theoretical acceptor decay model of Lindhoud *et al.*[184] showing that the acceptor lifetime shortens as the acceptor-to-donor concentration ratio increases. This model also predicts that the acceptor lifetime in the presence of donor always remains longer than that in the absence of donor (**Figure 4.10**). In our experiments, we cannot present the acceptor lifetime in the absence of donor because the host itself acts as the donor and choosing any other host material would change the photophysical characteristics of the incorporated QDs. However, in order to have an idea about the acceptor lifetime without a donor, we measured the lifetime of drop-casted QDs to be 4.90 ns, which is much shorter than the lifetime of the

QDs in anthracene macrocrystals. In addition to this, we estimated the acceptor lifetime in the absence of donor using the model in Ref. [184] to be around 9.2-13.0 ns, which is also shorter than the acceptor lifetime in the presence of acceptor.

To gain further insight of the physical mechanisms behind, we predicted the surface-to-surface distance to be between QDs between 8.4 and 9.9 nm for MC 1, between 4.9 and 6.2 nm for MC 2, and between 3.4 and 4.0 nm for MC 3, which are shorter than the predicted Förster radii (see Experimental methodology). These results indicate strengthened sharing of excitons with the increasing QD concentration. As a consequence, increasing the QD concentration decreases the number of excitons received by each QD leading to shorter acceptor lifetimes. However, these transferred excitons to QDs still make the acceptor lifetimes in the macrocrystals longer compared to the case of without donor.

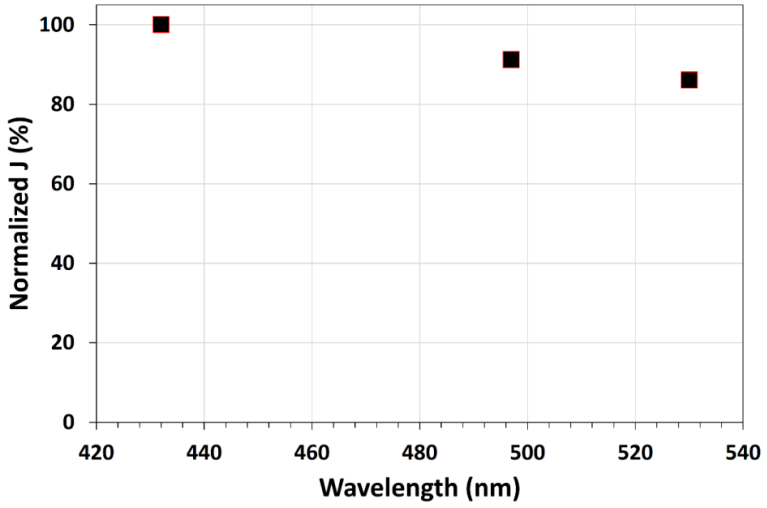

Figure 4.11. The overlap integral between QD absorption and individual emission mechanism of anthracene at 429, 494, and 533 nm. Reprinted with permission from Ref. [158] Copyright American Chemical Society 2015.

To reveal the physical reasoning behind the observation that the nonradiative energy transfer at longer wavelengths occurs more efficiently compared to 429 nm, we investigated the relation between the overlap integral (J) and the quantum yield at the wavelength of interest ($Q(\lambda)$) by assuming the random

distribution of exciton donating anthracene molecules and the acceptor QDs. The details of our semi-empirical model are presented in Experimental Methodology section. Our results summarized in **Figure 4.11** show that the overlap integral remains unaffected although the absorption of the QDs is stronger at shorter wavelengths. This is mainly because of the 4^{th} power dependence of the overlap integral on the wavelength. Subsequently, we calculated the normalized Förster radius (R_0^6) (**Figure 4.12**a), and then calculated normalized quantum efficiency (Figure 4.12b). Here, we observe that the quantum efficiency takes its highest value for all the samples at 494 nm where the nonradiative energy transfer occurs most efficiently. Considering the wavelength dependence of the overlap integral and quantum efficiency, we conclude that the difference of the nonradiative energy transfer efficiency is essentially caused by the difference in the quantum efficiency at each wavelength, reaching its highest value at 494 nm.

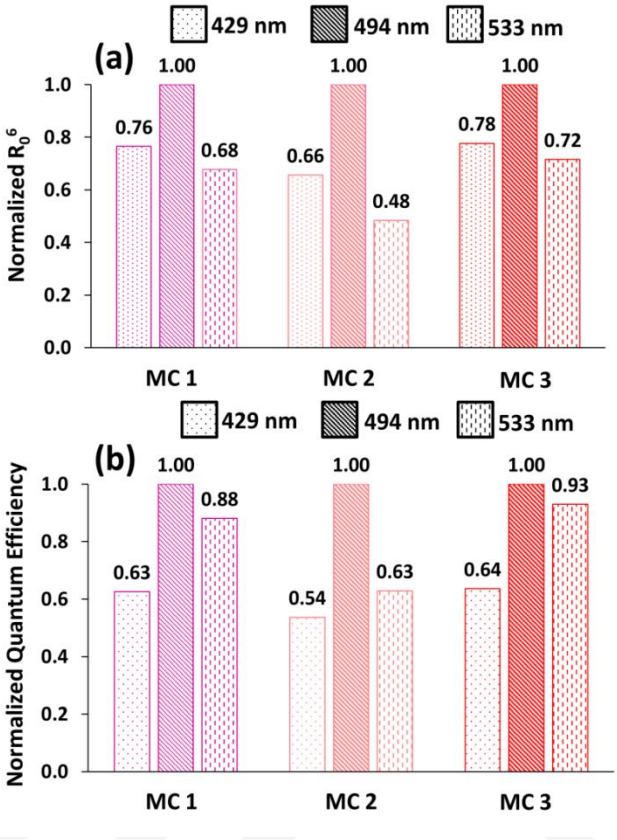

Figure 4.12. Normalized (a) R_0^6 and (b) relative quantum efficiency of the anthracene emission calculated using Equation 4.6 and the overlap integral between the anthracene emission and the QD absorption at various emission wavelengths for MC 1, MC 2, and MC 3. Reproduced with permission from Ref. [158] Copyright American Chemical Society 2015.

Since the optical properties of the anthracene are anisotropic,[185], [186] their macrocrystals might be expected to enhance the emission anisotropy of the incorporated QDs. To examine this hypothesis, we systematically investigated the polarization of the emitted light from the QDs that are immobilized in single anthracene-QD macrocrystals (not in powdered form). Here we employed a single cm-scale macrocrystal taken from the batch of MC 3 because of its larger size making the optical anisotropy measurements easier. Our results show that when the photons emitted normal to the surface of the anthracene-QD macrocrystal are collected, the ratio of the perpendicular polarization to the parallel polarization was measured to be ~1.50 (**Figure 4.13** and **4.14**a). Increasing the

collection angle to 30°, no significant change in the anisotropy of the QD emission was observed (Figure 4.13 and 4.14b). A further increase of the collection angle to 60° improved the polarization ratio to ~2.50 (Figure 4.13 and 4.14c). This observed anisotropy in the QD emission can either stem from the anisotropic extraction of electromagnetic radiation at different polarizations or from the emission rate difference caused by the anisotropy in the refractive index of the medium. One of the important indicators of the latter mechanism is the difference of the photoluminescence decay lifetimes at different polarizations. To identify the governing effect in our system, we investigated the emission dynamics of the QDs for both of the polarizations and did not measure a noticeable difference in the lifetime, which suggests that the main source of the observed anisotropy is the extraction efficiency difference rather than the modification of spontaneous emission rate.

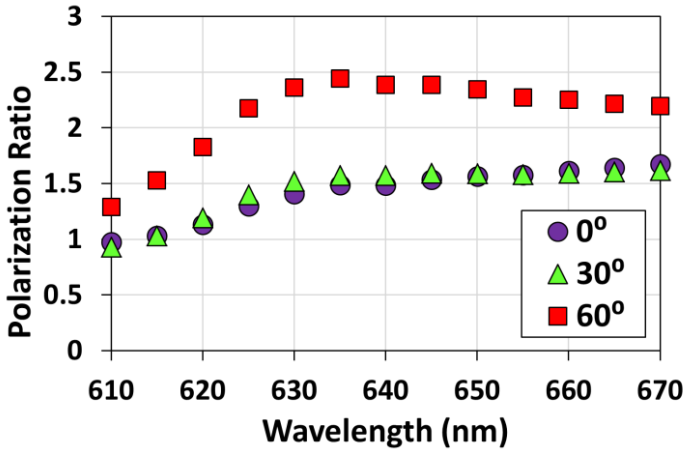

Figure 4.13. The ratio of polarizations of the QD emission within MC 3 at different collection angles. Reprinted with permission from Ref. [158] Copyright American Chemical Society 2015.

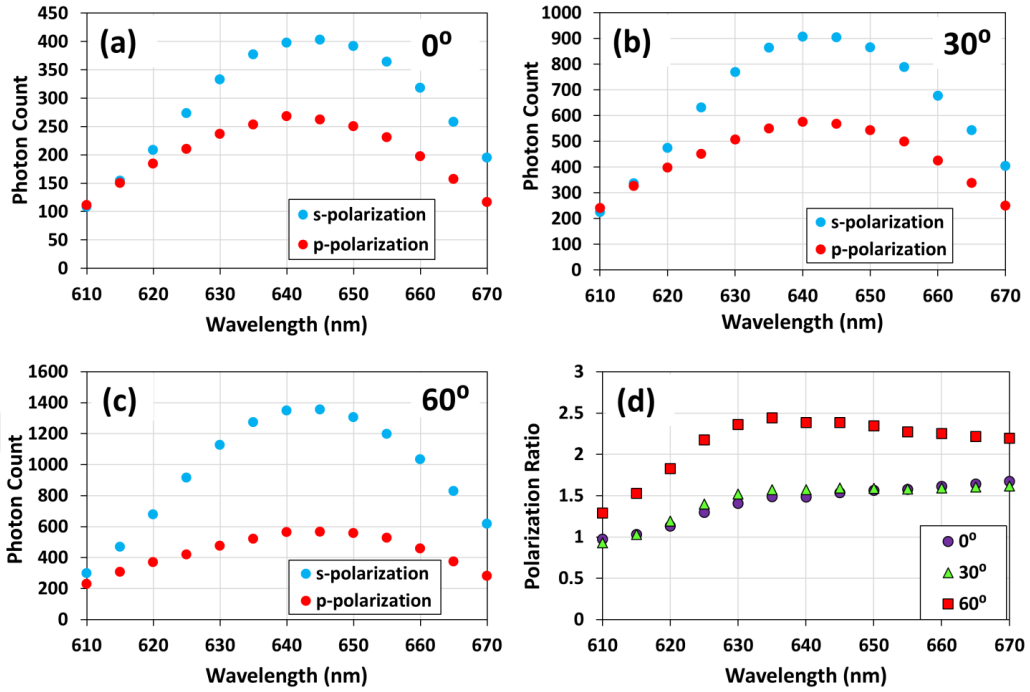

Figure 4.14. Emission spectra of the QDs within the anthracene macrocrystals at perpendicular (s) and parallel (p) polarizations at the collection angles of (a) 0°, (b) 30°, and c) 60° when excited at 375 nm. (d) The ratio of polarizations at different collection angles. Reproduced with permission from Ref. [158] Copyright American Chemical Society 2015.

Finally, we present a proof-of-concept demonstration of these anthracene-QD macrocrystals as color enrichment films on a commercially available LED emitting at 380 nm. The photons emitted from the LED at this wavelength were strongly absorbed by both the anthracene molecules and the QDs in the macrocrystal. As a result of the photoluminescence of the anthracene and QDs and the nonradiative energy transfer between them, the color conversion results in the emission spectra in **Figure 4.15** for MC 3 LED (and **Figure 4.16**a-c for MC 1, MC 2, and MC 3 LEDs) and the corresponding color coordinates presented in Figure 4.16d. The results show a trend in the change of the obtained color as the incorporated QD amount varies, as expected, due to the both radiative and nonradiative energy transfer. This proof-of-concept demonstration indicates that

the anthracene crystal is a good host for the QDs to be integrated into color conversion LEDs thanks to its compatibility with the transparent epoxies used by the industry.

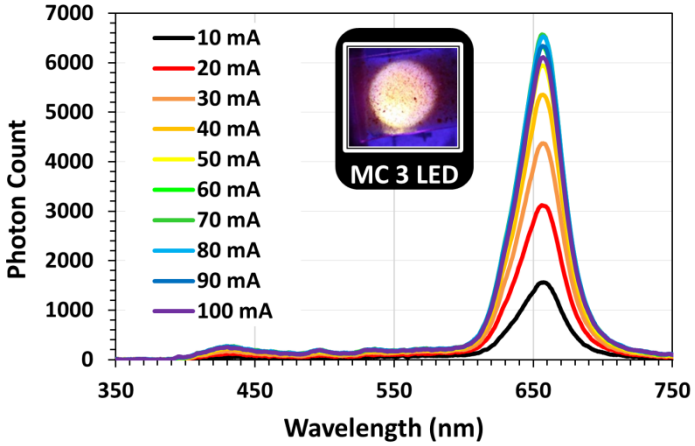

Figure 4.15. Emission spectra belonging to the color converting powdered film of MC 3 on a UV LED emitting at 380 nm driven by 10-100 mA along with its real color photograph. Reproduced with permission from Ref. [158] Copyright American Chemical Society 2015.

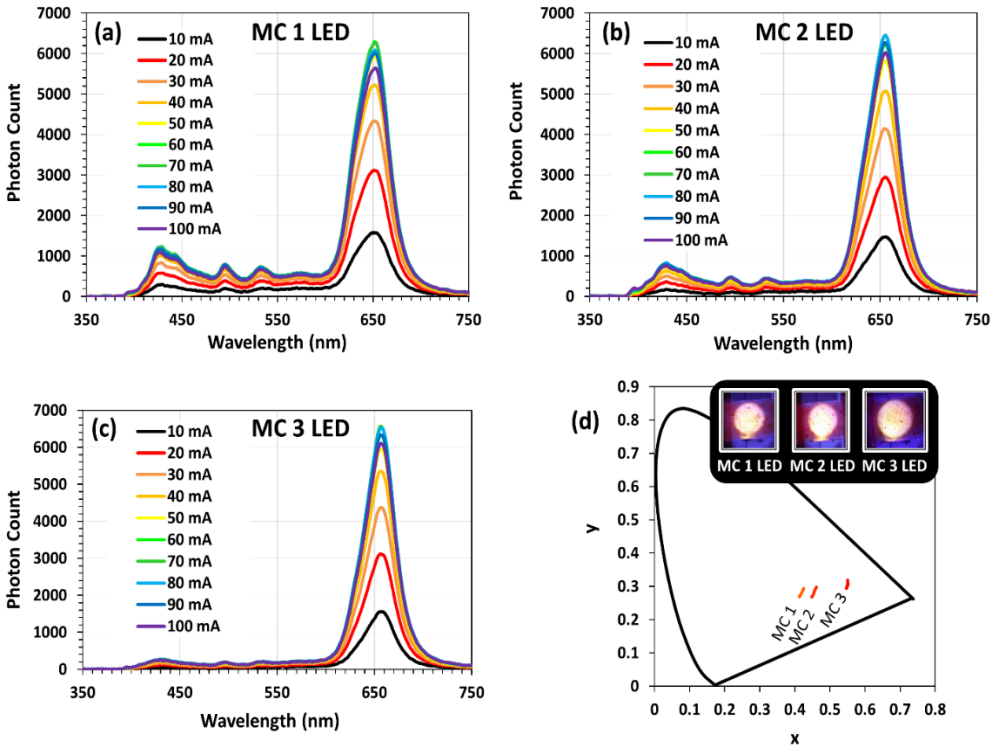

Figure 4.16. Emission spectra belonging to the color converting powdered films of (a) MC 1, (b) MC 2, and (c) MC 3 on a UV LED emitting at 380 nm driven by 10-100 mA. (d) Corresponding chromaticity coordinates of the light emitted from the LEDs employing the anthracene-QD macrocrystal powders as the color conversion film together with color photographs of the MC 1 LED, MC 2 LED, and MC 3 LED. Reprinted with permission from Ref. [158] Copyright American Chemical Society 2015.

4.4 Summary

In summary, in this chapter we demonstrated anthracene-QD macrocrystals to elucidate the interaction of the QDs within the host anthracene crystals. First, we carried out structural characterizations using optical and scanning electron microscopies. We observed that the QD incorporation affects the crystallization process of anthracene and leads to the formation of larger macrocrystals. Subsequently, we investigated the nonradiative energy transfer dynamics where the anthracene and the QDs serve as the exciton donating and accepting entities

in the macrocrystal, respectively. Our results showed that the photoluminescence lifetime of the anthracene molecules decreases with the increasing QD incorporation, indicating stronger exciton transfer. Moreover, we found that the anthracene does not emit most efficiently at the main photoluminescence peak at 429 nm in the presence of the QDs inside the macrocrystals, but instead the highest quantum efficiency occurs at 494 nm. In addition to this, the polarization anisotropy of the QD emission was observed at various collection angles. We found that these QDs exhibit a ~1.5 polarization ratio at the surface normal collection, while this number increases to ~2.5 at the collection angle of 60°. Finally, we used this nonradiative energy transfer concept on a color conversion LED employing the anthracene-QD macrocrystal as the color conversion film and demonstrated color tunability as a function of the incorporated QD amount. We believe that the findings of this study may open up new possibilities for employing crystalline organic semiconductors such as anthracene in the field of colloidal photonics.

Chapter 5
Highly Monodisperse Dual-Modal Colloidal Magnetite Nanocubes for MRI

In this part of the thesis, we present our study on the synthesis of highly crystalline and highly monodisperse colloidal iron oxide nanocubes along with their potential use for dual-modal MRI. Here, we colloidally synthesized monodisperse iron oxide nanocubes with the diameter of ~9.7 nm. Structural characterizations revealed that the crystal structure of these nanocubes is magnetite. Moreover, our magnetic characterizations demonstrated that these iron oxide nanocubes can simultaneously enhance the contrast in T_1- and T_2-weighted MR images, which holds great promise as dual-modal contrast agents.

This chapter of the thesis is mainly based on V. K. Sharma, A. Alipour, Z. Soran-Erdem, Z. G. Aykut, and H. V. Demir, "Highly monodisperse low-magnetization magnetite nanocubes as simultaneous T_1 –T_2 MRI contrast agents," *Nanoscale*, (2015). [187] Reprinted with permission from The Royal Society of Chemistry © 2015.

5.1 Motivation

Magnetic nanoparticles have been used as contrast agents for magnetic resonance imaging (MRI),[101], [188] drug delivery vehicles,[189] and in magnetic separation.[190] Among them, MRI is one of the most powerful medical diagnostic tools because it can provide images in a noninvasive manner together with real-time monitoring capability featuring excellent anatomical details based on the soft tissue contrast and functional information.[191] Different than the X-rays and computerized tomography (CT), MRI does not require ionizing radiation. In this technique, static magnetic field is used as source and generated from a series of electro-magnetic coils. After applying magnetic field, some of the

resonance frequency waves are absorbed by the targeted atomic nuclei and these energy levels change basically depending on the type, density, distribution, and arrangement of the protons. This process is referred as the "excitation". Afterwards, magnetic field is turned off, and the atomic nuclei return to their equilibrium state and release the absorbed energy. By processing this energy difference, MR images are constructed in white and black colors.[192]

The sensitivity of MRI can be greatly improved by using contrast agents that enhance the contrast of the region of interest from the background. Following the excitation of protons and turn off the magnetic field, MR signal is lost within a short time (~a few seconds), and this duration is referred as the "relaxation time". Considering this phenomenon, the MRI contrast agents are generally categorized according to their effects on longitudinal (T_1) and transversal (T_2) relaxations, and their respective ability is referred to as longitudinal (r_1) and transversal (r_2) relaxivity. The region where T_1 relaxation takes place appears brighter, whereas T_2 relaxation results in a darker contrast in the MR images. T_1-based contrast agents are thus called as positive contrast agents, whereas T_2 counterparts are also known as negative contrast agents.

Superparamagnetic iron oxide (SPIO) nanoparticles (NPs) with strong magnetic moments are the prevailing T_2 contrast agents, especially in the imaging and detection of lesions from normal tissues.[193] The significant drawbacks of these T_2 contrast nanoparticles are, however, magnetic susceptibility artifacts and negative contrast effects, which may limit their clinical applications. In contrast, T_1 imaging, typically using paramagnetic materials as the contrast agents, provides an excellent resolution between tissues due to their high signal intensity. Gadolinium (Gd) and manganese (Mn) based species are the most commonly used T_1 contrast agents in clinics.[194], [195] With unique advantages of their own, combining T_1 and T_2 imaging capabilities into a single type of contrast agent for MRI attracts considerable interest because this can give accurate diagnostic information. As a result, this creates strong motivation for designing new strategies to obtain synergistically enhanced T_1 and T_2 dual-modal contrast agents (DMCAs) for MRI. There are few reports[19], [196]–[199] on the DMCAs with both T_1 and T_2 capabilities for MRI. $Mn_xFe_{1-x}O$

nanocrystals have been reported as potential DMCAs by different groups.[196], [197] It was found that a specific composition results in simultaneous T_1 and T_2 contrast enhancement effects, which stems from different magnetic moments of the constituent Mn^{2+} and Fe^{2+} ions.[200] Gadolinium-labeled magnetite nanoparticles (GMNPs)[198] synthesized *via* conjugation of gadolinium and magnetite nanoparticles have also been reported as potential DMCAs. Zhou *et al.*[19] demonstrated monodisperse gadolinium iron oxide (GdIO) nanoparticles as DMCAs synthesized using a magnetically decoupled core–shell design.[201] In this design, GdIO nano-particles were obtained by embedding the paramagnetic Gd_2O_3 species into superparamagnetic Fe_3O_4 nanoparticles. However, although gadolinium (Gd)[202] has been the most popular choice among the paramagnetic metals, it has been recently linked to a medical condition known as nephrogenic systemic fibrosis (NSF).[194] For obvious reasons, this has led to concerns over the safety of Gd-based T_1 contrast agents in MRI applications.

Iron oxide NPs are still considered to be the best materials for MRI applications.[203] They are more biocompatible than Gd and Mn based materials because iron species are rich in human blood, which are mostly stored as ferritin in the body. Cytotoxicity investigations also confirmed that the iron oxide NPs are well tolerated by the human body.[204]–[207] However, common iron oxide NPs are not appropriate for T_1 MRI contrast agents. Although ferric (Fe^{3+}) ions having 5 unpaired electrons increase the r_1 value, the high r_2 of iron oxide nanoparticles derived from innate high magnetic moment prevents them from being utilized as T_1 contrast agent. This problem can be resolved by decreasing the size of the magnetic nanoparticles. The magnetic moment of magnetic nanoparticles rapidly decreases as their size decreases due to the reduction in the volume magnetic anisotropy and spin disorders on the surface of the nanoparticles. Recently, Kim *et al.*[208] reported 3 nm sized spherical iron oxide nanoparticles as a potential candidate for T_1 contrast agents, with high r_1 relaxivity of 4.78 $mM^{-1}s^{-1}$. On the other hand, Lee *et al.*[207] reported extremely high r_2 relaxivity (761 $mM^{-1}s^{-1}$) for the ferrimagnetic iron oxide nanocubes of 22 nm size. Very recently, Li *et al.*[18] reported dual-modal MRI contrast capabilities of ultrasmall iron oxide nanoparticles. They reported high longitudinal relaxivity r_1=8.3 $mM^{-1}s^{-1}$ but the transverse relaxivity was comparitively lower

r_2=35.1 $mM^{-1}s^{-1}$. A careful observation of the result suggests that if we increase the size of the iron oxide NPs, r_1 relaxivity will decrease and r_2 relaxivity will increase. The MR relaxivity is strongly related to the size and shape of the nanoparticles. Zhen *et al.*[209] observed that iron oxide nanoparticles with cubic geometry possess high relaxivity values (up to 4 times stronger) in comparison with the spherical counterparts. Therefore, size- and shape-controlled synthesis of uniform nanoparticles is critical for the fine control of MR relaxivity. In the previous studies, iron oxide nanoparticles have not been reported as efficient dual-modal contrast agents in MRI. The issue is, if we decrease the size too much they compromise the T_2 contrast capabilities of these NPs and *vice versa*. Recently, Zhou *et al.*[210] regulated the balance of T_1 and T_2 contrast by controlling their structure and surface features, including morphology, exposed facets, and surface coating. Also, iron oxide nanoparticles are commonly known to possess a magnetite (Fe_3O_4) or maghemite (Fe_2O_3) crystal structure, which are quite difficult to differentiate only on the basis of XRD measurements. But a careful observation of the previous reports reveals that they also lack detailed characterization to differentiate between a magnetite (Fe_3O_4) and maghemite (Fe_2O_3) crystal structure of the iron oxide NPs.

In this chapter, we show the synthesis of highly mono-disperse and crystalline iron oxide nanocubes for simultaneous contrast enhancement in both T_1- and T_2-weighted MRI. We also performed a detailed characterization to confirm the magnetite structure of the iron oxide nanocubes. These nanocubes were successfully demonstrated as DMCAs in phantom experiments and in vivo MRI. Also, these nanocubes are small in size (9.7 nm) and can be used in most parts of the human body.[194], [211] These nanocubes are unique in that, being smaller in size, they offer simultaneous T_1 and T_2 contrast enhancement in MRI while being safer for the body. To the best of our knowledge, this is the first report of dual contrast enhancement in T_1- and T_2-weighted MR images using magnetite nanocubes.

5.2 Experimental Methodology

5.2.1 Materials

Ammonia (28 wt% in water), poly(5)oxyethylene-4-nonyl-phenyl-ether (Igepal Co 520), tetraethyl orthosilicate (TEOS, 99%), oleic acid (tech 90%), 1-octadecene (tech 90%) and iron (III) chloride hexahydrate (99.99%) were purchased from Sigma-Aldrich. Sodium hydroxide, ethanol, hexane, cyclohexane and other reagents were purchased from Alfa Aesar. All chemicals were used as received without further purification.

5.2.2 Synthesis of sodium oleate

Sodium oleate was prepared by adding sodium hydroxide (0.71 g, 17.6 mmol) to oleic acid (5.56 mL, 17.6 mmol) dissolved in ethanol (50 mL). The reaction mixture was stirred overnight at room temperature. Removal of the solvent under vacuum yielded the product as a white soap.

5.2.3 Synthesis of iron–oleate complex

In a typical procedure, iron chloride ($FeCl_2 \cdot 6H_2O$ ~ 0.9 g, 5 mmol) and sodium oleate (4.56 g, 15 mmol) were mixed in a round bottom flask with distilled water (60 mL), ethanol (25 mL) and hexane (25 mL) to generate the Fe-oleate complex. The reaction system was allowed to perform at 90 °C for 4 h before cooling to room temperature. When the reaction was complete, the upper organic layer containing the Fe-oleate complex was washed two times with distilled water in a separatory funnel. After washing, hexane was evaporated off, resulting in the Fe-oleate complex in a waxy form.

5.2.4 Synthesis of magnetite nanocubes

Iron oleate (0.5 g), oleic acid (0.1 mL) and 1-octadecene (10 mL) were mixed in a three neck bottle flask and degassed under argon for 30 min at 70 °C. The reaction mixture was heated to 320 °C with a constant heating rate of 5.5 °C

min^{-1}, and then maintained at that temperature for 30 minutes. When the reaction temperature reached 320 °C, a severe reaction occurred and the initial transparent solution became turbid and brownish black. The resulting solution containing the nanocrystals was then cooled to room temperature, and the synthesized nanocrystals were precipitated using iso-propanol and redispersed in hexane for further use.

5.2.5 Silica coating on magnetite nanocubes

For the reverse microemulsion synthesis, IgePAL CO-520 (1.3 mL) was dispersed in cyclohexane (10 mL) and stirred for 15 min (500 rpm) to form a stable solution. Subsequently, a dispersion of nanocubes (0.5-1 nmol) in cyclohexane (1 mL) was added, followed by TEOS (80 µL) and ammonia (150 µL). Between the additions, the reaction mixture was stirred for 15 min (500 rpm). Once ammonia was added, the mixture was stirred for 2 days. Finally, the particles were purified by adding 25 mL of ethanol to the reaction mixture and the whole mixture centrifuged for 20 min at 9500 rpm. After the removal of the supernatant, 25 mL of ethanol was added, and the silica particles were sedimented again by centrifugation at 9500 rpm for 20 min. This was repeated once more for 20 min, after which the particles were redispersed in 5 mL double distilled water and stored at 4 °C.

5.2.6 Characterization of the magnetite nanocubes

TEM, HR-TEM images and the SAED pattern of nanocubes were obtained using a high resolution transmission electron microscope (TEM-Tecnai G2 F30) operating at 300 kV. UV-Vis absorption spectra were recorded using a UV-Vis spectrophotometer (Varian -Cary 100). FT-IR spectra was recorded by using an FT-IR spectrometer (Bruker-Vertex 70). Magnetic measurements (M-H and M-T curves) were recorded on a Quantum Design MPMS-XL-7 system. MR phantom experiments were performed at room temperature on a 3T Siemens TrioTim MR scanner. Various concentrations (3 to 60 µM) of magnetite nanoparticles were prepared for MRI phantom study. T_1-weighted and T_2-weighted phantom MR images of magnetite nanoparticles were acquired using a

spin echo (SE) sequence under the following parameters: TR/TE=1000/12 ms (T_1), TR/TE=10000/330 ms (T_2), (slice thickness=3 mm, flip angle=90°, acquisition matrix=384 pixels×384 pixels, FoV=120×120 mm^2).

5.2.7 *In vivo* MR imaging

Animal experiments were performed using a Sprague Dawley (200-250 g) rat according to a protocol approved by the animal ethics committee of Bilkent University, Turkey. MRI experiments were performed at room temperature on a 3T Siemens TrioTim MR scanner. Silica coated magnetite nanocubes with the dosage of 1 $mgkg^{-1}$ were injected into a rat through its tail vein and coronal images of the kidneys were taken before and after the injection of magnetite nanocubes. T_1-Weighted and T_2-weighted *in vivo* rat MR images were acquired using a spin echo (SE) sequence under the following parameters: TR/TE=550/11 ms (T_1), TR/TE=4420/94 ms (T_2) (slice thickness=2 mm, flip angle=90°, acquisition matrix=384 pixels×384 pixels, FoV=90×90 mm^2).

5.2.8 Cytotoxicity studies

The *in vitro* cytotoxicity of iron oxides nanocubes was investigated using a L929 mouse cell line. Silica coated iron oxides were added with the concentrations of 0, 25, 100 and 200 µg Fe mL^{-1} and their toxic responses were evaluated by the Alamar Blue Assay after 24 h. To determine the viability, 2×10^3 L929 cells were seeded into a 96-well plate (n = 3) and silica coated cubic iron oxides were added in different concentrations in ddH_2O. For the positive control, the cells were grown without exposure to the nanoparticle solution. In order to understand the fatal effect of less medium on the cells, we added phosphate buffer saline (PBS) with the same amount of ddH_2O as the negative control group for each concentration. Cells were cultured in Dulbecco's modified Eagle's medium (DMEM) containing 10% fetal bovine serum (FBS) at 37 °C and 5% CO_2 for 24 h. Subsequently, the cells were incubated in Alamar Blue solution (10% in DMEM-high glucose colorless medium) at 37 °C for 1 h. After the desired incubation time, the supernatant (200 µL) was transferred into a 96-well plate, and the absorbances at 570 and 595 nm were measured. A calibration curve was

constructed using known concentrations of cells (L929) to relate the cell numbers to the dye reduction (%).

5.3 Results and Discussion

Magnetite nanocubes were synthesized using thermal decomposition of the iron-oleate complex using a modified receipe.[105] We observed that the shape and size of the iron oxide NPs can be controlled by varying the molar ratio of iron-oleate to oleic acid and the heating rate. In Ref.,[105] 12 nm sized spherical magnetite NPs were synthesized with the ratio of iron-oleate:oleic acid as 2:1, with a heating rate of 3.3 °C min^{-1}. In our case, cubic shaped magnetite NPs were obtained with increased oleic acid amounts, i.e., equal molar ratio of iron-oleate and oleic acid, with a heating rate of 5.5 °C min^{-1}. The small but critical reduction in the growth rate by the additional oleic acid appears to promote the formation of iron oxide NPs with a nonspherical, faceted shape.

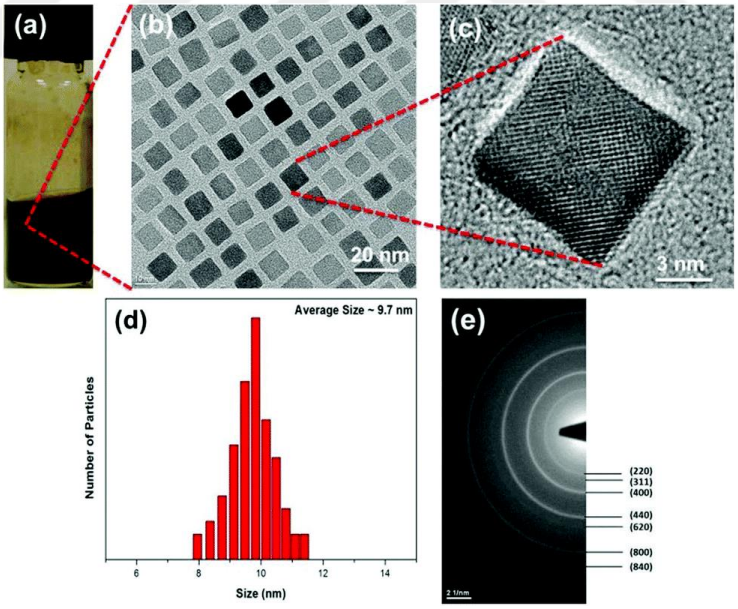

Figure 5.1. (a) Magnetite nanocubes dispersed in hexane. (b) TEM, (c) HR-TEM, (d) PSD and (e) SAED pattern of the as-synthesized magnetite nanocubes. Reprinted with permission from Ref. [187] Copyright The Royal Society of Chemistry 2015.

Figure 5.1a shows the magnetite nanocubes dispersed in hexane and Figure 5.1b shows TEM (transmission electron microscopy) images of monodisperse magnetite nanocubes with an average size of 9.7±0.5 nm. The particle size distribution (PSD) of the nano-cubes obtained using ImageJ software is shown in Figure 5.1d. XRD spectra of as-synthesized iron oxide nanocubes are presented in the Figure 5.2.

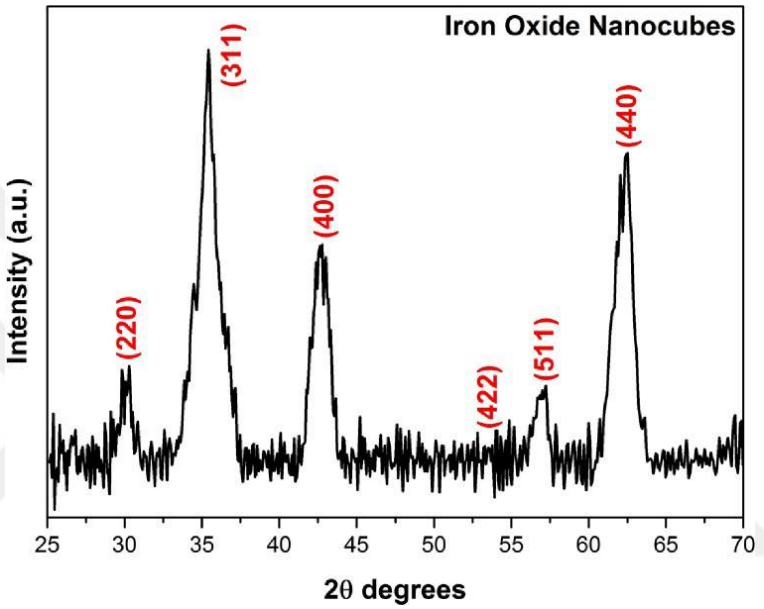

Figure 5.2. XRD spectra of as-synthesized iron oxide nanocubes. Reproduced with permission from Ref. [187] Copyright The Royal Society of Chemistry 2015.

From the XRD data, it is found that the reflections are closer to the magnetite structure of the iron oxide NPs (Table 5.1). To further confirm the structure of these nanocubes, we have also recorded, SAED, FT-IR and absorption spectra. The magnetite structures of the iron oxide nanocubes were confirmed by selected area electron diffraction (SAED) pattern,[212] Fourier transformed infrared spectra (FT-IR)[105], [213] and optical absorption measurements.[213] We carried out SAED (Figure 5.1e) of these nanocubes and found that the rings can be assigned to the spinel structure of magnetite (JCPDS#19-0629). The 220 (d=2.9683 Å) and 400 (d=2.0956 Å) phases in the SAED pattern are exclusive to the structure of magnetite.[212] The highly crystalline nature of these nanocubes is demonstrated by the high-resolution (HR) TEM images as shown

in Figure 5.1c. HR-TEM also confirms that the spacing between the planes (d~0.295 nm) is close to the magnetite structure of iron oxide nanocubes.

Table 5.1. XRD data comparison of the experimental data with the standard magnetite and maghemite JCPDS data.

(hkl) Planes	Experimental Data d (Å)	JCPDS 19-0629 Magnetite Fe_3O_4 d (Å)	JCPDS 39-1346 Maghemite Fe_2O_3 d (Å)
(220)	2.96406	2.9670	2.9530
(311)	2.53165	2.5320	2.5177
(400)	2.11472	2.0993	2.0886
(422)	1.71430	1.7146	1.7045
(511)	1.61598	1.6158	1.6073
(440)	1.48642	1.4845	1.4758

To further confirm the crystal structure of the as-synthesized iron oxide nanocubes, we performed absorption and FT-IR measurements. The nanocubes are easily dispersed in hexane to form transparent colloids, with a characteristic vivid color corresponding to the color of the bulk material. The absorption data are generally consistent with the characteristic color of the sample and are, therefore, considered as a reliable way of differentiating magnetite and maghemite structures of iron oxide. For Fe_3O_4 nanocubes, the absorption spectrum exhibits a full absorption band in the visible region 400-700 nm, which corresponds to the black color of the dispersion.[213] For α-Fe_2O_3, the strongest absorption peak appears at 400-450 nm and corresponds to the red color. In our case, the absorption spectrum exhibits a full absorption band in the visible area (Figure 5.3a) along with the black color of the dispersion (Figure 5.1a). Therefore, from the absorption data, it is clear that in our case the nanocubes possess a magnetite structure.

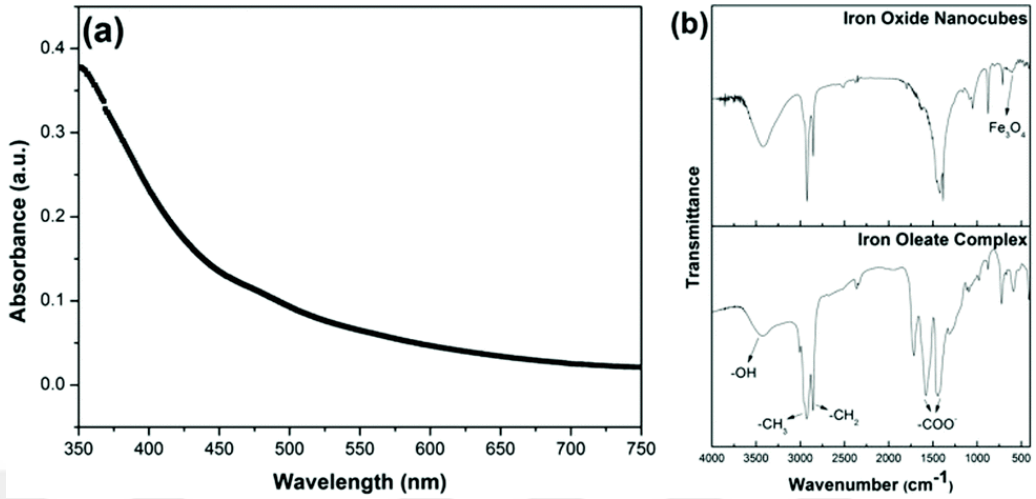

Figure 5.3. (a) Absorption spectra of the as-synthesized magnetite nanocubes. (b) FT-IR spectra of the as-synthesized magnetite nanocubes and the iron–oleate complex. Reproduced with permission from Ref. [187] Copyright The Royal Society of Chemistry 2015.

FT-IR spectra of the iron-oleate complex and iron oxide nanocubes are presented in Figure 5.3b. FT-IR was used to identify the functional groups present in the nanocubes. The wide band at 3130-3630 cm^{-1} is assigned to O-H vibrations. The sharp bands at 2923 and 2853 cm^{-1} are assigned to the asymmetric methyl stretching and the asymmetric and symmetric methylene stretching modes, respectively. The sharpness of the bands is attributed to the well-ordered, long hydrocarbon chain of oleic acid. The characteristic bands at 1560 and 1443 cm^{-1} can be attributed to the asymmetric and symmetric COO^- stretches, respectively, indicating that the oleic acidchain is attached in a bidentate fashion, with both oxygens symmetrically coordinated to the surface.[214] Based on the FT-IR spectra, oleic acid is thought to coat the surface of the nano-cubes. TEM results, in conjunction with FT-IR data, suggest that, in our case we have a core-shell structure, with an iron oxide core and an oleate shell (~1.6 nm). This is also confirmed by the uniform spacing between the nanocubes (Figure 5.1b). FT-IR is also used as a tool to distinguish magnetite and maghemite structures from each other through their distinct lattice absorption peaks.[199] The lattice absorption peaks of the iron oxide nanocubes centered at ~595 cm^{-1} (Figure 5.3b) indicate that the nanocubes are most

probably magnetite.[215], [216] Therefore, on the basis of the SAED pattern, optical absorption data and FT-IR measurements, we confirm that these iron oxide nanocubes possess a magnetite structure.

We also studied the magnetic properties of these nano-cubes using a Quantum Design MPMS-XL-7 system. The magnetization dependence on the magnetic field (M-H curve) of the magnetite nanocubes was measured at body temperature (310 K). We performed the measurements at body temperature because we wanted to use these materials in humans as MRI contrast agents. M-H curves as shown in Figure 5.4a indicate that the saturated magnetization (M_s) of the as-synthesized magnetite nanocubes (~18 emu g^{-1}) is much lower than that of magnetite NPs with a similar size (~65 emu g^{-1}) measured at room temperature.[217] Moreover, the continuous growth of magnetization along with the applied magnetic field for magnetite nano- cubes is probably due to the enhanced spin canting effect on the surface layer of these nanocubes because of the size and shape,[218] which may be responsible for the partially paramagnetic properties of these nanocubes. The characteristic M-H curves of these nanocubes are similar to those of the high-spin paramagnetic rare-earth materials and superparamagnetic nanoparticles,[219] suggesting that these nanocubes exhibit both superparamagnetic and paramagnetic behaviors. The presence of mixed magnetic phases is further confirmed by fitting the M-H curves with the following relation:

$$M(T) = M_s \left[\coth\left(\frac{\mu H}{k_B T}\right) - \left(\frac{k_B T}{\mu H}\right)\right] + \chi H \qquad (5.1)$$

where M(T) is the magnetization of the nanocubes at temperature T, M_s represents the saturation magnetization of the nanocubes, μ is the magnetic moment of the nanocubes, χ is the susceptibility of the nanocubes and k_B is the Boltzmann constant. The first term in Equation (5.1) is the superparamagnetic contribution and the second term is the paramagnetic contribution to the total magnetic moment of the nanocubes. The M-H fit obtained by using Equation (5.1) is shown in red color in Figure 5.4a. Equation (5.1) is in excellent agreement with the experimental data, substantiating the simultaneous presence of two magnetic phases in the nanocubes. Therefore, we conclude that these nanocubes

possess superparamagnetic and paramagnetic phases simultaneously, which result in simultaneous contrast enhancement in T_1 and T_2-weighted MR images similar to GdIO NPs.[19]

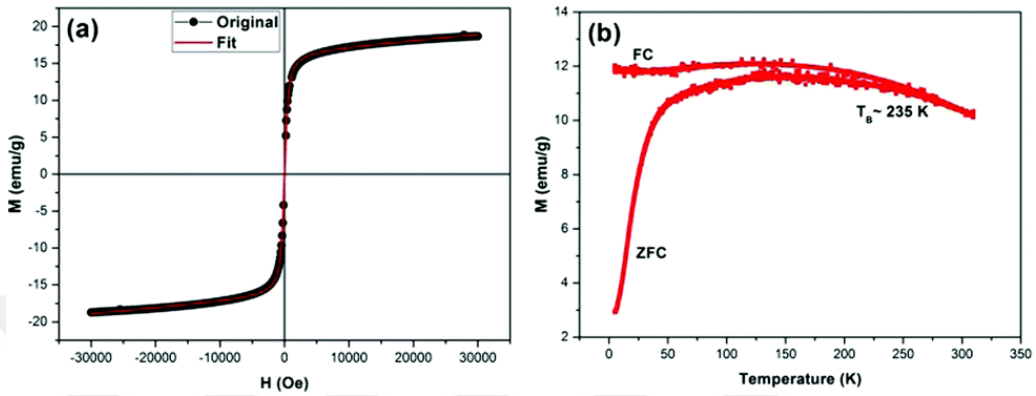

Figure 5.4. Magnetic properties; (a) *M–H* and (b) *M–T* curve of the as-synthesized magnetite nanocubes. Reprinted with permission from Ref. [187] Copyright The Royal Society of Chemistry 2015.

We also studied the magnetization (M) dependence (zero field cooled-ZFC and field cooled-FC curves) on temperature (T) of the as-synthesized magnetite nanocubes. The ZFC and FC curves, which coincide initially, but start to separate and follow different trends as the temperature is decreased from 310 to 5 K. In the FC mode at the field level of H=100 Oe, the magnetization increases slightly and then levels off (Figure 5.4b), whereas the ZFC magnetization reaches a maximum followed by a steady decrease to a value approaching zero in the low temperature region. The shape of the FC curves is the result of the presence of dipole-dipole interactions between the oleate-capped magnetite nanocubes.[220] Moreover, the variation of the magnetization in the ZFC and FC modes indicates a dominant superparamagnetic behavior for the magnetite nanocubes. The value of the blocking temperature for the nanocubes is estimated to be 235 K, obtained from the Stoner-Wohlfarth relationship:

$$T_B = \frac{K}{25k_B} * V \qquad (5.2)$$

where T_B is the blocking temperature, K is the anisotropy constant, V is the volume of the nanocubes, and k_B is the Boltzmann constant. Similar values of the blocking temperature for iron oxide NPs are reported by Caruntu *et al.*[217]

Magnetite nanocubes were made water soluble for MRI applications by silica coating using a recipe reported elsewhere.[221] The encapsulated nanoparticles showed excellent colloidal stability in water. The hydrodynamic diameter of the silica coated nanocubes in deionized (DI) water, measured by dynamic light scattering (DLS), was 27.8 nm (Figure 5.5). DLS measurements reveal that the nanocubes are monodisperse with no aggregation. The hydrodynamic diameter value is less than 30 nm. Therefore, these nanocubes come in the category of ultra-small iron oxide nanocubes (USIONs). Hydrodynamic diameter is an important parameter for the use of contrast agents in the human body. Our nanocube hydrodynamic size lies between 43 nm[207] (maximum r_2 relaxivity ~761 $mM^{-1}s^{-1}$ reported) and 15 nm[208] sized nanoparticles (r_1 relaxivity ~4.78 $mM^{-1}s^{-1}$). Our coated nanocube size (~27.8 nm) is close to the median of these two values. Therefore, we believe that because of the size and shape (enhanced spin-canting effect) of our nanocubes, they have the ability to enhance the contrast in both T_1-and T_2-weighted MRI.

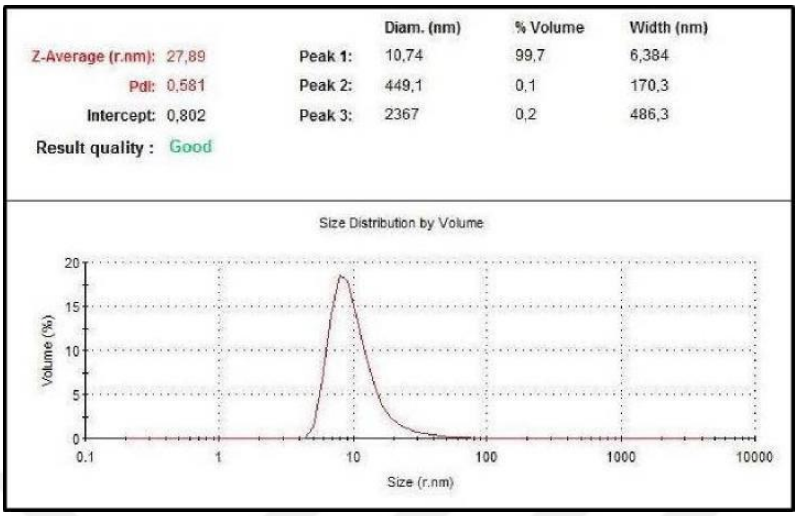

Figure 5.5. DLS Particle size measurements of the magnetite nanocubes dispersed in water. Z-average (27.8 nm) obtained from DLS is considered as a robust parameter for calculating the size. Reproduced with permission from Ref. [187] Copyright The Royal Society of Chemistry 2015.

The utility of the water-soluble magnetite nanocubes as DMCAs for MR phantom studies was investigated in solution. Nanocubes were studied by using a 3T Siemens MR scanner to observe the contrast enhancement in both T_1- and T_2-weighted MR images. Figure 5.6a shows the T_1-weighted MR images of silica capped magnetite nanocubes at different concentrations. We can clearly observe the increase in the image contrast (bright) with the increase in nanocubes concentration.

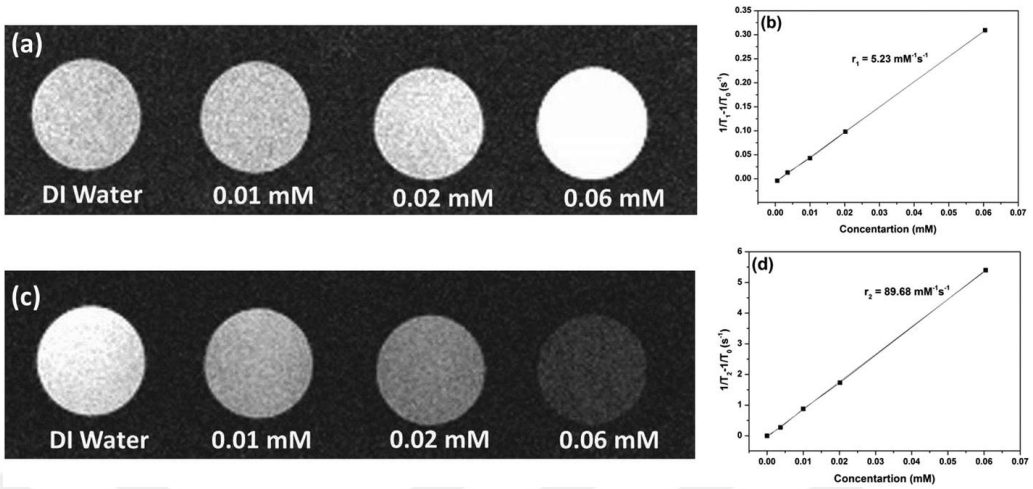

Figure 5.6. (a) T_1-weighted and (c) T_2-weighted MR phantom images of the as-synthesized magnetite nanocubes. (b) T_1 and (d) T_2 relaxivity plots of the as-synthesized magnetite nanocubes obtained at 3T @25 °C. Reprinted with permission from Ref. [187] Copyright The Royal Society of Chemistry 2015.

To examine the feasibility of using magnetite nanocubes as simultaneous T_1 and T_2 MRI contrast agents, the relaxation time was measured. The relaxation time $T_{1,2}$ was measured at 3T @25 °C using a spin echo sequence. The longitudinal (r_1) and transverse (r_2) relaxivities were determined from the following relation:

$$r_{1,2}[Fe_3O_4] = \frac{1}{T_{1,2}} - \frac{1}{T_0} \tag{5.3}$$

where T_0 and $T_{1,2}$ are the longitudinal and transverse relaxation times of DI water and the samples with increasing nano-cube concentration, respectively.[222] From the slope of ($1/T_1$-$1/T_0$) versus nanocubes concentration (Figure 5.6b), we obtain the longitudinal relaxivity (r_1) as 5.23 $mM^{-1}s^{-1}$. The high r_1 relaxivity of the magnetite nanocubes can be attributed to the large number of Fe^{3+} ions with 5 unpaired electrons on the surface of the nanocubes. This value is higher than the value reported for 3 nm sized spherical iron oxide nanoparticles,[208] which most probably resulted from the shape of our nanocubes as suggested by Zhen *et al.*[209] Recently, Zhou *et al.*[210] reported T_1 contrast enhancement in Fe_3O_4 nanoplates with (111) exposed surfaces. In our case too, there may be some contribution to the T_1 contrast from the exposed surfaces of the magnetite nanocubes.

Figure 5.6c shows the T_2-weighted MR images of silica capped magnetite nanocubes at different concentrations. Here, we can clearly observe the decrease in the image contrast (dark) with the increasing nanocubes concentration.The transversal relaxivity (r_2) value of nanocubes obtained from the slope of ($1/T_2$-$1/T_0$) versus nanocubes concentration (Figure 5.6d) is 89.68 $mM^{-1}s^{-1}$.

Magnetite nanocubes exhibit low T_2 relaxivity as compared to the larger sized particles because the low magnetic moment induces weak magnetic inhomogeneity around the particles.[207]

Thus, with increased concentrations of magnetite nano-cubes, we observed reduced signals in T_2-weighted MR images and increased signal in T_1-weighted MR images, indicating that magnetite nanocubes can act as both negative and positive contrast agents simultaneously. Iron oxide NPs are well known for their excellent T_2 contrast enhancement effect with no obvious T_1 contrast effect. By decreasing the size of the magnetic NPs, they are also reported as potential T_1 contrast agents.[208], [223]

By fine-tuning the shape of the iron oxide nanoparticles into cubes and making their size ultra-small, here we aim at achieving simultaneous enhancement in both positive and negative MR contrast images. In our case, we conclude that our nanocubes shape and dimension combinedly result in the simultaneous contrast enhancement in both T_1- and T_2-weighted MRI, which we do not observe otherwise individually.

The *in vitro* cytotoxicity of magnetite nanocubes was investigated using the L929 mouse cell line with the concentrations of 0, 25, 100 and 200 µg Fe mL^{-1} in ddH_2O. No appreciable toxicity was observed even at very high concentrations of 100 µg Fe mL^{-1} (Figure 5.7), which is consistent with the recent report by Wortmann *et al.*[224] On the other hand, further addition of cubic iron oxide decreased the viability of the L929 cell. The result of cell assays confirmed that the silica coated iron oxide nanocubes are not significantly cytotoxic, up to high concentrations of 100 µg Fe mL^{-1}.

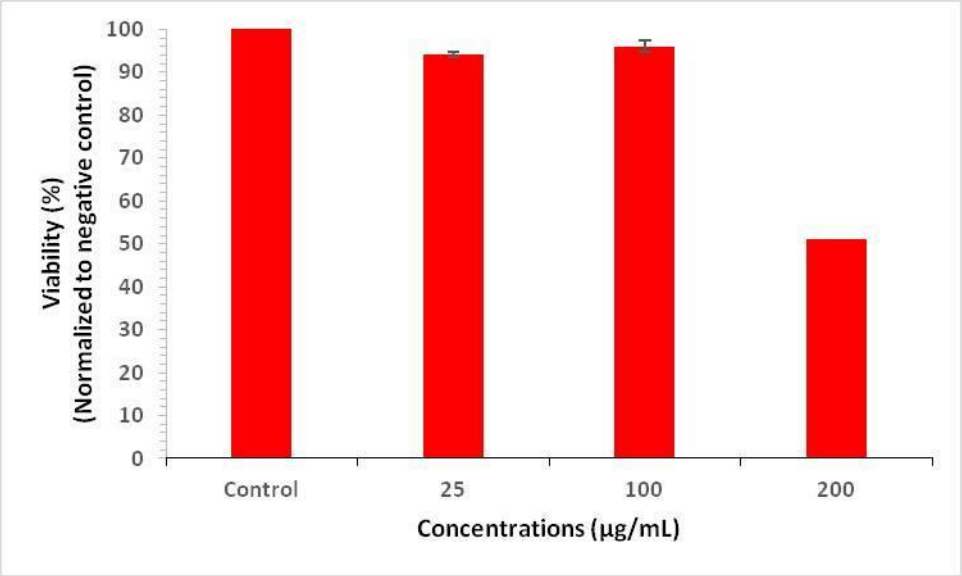

Figure 5.7. Cytotoxicity data for the silica coated iron oxide nanocubes and the control. Reproduced with permission from Ref. [187] Copyright The Royal Society of Chemistry 2015.

We further studied the *in vivo* MR imaging of the rat kidneys using these nanocubes. For *in vivo* MR imaging, T_1 and T_2 dual-mode abdominal images before and after the injection were obtained by using a 3T MR scanner at room temperature. Silica coated magnetite nanocubes with a dosage of 1 mg kg^{-1} were injected into the rat through its tail vein and the coronal images of the kidneys were taken before injection, immediately after injection, and after 30 and 60 min of injection (Figure 5.8). Since the kidney is an important member of the urinary system and one of its functions is a filtration of waste products from the body, we focused on the kidneys in the MR imaging. With the post injection time, the blood vessels going into kidneys gradually turned brighter and darker in T_1 and T_2 coronal planes, respectively. Color images of the kidney areshown in the insets of Figure 5.8 for clarity. These results demonstrate that although our silica coated cubic nanoparticles have a hydrodynamic diameter (HD) of 27.8 nm, they can be observed in the kidneys where the renal cut-off is 5-6 nm. This may be due to the coating material, "silica". There are several reports[211], [225] on the renal clearance of silica coated nano-particles, which revealed intact and larger particles in the urine; however, the exact excretion process remained unclear. In

order to understand the clearance mechanism involving silica, Lu *et al.*[226] investigated the biodistribution of silica nano-particles with diameters of *ca.* 100-130 nm. They observed a rapid excretion of almost all of the nanoparticles from the body through urine and feces. Similar results were also observed by He *et al.*[132] revealing that the silica nanoparticles of *ca.* 45 nm accumulated mainly in the liver, kidney, and urinary bladder a few hours after intravenous injection and consequently silica nanoparticles are safely removed through the renal route. All of these previous studies clearly show that very large nanoparticles can be efficiently removed from the body *via* renal excretion. In the light of these studies, we can attribute the excretion of our nanoparticles to the silica coating which may help particles to escape RES recognition by possibly limiting the opsonization of nanoparticles[131] and guiding them to renal clearance. Furthermore, intravenous injection might also take a role in the rapid renal excretion of our nanoparticles as reported by He *et al.*[132] In addition, similar to Ref.,[226] it is also possible that our nanoparticles degrade quickly in the bloodstream and the smaller particles may then prefer renal clearance. However, a more detailed analysis on the clearance mechanism of the silica coated iron oxide nanoparticles larger than 6 nm should be investigated as a subject of another study for a better and deeper understanding.

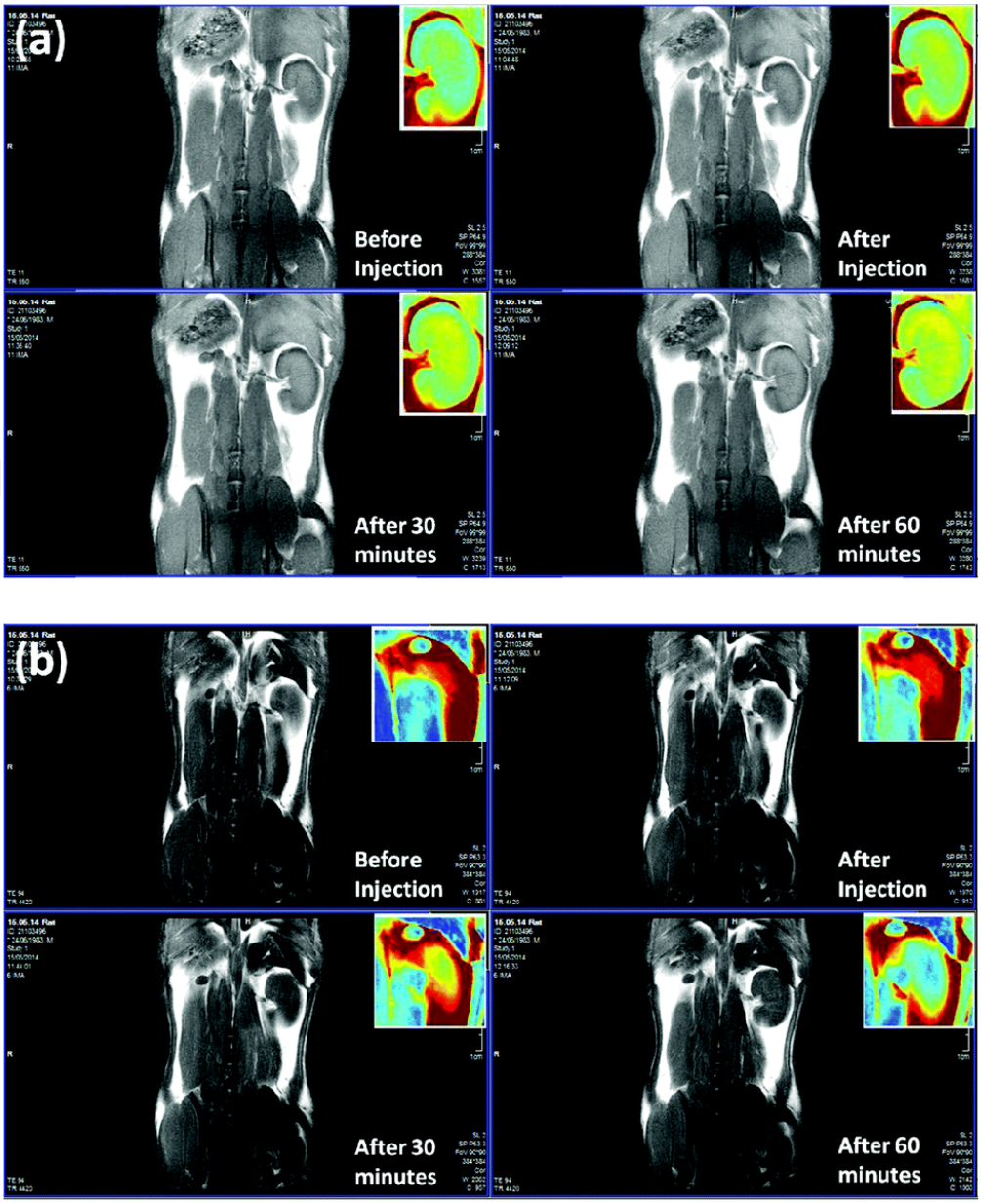

Figure 5.8. (a) T_1- and (b) T_2-weighted *in vivo* MR images obtained before and after the nanocubes injection into the rat, at 3T @25 °C. In the inset, the kidney images in color are shown for the clear enhancement in the contrast. Reproduced with permission from Ref. [187] Copyright The Royal Society of Chemistry 2015.

In summary, our experiments have demonstrated that these nanocubes are suitable as a contrast agent for MRI owing to their strong MR contrast enhancement in both T_1- and T_2-weighted imaging. Because of their dual-mode

contrast feature and high biocompatibility, they allow access to comprehensive information with higher accuracy in medical diagnosis.

5.4 Summary

In this chapter, we show the colloidal synthesis of highly crystalline, monodisperse and low-magnetization magnetite nanocubes that achieve simultaneously enhanced contrast in T_1- and T_2-weighted MR images. The dual-mode MR contrast enhancement capabilities of these nanocubes are a direct result of the simultaneous presence of superparamagnetic and paramagnetic phases as confirmed by the magnetic measurements. Also, these nanocubes are small in size (~9.7 nm) and almost harmless for use in the human body. These nanocubes while being non-toxic and bio-compatible, hold great promise as DMCAs for better diagnosis of patients using MRI.

Chapter 6
Dynamics of T_1 and T_2 Relaxivities in Spherical and Cubic Colloidal Iron Oxide Nanoparticles with Different Sizes

In this part of the thesis, we will present our study on the investigation of longitudinal (r_1) and transverse (r_2) relaxivities of colloidal iron oxide nanoparticles depending on their sizes and shapes. Here, we systematically studied the colloidal synthesis parameters to control size and shape of the IO NPs and employed both cubic and spherical iron oxide nanoparticles in three different sizes. We found out that these iron oxide nanoparticles have magnetite crystal structure. Besides, magnetic characterizations revealed that cubic nanoparticles have better magnetic features including saturation magnetization, r_1 relaxivity and r_2 relaxivity compared to their spherical counterparts. Finally, we observed that both cubic and spherical IO NPs possess paramagnetic phase additionally to their superparamagnetic phase, which are directly correlated with the longitudinal (r_1) and transverse (r_2) relaxivities.

This chapter of the thesis is mainly based on Z. Soran-Erdem, V. K. Sharma, A. Alipour, P. L. Hernandez-Martinez, and H. V. Demir, "Direct Correlation of T_1 and T_2 Relaxivities in Highly Monodispersed Iron Oxide Nanoparticles," (2016) (*submitted*)

6.1 Motivation

Superparamagnetic iron oxide nanoparticles (SPIONs) have stepped forward as promising T_2 contrast agents in magnetic resonance imaging (MRI) by shortening mainly the spin-spin relaxation and thereby resulting in darker images. They are favorable materials, particularly for biomedical applications, thanks to their air stability and degradation without toxic by-products. However, the difficulty to

distinguish the darker area originating from endogenous artifacts and the contrast agents makes the accurate diagnosis very challenging in T_2-weighted imaging,[227], [228] while T_1-weighted imaging provides an excellent resolution between tissues owing to its high signal intensity. Unfortunately, the toxicity of commonly used Gd- and Mn-based T_1 contrast agents significantly limits their applicability.[194], [229] Therefore, combining the T_1- and T_2-weighted MRI capabilities in a single nontoxic material is of critical importance, which may significantly improve the detection accuracy and applicability in clinical diagnosis. One of the approaches to achieve T_1-weighted contrast in addition to T_2 contrast with spherical SPIONs is to decrease the size of the nanoparticles (<5 nm), which also results in the decrease of the magnetic moment.[208], [227], [230] Alternatively, doping the SPIONs with paramagnetic metal ions such as manganese[200] and gadolinium was proposed.[231] Dual-modal effect can also be observed by tuning the shape of the SPIONs without doping. For example, Sharma *et al.* employed highly crystalline and monodisperse iron oxide nanocubes with the size of ~9.7 nm and demonstrated simultaneously enhanced contrast in T_1- and T_2-weighted MR images with the undoped cube SPIONs for the first time.[187]

The magnetic properties of SPIONs strongly depend on their sizes and shapes. Therefore, it is very crucial to control their morphology.[232] However, iron oxide nanoparticles have a rich phase diagram with a variety of oxidation states, which makes it more complicated to control the synthesis of SPIONs with a uniform shape, size, and structure.[233] Additionally, the intrinsic agglomerating features of magnetic nanoparticles is an important challenge for the monodisperse synthesis of SPIONs.[213] To date, various mechano-chemical (mechanical milling technique, pyrolysis and electrodeposition) and chemical procedures (co-precipitation, emulsion, hydrolysis of iron salt and decomposition of organic iron precursor) have been used to control the shape and size of the iron oxide nanoparticles.[96], [105], [187] Among them, high-temperature decomposition of iron-oleate (Fe-oleate) has been found to be one of the best approaches to produce magnetic iron oxide nanoparticles for biomedical applications. In this method, synthesized iron oxide nanoparticles exhibit monodispersity in size and shape together with the successful control of crystal structure owing to high

temperature.[234] Furthermore, ultralarge-scale synthesis of iron oxide nanoparticles is also possible with this method.[105] Depending on the reaction conditions, different sizes, shapes and crystal structures can be obtained in Fe-oleate decomposition method. Liang *et al.*[213] reported that alkalinity of the reaction and polarity of the solvent in the synthesis are important parameters affecting the phase formation and size of the nanoparticles (NPs), respectively. They demonstrated that increased alkalinity favors the formation of Fe_3O_4 iron oxide NPs and the size of the nanoparticles increase with increasing solvent polarity. The influence of Fe-oleate complex prepared in different conditions is discussed by Bronstein *et al.*[235] To enable the formation of cubic SPIONs, using additional sodium-oleate (Na-oleate) complex is a well-known and mostly preferred approach in most synthesis procedures reported so far.[236], [237] Although the parameters that play a role on the shape and size are discussed in these previous studies, the underlying mechanism of cubic particle formation is not clear yet. Moreover, while the increased T_2-weighted imaging of iron oxide nanocubes were reported,[207] the literature lacks a systematic study of their T_1-weighted mechanism.

In this chapter, we address these long-pending problems by systematically studying the parameters that govern the size and shape of the SPIONs and correlating them to their magnetic properties. First, we successfully synthesized these iron oxide NPs in ultralarge scales by carefully controlling the synthesis conditions. Subsequently, we structurally and magnetically characterized cube and sphere SPIONs having three different sizes. In addition to T_2-relaxation dynamics of SPIONs, we also systematically investigated the size and shape dependence of their T_1-relaxation times for the first time in order to evaluate the potential application of these nanoparticles for dual-modal (T_1- and T_2-weighted) MRI.

6.2 Experimental Methodology

6.2.1 Materials

Oleic acid (tech 90%), 1-octadecene (tech 90%) and iron (III) chloride hexahydrate (99.99%) were purchased from Sigma-Aldrich. Sodium hydroxide, ethanol, hexane, 2-propanol and other reagents were purchased from Merck. All chemicals were used as received without further purification.

6.2.2 Synthesis of sodium-oleate (Na-oleate)

Sodium-oleate precursor was prepared by adding 17.6 mmol sodium hydroxide (0.71 g) to 17.6 mmol oleic acid (5.56 mL) dissolved in 50 mL ethanol. After stirring the mixture overnight at room temperature, excess solvent was removed under vacuum. This dry product was used as a precursor of iron-oleate synthesis.

6.2.2.1 Synthesis of iron-oleate (Fe-oleate) precursor

In order to synthesize the Fe-oleate precursor, 15 mmol (4.56 g) of freshly synthesized Na-oleate and 5 mmol of iron chloride ($FeCl_3.6H_2O$~0.9 g) were mixed in a round bottom flask together with 60 mL of distilled water, 25 mL of ethanol and 25 mL of hexane. The mixture was stirred at 80 °C for 4 h and then cooled down to room temperature. Subsequently, the mixture was cleaned by removing the lower inorganic part in a separatory funnel. Remaining organic layer was washed eight times with water, and hexane was evaporated under vacuum. After three days, Fe-oleate complex was obtained in a waxy form to be used in the iron oxide syntheses.

6.2.2.2 Synthesis of cubic and spherical superparamagnetic iron oxide nanoparticles

For the synthesis of SPIONs, we used a modified procedure reported previously.[105], [187] In a typical procedure, 25 mL (~20 g) of 1-octadecene (ODE) solution containing oleic acid and freshly synthesized Fe-oleate were stirred in a three neck bottle flask and degassed under vacuum at 70 °C for 2 h.

Then, the temperature of the reaction was increased to 320 °C at a constant heating rate of 3.3 °C min^{-1}, 4.2 °C min^{-1} or 5.5 °C min^{-1} under argon flow and kept at that temperature for 30 min unless otherwise stated. Syntheses of cubic iron oxide nanoparticles were performed without addition of Na-oleate or other chemicals different than the literature.[236], [237] To understand the effect of oleic acid and Fe-oleate on the size and shape change, varying amounts of these chemicals were used. Briefly, 0.8 mmol (0.25 mL), 1.6 mmol (0.50 mL), 1.9 mmol (0.60 mL) and 2.4 mmol (0.75 mL) of oleic acid were used. 2.1 mmol (1.88 g) Fe-oleate was used in all of these syntheses. Afterwards, to study the effect of Fe-oleate amount with respect to oleic acid concentration, two different syntheses were performed using 0.8 and 2.4 mmol oleic acid. In the synthesis involving 0.8 mmol of oleic acid, 2.1 and 2.4 mmol of Fe-oleate were used. On the other hand, we used 1.4, 1.7 and 2.1 mmol of Fe-oleate when we employed 2.4 mmol oleic acid. In order to investigate the effect of growth time on the size, the reaction duration was changed from 0.5 to 5.0 h. Following the growth of nanocrystals, the solution was cooled down to room temperature. For cleaning, 2-propanol was added onto the synthesis solution and the nanocrystals were precipitated at 4500 rpm for 20 min using centrifugation. After removing the supernatant, the samples were washed with acetone for three times. Then, SPIONs were dispersed in 16 mL of hexane and filtered using 0.2 µm Millipore filter.

6.2.3 Structural characterization of the nanocubes and nanopsheres

The effect of various parameters (*e.g.* oleic acid, Fe-oleate, rate of temperature increase) on the size and shape were investigated by a high-resolution transmission electron microscope (TEM) (Tecnai G2 F30). Three sets of cubic and sphere iron oxide nanoparticles having 7.0, 11.0, and 13.5 nm diameter were characterized structurally and magnetically. Hydrodynamic size and homogeneity of these cubic and spherical SPIONs were examined using Malvern Nano-ZS Zetasizer dynamic light scattering (DLS). Furthermore, surface chemistry of the SPIONs were investigated using a Bruker-Vertex 70 Fourier transform infrared (FT-IR) spectrometer. FT-IR samples were prepared by forming drop-casted iron oxide film on the potassium bromide (KBr) pellet.

Absorption spectra of the samples were acquired by Cary-100 UV-Vis spectrophotometer (Varian) at the wavelengths of 400-800 nm.

6.2.4 Magnetic characterization of the nanoparticles

Magnetic properties of the cubic and spherical SPIONs with the sizes of 7.0, 11.0, and 13.5 nm were studied by measuring their magnetic field (M-H) and temperature dependent magnetizations (M-T). M-H and M-T curves of the SPIONs were recorded using a vibrating sample magnetometer (Quantum Design PPMS 6000).

6.2.5 Phantom Imaging

In order to investigate the longitudinal and transverse relaxivities of SPIONs, MR phantom experiments were performed using a 3T Siemens TrioTim MR scanner at room temperature. The sample concentrations in these experiments were 0.025, 0.05, 0.1, 0.2, 0.3, 0.4, and 1 mM. T_1- and T_2-weighted phantom MR images of SPIONs were acquired using spin echo (SE) sequence under the following parameters: TR/TE=3000/12 ms (T_1), TR/TE=2000/9.4, 15, 20, 30, 40, 50, 60, 70, 100, 150 ms (T_2), slice thickness=3 mm, flip angle=90°, acquisition matrix=256 pixels×256 pixel, field of view (FoV)=160×160mm^2.

6.3 Results and Discussion

Superparamagnetic iron oxide nanoparticles were synthesized according to a reported recipe with some modifications.[105] Briefly, high thermal decomposition of Fe-oleate method was employed and the growth of SPIONs in varying sizes and shapes were systematically studied by changing synthesis parameters (oleic acid, Fe-oleate and the heating rate). We first investigated the size and shape effect of oleic acid on SPIONs, which is a widely preferred organic molecule as stabilizer in the synthesis of different nanoparticles such as iron oxide nanoparticles[94], [187] and quantum dots.[10] We varied oleic acid concentration in the reaction mixture while keeping other parameters the same to understand its effect on the size and morphology of the nanoparticles. **Figure 6.1** shows the

TEM images of SPIONs with the sizes of 11.1±0.7, 10.0±0.6, 13.5±0.8, and 13.6±0.9 nm obtained from 0.8, 1.6, 1.9, and 2.4 mmol oleic acid added synthesis, respectively. In all of these syntheses, we kept the concentration of Fe-oleate and ODE to be 2.1 mmol and 25 mL, respectively. Images demonstrated that increased oleic acid amount favors the shape change from cube to sphere. Although a minor size increase (11.0 nm to 13.5 nm) was observed while the shape of SPIONs change from cube to sphere, we did not observe any significant difference in the size when we compared the two cubes (Figure 6.1a,b) and two spheres (Figure 6.1c,d) within each other. In the literature, Zhen *et al.*[209] demonstrated size decrease in the nanoparticles with the decreasing concentration of oleic acid, which is not observed in our study. Also, they reported cube SPION formation without oleic acid addition, which strongly supports our observation.

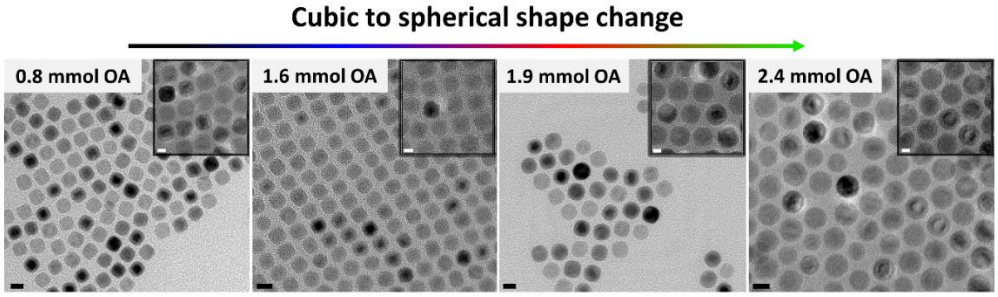

Figure 6.1. Size and shape variation of iron oxide nanoparticles (scale bar: 10 nm) as a function of the oleic acid amount in the reaction mixture together with zoom-in TEM images (scale bar: 5 nm) in the inset. Calculated average sizes are 11.1±0.7, 10.0±0.6, 13.5±0.8, and 13.6±0.9 nm for 0.8, 1.6, 1.9, and 2.4 mmol oleic acid (OA) added syntheses.

The iron oxide nanoparticles may be expected to become bigger with the increasing growth time. To test this hypothesis, we investigated the variation in the size and shape of the SPIONs in two different syntheses having homogenous or non-homogenous size distribution after 30 min and 5 h growth times. The experimental results demonstrated that the increasing growth time does not change the size and shape of the iron oxide nanoparticles (**Figure 6.2**). However, we observed that the increasing growth time slightly decreases the standard

deviation of nanoparticle size while keeping their average diameters the same. Based on this result, we continued our study by growing nanoparticles for 30 min at 320 °C.

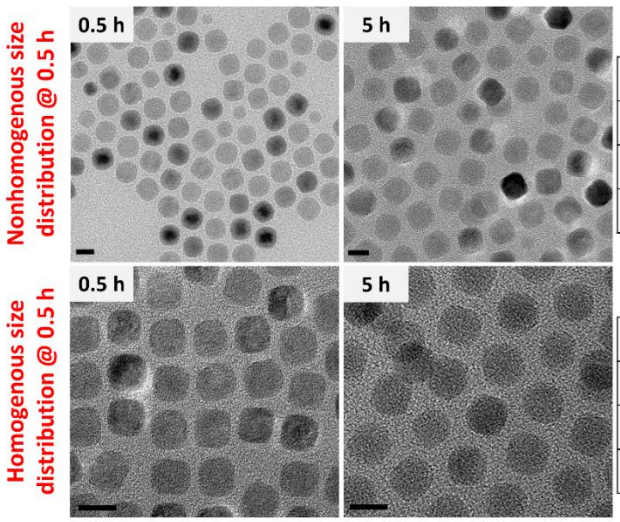

Synthesis Parameters

Fe-oleate	2.1 mmol
Oleic acid	1.9 mmol
ODE	25 mL
Heating rate	5.5 °C/min

Synthesis Parameters

Fe-oleate	2.1 mmol
Oleic acid	0.8 mmol
ODE	25 mL
Heating rate	5.5 °C/min

Figure 6.2. Difference in size and shape of iron oxide nanoparticles after 30 min and 5 h growth (Scale bars: 10 nm). Calculated average sizes for non-homogenous nanoparticles at 0.5 h are 11.5±1.4 and 11.8±1.2, for homogenous nanoparticles at 0.5 h are 9.89±0.4 and 10.82±0.5, respectively.

Iron-oleate concentration is known to be another parameter affecting the nanoparticle size and shape.[16] Since the concentration of oleic acid induce cubic or spherical shapes in our study, we investigated the effect of Fe-oleate concentration in both 2.4 mmol (sphere inducer) and 0.8 mmol (cube inducer) oleic acid consisting syntheses. TEM images of SPIONs synthesized using 2.4 mmol oleic acid are presented in **Figure 6.3**.

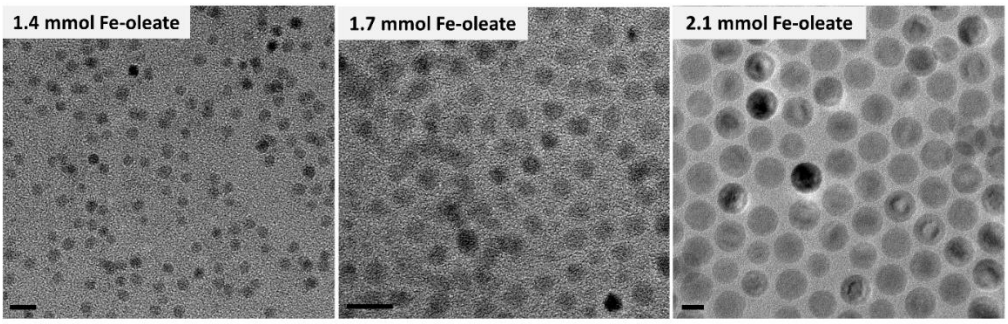

Figure 6.3. Iron oxide nanoparticles synthesized with indicated amounts of Fe-oleate using 2.4 mmol oleic acid and 25 mL ODE solution. Sizes of the nanoparticles were measured as 4.5±0.3, 4.3±0.4, and 13.6±0.9 nm, respectively (Scale bars: 10 nm).

We observed that there is a critical amount of Fe-oleate for a homogenous size distribution of iron oxide nanoparticles synthesized *via* high temperature decomposition method, which is found to be 2.1 mmol in our study. Moreover, the larger iron oxide nanoparticles having more homogenous size distribution suggests that decreased amounts of Fe-oleate do not allow the nanoparticles to grow enough after nucleation step leading to the formation of nanoparticles with sizes smaller than 5 nm. Therefore, we avoided lower concentrations of Fe-oleate for the 0.8 mmol oleic acid added syntheses and synthesized iron oxide nanoparticles using higher amounts of Fe-oleate (2.1 and 2.4 mmol). Results demonstrated that increased Fe-oleate triggers a slight size increase in the cubic iron oxide nanoparticles together with the significantly increased size distribution (**Figure 6.4**), which suggests higher concentrations of Fe-oleate also induce a nonhomogenous size distribution.

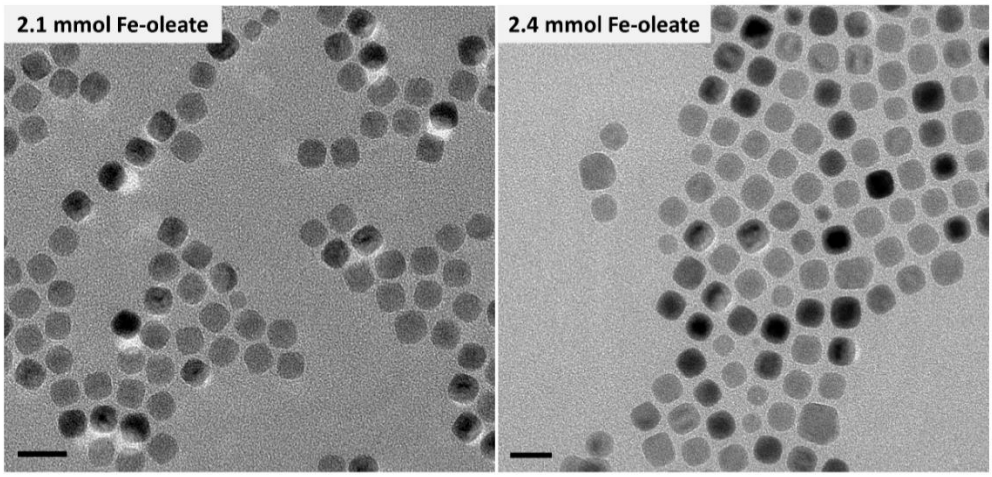

Figure 6.4. Iron oxide nanoparticles synthesized with varying amounts of Fe-oleate, 0.8 mmol oleic acid and 25 mL ODE solution. Average diameters were calculated as 11.0±0.7 and 12.9±1.8, respectively (Scale bars: 20 nm).

We also investigated the structural change of iron oxide nanoparticles synthesized with the temperature increase rates of 3.3, 4.2 and 5.5 °C min^{-1} for both 0.8 and 2.4 mmol oleic acid used syntheses. As depicted from **Figure 6.5**, increased heating rate of the reaction solution results in both size increase and spherical to cubic shape change in 0.8 mmol oleic acid including reactions, while only size change is observed in 2.4 mmol oleic acid added synthesis. The TEM images of 0.8 mmol oleic acid consisting syntheses showed that average diameters of the nanoparticles were 5.9±0.4, 8.9±1.3 and 11.0±0.7 nm for nanoparticles synthesized at a constant heating rate of 3.3, 4.2, and 5.5 °C min^{-1}, respectively. On the other hand, in the case of 2.4 mmol oleic acid used syntheses, we obtained spherical SPIONs with the decreasing diameters of 19.8±0.8, 16.9±0.7, and 10.8±0.4 nm at the same heating rates. We observe an opposite pattern in the diameter change with the increasing heating rates for 0.8 mmol and 2.4 mmol oleic acid added groups, however this change is more significant for 0.8 mmol oleic acid including groups. Higher amounts of oleic acid may possibly induce uniform growth of the nanoparticles by surrounding them homogenously. This is not possible for cubic SPIONs because of their anisotropic shape and low amount of oleic acid that they have. From these results, it can be concluded that the

oleic acid concentration in the reaction mixture is one of the most important parameters affecting the size and shape variation.

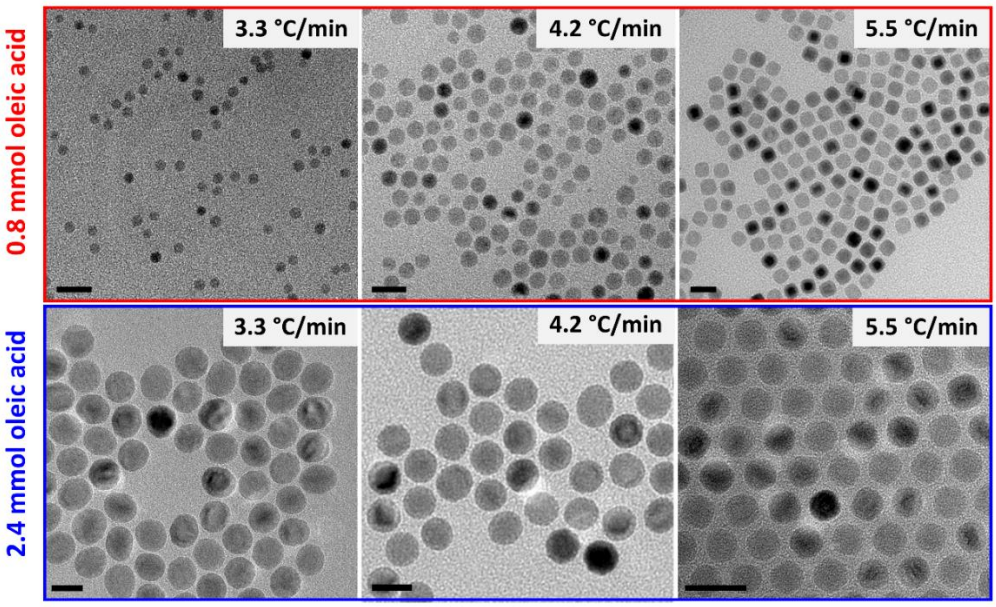

Figure 6.5. Influence of heating rate on the morphological change of iron oxide nanoparticles synthesized in the presence of 0.8 mmol and 2.4 mmol oleic acid. Average sizes of nanoparticles synthesized with 0.8 mmol oleic acid are measured as 5.9±0.4, 8.9±1.3 and 11.1±0.7 nm, while it is calculated as 19.8±0.8, 16.9±0.7, and 10.8±0.4 nm for 2.4 mmol oleic acid including syntheses (scale bars: 20 nm).

Following the investigation of size and shape affecting parameters, we examined the structural and magnetic properties of both cubic and spherical iron oxide nanoparticles having diameters of 7.0 nm, 11.0 nm, and 13.5 nm. The syntheses parameters and TEM images of the SPIONs were demonstrated in **Table 6.1** and **Figure 6.6**, respectively.

Table 6.1. Size, shape, and syntheses parameters of SPIONs represented in Figure 6.6.

	Size (nm)	**Fe-oleate (mmol)**	**Oleic acid (mmol)**	**ODE (mL)**	**Heating rate (°C min^{-1})**	**M_s (emu/g)**
CUBE	**7.0**	**2.1**	**0.8**	**25**	**5.3**	**24**
	11.0	**2.1**	**0.8**	**25**	**5.5**	**48**
	13.5	**2.1**	**1.9**	**25**	**5.5**	**45**
SPHERE	**7.0**	**2.1**	**0.8**	**25**	**3.3**	**14**
	11.0	**2.1**	**2.4**	**25**	**5.3**	**37**
	13.5	**2.1**	**2.4**	**25**	**5.5**	**43**

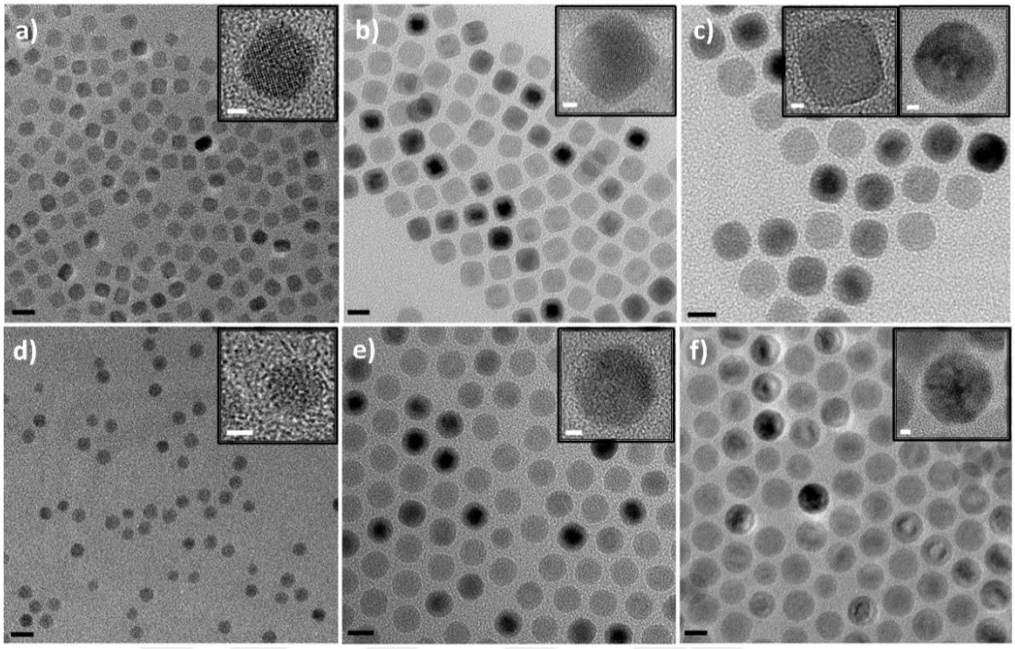

Figure 6.6. TEM images of the cubic (a-c) and spherical (d-f) SPIONs with the sizes of 7.0, 11.0, and 13.5 nm, respectively (Scale bars: 10 nm). Insets show the zoom-in images of a single particle (Scale bars: 2 nm).

In this synthesis route, since the iron oxide nanoparticles tend to become spherical with increasing particle size, we believe that the cubic SPIONs larger than 13.5 nm will tend to be more spherical than cubical shape. As depicted from Figure 6.6c, in the synthesis of 13.5 nm sized SPIONs, we observed both cubic and sphere-like nanoparticles. However, other syntheses resulted in monodisperse nanoparticles with the same shape. For the size analyses, both TEM and DLS measurements were performed, and DLS results supported the sizes calculated using TEM images **(Figure 6.7)**.

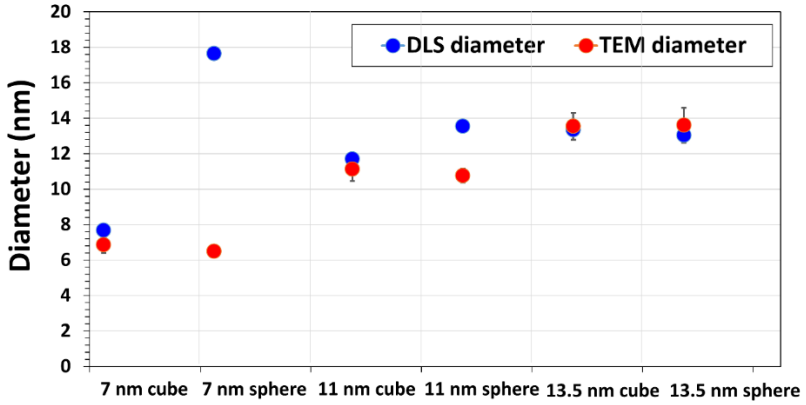

Figure 6.7. Size comparison of cube and sphere SPIONs analyzed by dynamic light scattering measurements along with their diameters calculated from TEM images.

We studied the absorption spectra of cubic and spherical SPIONs since it provides information about the crystal structure of the particles. Liang *et al.*[12] reported that Fe_3O_4 SPIONs exhibit an absorption band between 400-700 nm in the visible area, which is responsible from the black appearance of the SPION dispersion. Additionally, a very slight increase between 450 and 500 nm is also reported. On the other hand, the strongest peak for α-Fe_2O_3 is reported at 400-450 nm, which is in good aggrement with the red color of the solution. In our study, we observed the coverage of absorption spectrum of SPIONs throughout the whole visible regime in all groups. Considering the reported spectrum differences and solution colors of Fe_3O_4 and α-Fe_2O_3, we attributed our absorption spectrum to the formation of Fe_3O_4 nanocrystals (**Figure 6.8a**).

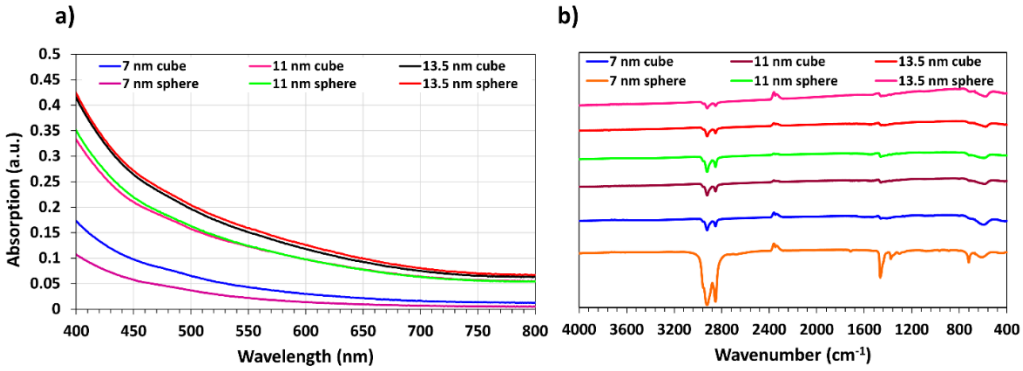

Figure 6.8. Structural information obtained from a) absorption spectra and surface characterization performed with b) FT-IR measurements.

To identify the functional groups of the SPIONs, we performed Fourier transform infrared spectroscopy (FTIR) measurements. The sharp peaks appearing at 2923, 2852, and 1461 cm^{-1} are assigned to the asymmetric stretching (υ_a C-H), symmetric stretching (υ_s C-H), and scissoring (δ_s C-H) modes of oleic acid, respectively (Figure 6.8b). These peaks are in agreement with the literature[213], [238] and indicate the oleic acid attachment to the SPION surface in a bidentate fashion in all groups.

We subsequently studied the magnetic properties of the SPIONs presented in Figure 6.6 using physical property measurement system (PPMS) to measure the dependence of magnetization on magnetic field (M-H curve) and on temperature (M-T). We recorded M-H curves at body temperature (310 K) because of their potential use in clinical MRI. The magnetization curve and saturation magnetization (M_s) of the all SPIONs are presented in **Figure 6.9** and Table 6.1.

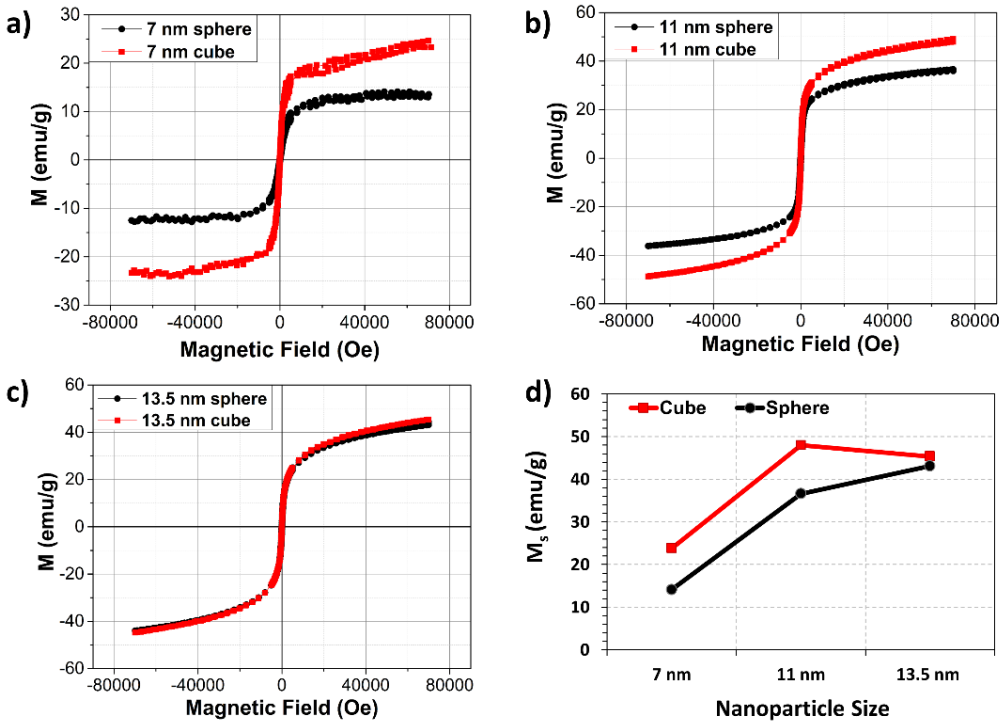

Figure 6.9. M-H curves of cube and sphere SPIONs having a) 7.0 nm, b) 11.0 nm and c) 13.5 nm diameters along with their d) saturation magnetization (M_s).

As depicted from Figures 6.9a-c, the continuous increase of magnetization along with the applied magnetic field observed in M-H curves can be explained by the enhanced spin canting effect in the surface layer.[187] When we compared the saturation magnetization values, we observed that the M_s values of cube SPIONs are higher than the spherical counterparts for all the sizes. Furthermore, we noticed that saturation magnetization increases with the increasing size for spherical SPIONs. This pattern is similar for cubic SPIONs with the sizes of 7.0 and 11.0 nm; however, a small decrease in 13.5 nm cubic SPIONs is observed. At this size (~13.5 nm), M_s values of the cubic and spherical SPIONs become very close to each other (~45 and ~43 emu/g, respectively). This size-dependent M_s decrease with decreasing size for both cube and sphere SPIONs may be attributed to the more adsorption of oleic acid by the nanoparticles' surface due to the larger surface area that they have or their crystalline defects inside the particle as also reported in previous works.[209], [213] In our study, we suggest that the decrease of M_s from 48 to 45 emu/g in 13.5 nm cube is possibly due to

the shape inhomogeneity of the solution. As shown in Figure 6.6c, this synthesis contains both sphere-like and cubic SPIONs.

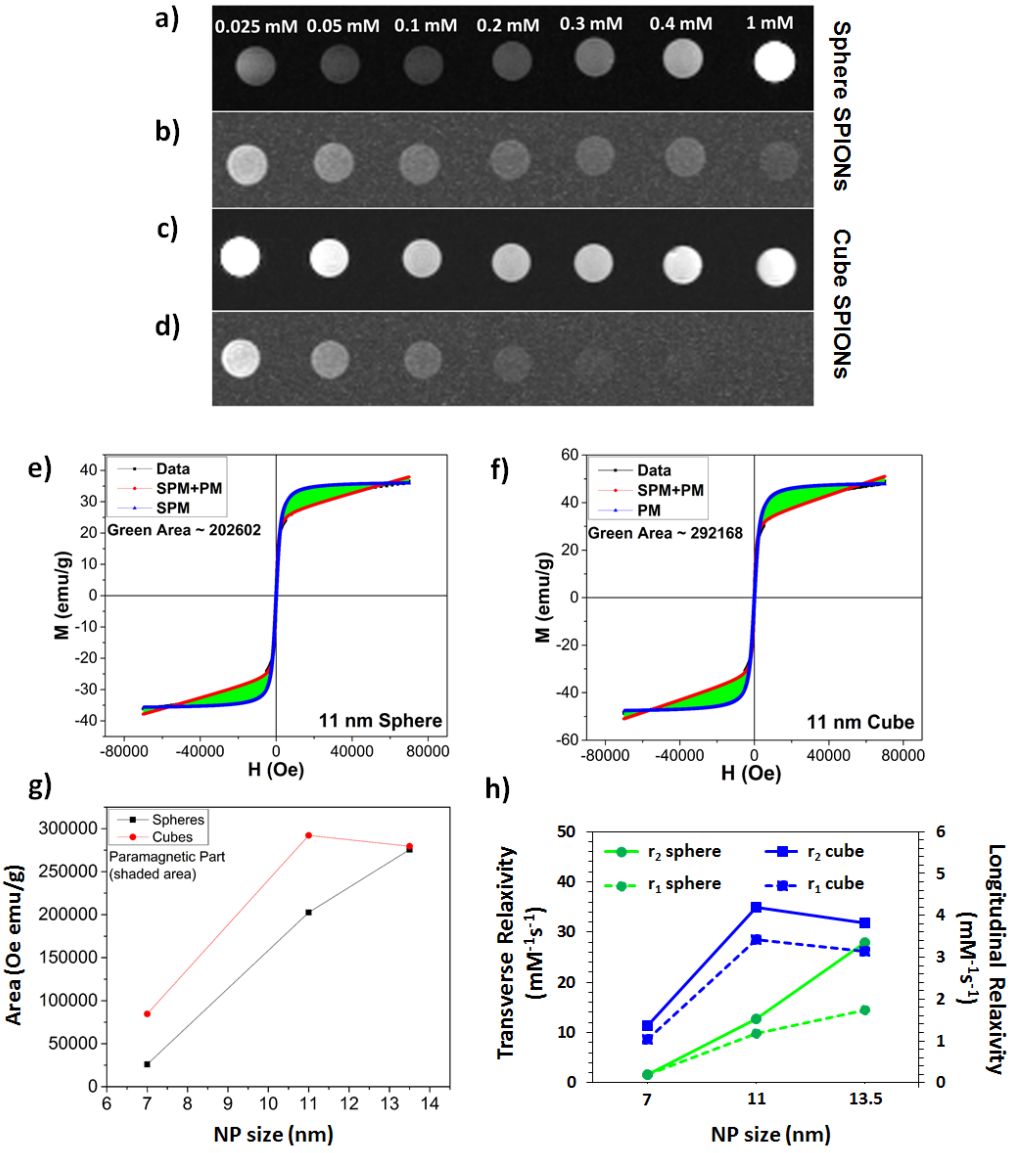

Figure 6.10. T_1- and T_2-weighted phantom images of a-b) sphere and c-d) cube SPIONs with the size of 11.0 nm. Diagrams of fitted M-H curves belonging to 11 nm sized e) sphere and f) cube SPIONs along with the g) areas showing the paramagnetic contribution in the M-H curves for all groups, which are calculated

from the green area in the fitted M-H curves. h) Transverse and longitudinal relaxivity values as a function of the SPION size.

Iron oxide nanoparticles are widely studied contrast agents for T_2-weighted imaging, however, there are a few reports on the use of these nanoparticles for dual-modal imaging.[19], [239] In order to understand the both transverse (r_2) and longitudinal relaxivity (r_1) mechanism depending on size and shape in SPIONs, we performed T_1- and T_2-weighted MR phantom imaging of cube and sphere SPIONs using a 3T Siemens MR scanner (**Figure 6.10** and **Figure 6.11**).

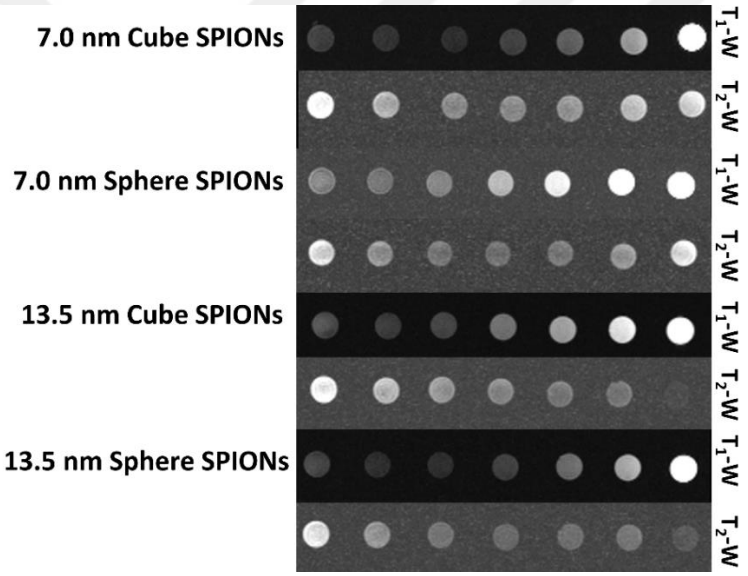

Figure 6.11. T_1- and T_2-weighted phantom images of cubic and spherical SPIONs with the sizes of 7.0 and 13.5 nm.

We observed that cubic SPIONs have larger r_1 and r_2 relaxivity values compared to the spherical counterparts for all sizes; however, there is a slight decrease in the r_1 and r_2 relaxivities of 13.5 nm sized cubic SPIONs. On the other hand, spherical SPIONs exhibited monotonically increasing relaxivities with increasing size. This result is in agreement with the M_s values shown in Figure 6.9d. For T_2-weighted imaging, the observation of improved contrast with the larger SPIONs is predictable since the larger particles have significantly higher magnetic moments due to their smaller surface contribution to spin canting.

Additionally, enhanced perturbation effects from the unique morphology also positively contributes to the T_2 contrast effect.[240] However, the origin of the r_1 relaxivity in SPIONs is not clear yet. In our study, while the r_2 and r_1 relaxivity values of cubic SPIONs (11 nm) are calculated as ~35 and ~3.4 $mM^{-1}s^{-1}$, Sharma *et al.* reported ~9.5 nm nanocubes with higher r_1 and r_2 values.[187] We believe that the reason of this difference is the spin-canting effect depending on the sharpness of nanocube corners. Therefore, higher relaxivity values could be obtained if the corners of our nanoparticles were sharper. A previous study[228] reported ultrahigh r_2 value from concave octapod iron oxide nanoparticles having sharp four-arm star like morphology, which strongly supports our hypothesis.
The continuous growth of magnetization along with the magnetic field suggests that these SPIONs may have a partially paramagnetic behavior in addition to their superparamagnetic nature. This paramagnetic property may possibly stem from the enhanced spin canting of SPIONs and similar result was reported in a study with cubic SPIONs previously.[187] These mixed magnetic phases were investigated by fitting the M-H curves of the samples using Equation 6.1.

$$M(T) = M_s \left[\coth\left(\frac{\mu H}{k_B T}\right) - \left(\frac{k_B T}{\mu H}\right)\right] + \chi H \qquad (\mathbf{6.1})$$

where M(T) represents the magnetization of the nanoparticles at temperature T, M_s shows the saturation magnetization of the nanoparticles, μ is the magnetic moment of the nanoparticles, χ is the susceptibility of the nanoparticles, and k_B is the Boltzmann constant.

The superparamagnetic (SPM) and paramagnetic (PM) contribution to the total magnetic moment can be observed in the first and second term of Equation 6.1, respectively. Experimental data and fits corresponding to sphere and cube iron oxide nanoparticles with the size of 11 nm are given in Figure 6.10e and f, respectively, while similar data for other nanoparticles are shown in **Figure 6.12**. Our experimental data and the SPM+PM fits, which are presented using black and red lines, respectively, matched perfectly suggesting the presence of SPM and PM phases. The green areas in the M-H curve graphs indicate the paramagnetic contribution. Figure 6g summarizes these green areas for all samples and exhibits excellent coherency with the patterns observed in M_s and

relaxation values. These results revealed that stronger paramagnetic contributions in the cubes compared to the spheres are responsible for larger r_1 relaxation values. It is also noteworthy mentioning that green areas calculated from M-H fits are similar for 13.5 nm of cube and sphere SPIONs, confirming the consistency of results obtained from M-H and relaxivity measurements (Figure 6.12). It is well understood from the literatue that the T_2 relaxivity is directly related to the saturation magnetization of the contrast material whereas T_1 relaxivity is associated with the paramagnetic contribution it possesses.[122] In our SPIONS, we can see a clear correlation of PM and SPM contributions with the longitudinal and transverse relaxivities, which we report here for undoped SPIONs for the first time to the best of our knowledge. We owe our results to the highly uniform/monodisperse synthesis of iron oxide nanoparticles.

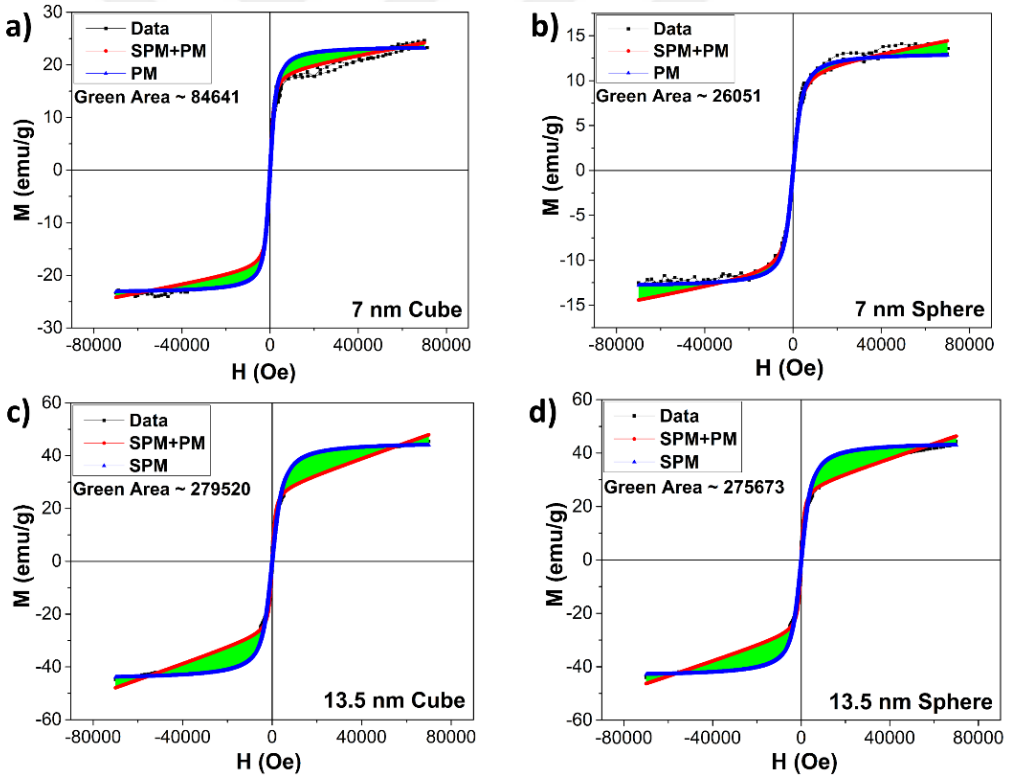

Figure 6.12. M-H fitting diagrams of a-b) 7.0 nm and c-d) 13.5 nm sized cube and sphere SPIONs

We also studied the magnetization dependence of our nanoparticles on temperature. We obtained zero field cooled (ZFC) magnetization by cooling in zero-field and field-cooled (FC) magnetization by warming in the presence of 300 Oe field following the cooling in zero-field. Results corresponding to the sphere and cube SPIONs having 11 nm diameter are presented in **Figure 6.13**. Results demonstrated that ZFC magnetizations of both cube and sphere SPIONs increase and reach a maximum at the blocking temperature (T_B). We observed that the ZFC magnetization of all cubic SPIONs is higher than the spherical SPIONs (**Figure 6.14**) and the values of T_B are estimated to be 135 and 120 K for 11 nm sized cube and sphere SPIONs, respectively.

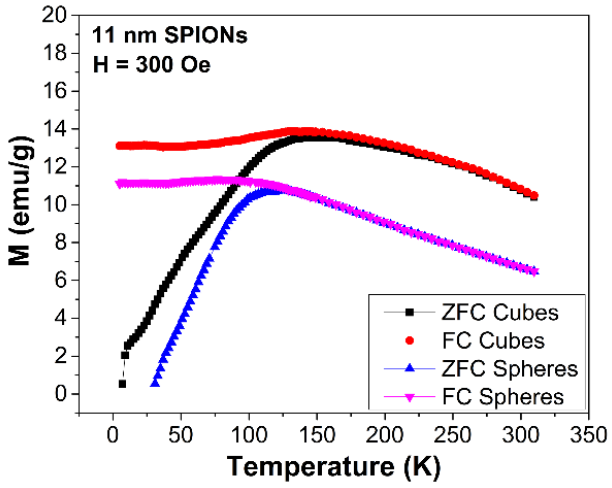

Figure 6.13. Zero field- and field-cooled M-T measurements of the cubic and spherical iron oxide nanoparticles having 11 nm size.

There is a conflict in the literature about the blocking temperature of the similar sized cube and sphere SPIONs. Salazar-Alvarez *et al.* reported that the blocking temperature of spherical shaped γ-Fe_2O_3 is higher than the cubic counterpart.[241] However, Zhen *et al.* reported that the Fe_3O_4 magnetite cubic SPIONs have higher blocking temperatures compared to the spherical counterparts, which is similar to our observation. The parameters affecting blocking temperature are shown in following Stoner-Wohlfarth relation:

$$T_B = \frac{K}{25k_B} * V \qquad \textbf{(6.2)}$$

where T_B is the blocking temperature, K is the anisotropy constant, V is the volume of the nanoparticles, and k_B is the Boltzmann constant. According to this relation, T_B is directly proportional to the magnetic anisotropy and the volume of the nanoparticles. Therefore, T_B increase with the increasing size and volume in both cube and sphere SPIONs is expected, and in agreement with our results. However, different than the M_s and relaxivity results, we observed a monotonic increase in the T_B of cubic SPIONs with the increasing size (Figure 6.14). Based on the Stoner-Wohlfarth relation, we attribute this variation to the differences in the shape anisotropy (cubes and spheres), which might originate from various factors such as broken exchange bonds, presence of structural defects (*e.g.*, facets), and differences in number of neighbors or atomic distances according to Neal's pair anisotropy model.[241] Considering the surface properties of our nanoparticles, all of these factors may take role in the magnetization anisotropy.

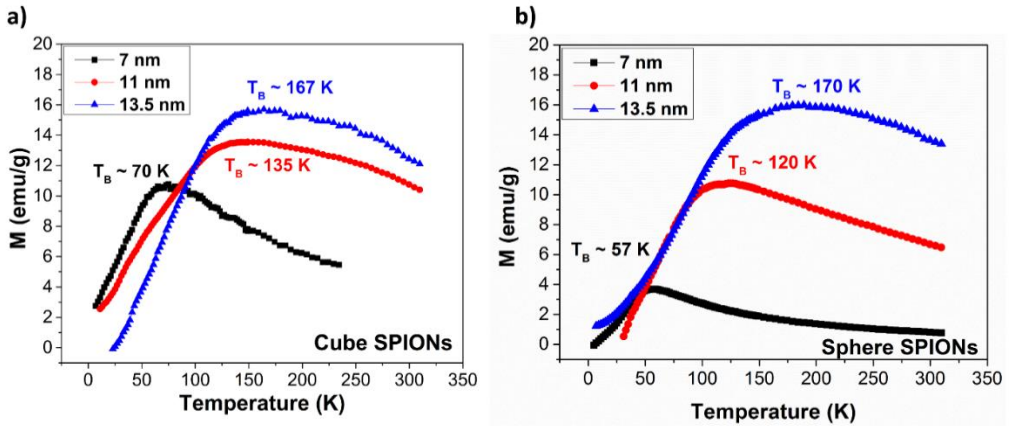

Figure 6.14. Zero field cooled measurements of a) cube and b) sphere SPIONs in three different sizes along with the blocking temperature values.

6.4 Summary

In this chapter, we show the colloidal synthesis of cubic and spherical superparamagnetic iron oxide nanoparticles of various sizes along with their structural and magnetic properties. In this study, for the first time, the longitudinal relaxivity of iron oxide nanoparticles, which are common T_2-weighted contrast agents, with different sizes and shapes was studied in detail. For this purpose, we synthesized spherical and cubic superparamagnetic iron

oxide nanoparticles using high-thermal decomposition method and investigated the key parameters to tune the size and shape of these nanoparticles. Morphological analyses demonstrated that oleic acid concentration is mainly responsible from shape change, and Fe-oleate amount in the reaction is crticial for size variation. Absorption measurements confirmed that SPIONs have magnetite (Fe_3O_4) crystal structure. MRI phantom studies demonstrated that cubic SPIONs have better relaxivity values as compared to the spherical counterparts, which is also supported by magnetic properties. Furthermore, M-H measurements showed that the magnetization saturation of cubic SPIONs is higher than spherical counterparts and both cube and sphere SPIONs have paramagnetic phase additionally to their superparamagnetic phase, which is confirmed by fitting the M-H curves. These PM and SPM contributions in our SPIONs are directly correlated with the longitudinal (r_1) and transverse (r_2) relaxivities. We believe that this study will open new pathways in the development of dual-modal (T_1 and T_2 weighted) iron oxide nanoparticles for magnetic resonance imaging.

Chapter 7

Conclusions

In this part of the thesis, we first summarize what we presented in this thesis and present our concluding remarks. Subsequently, we will continue with the future outlook and finish this chapter with a list of our contributions to the science and literature resulting from this thesis work.

7.1 Concluding Remarks

In this thesis, we prepared and used different colloidal nanoparticles for various targeted applications. First, we developed high-efficiency and high-stability new composite matrices suitable for solid-state lighting applications by employing colloidal conjugated polymer nanoparticles and colloidal semiconductor quantum dots. Additionally, we developed colloidal magnetic contrast agents that are promising for dual-modal imaging in MRI. We studied the effects of the size and shape of the nanoparticles on intrinsic mechanisms governing the magnetic features. After a brief introduction in Chapter 2, we started with providing background information on the syntheses, physical properties, and potential applications of different nanoparticles employed in this thesis work.

Subsequently, in Chapter 3, we focused on the problem of low quantum efficiency and stability of conjugated polymer nanoparticles for solid-state lighting applications. To address this challenge, here, we incorporated organic fluorescent oligomer nanoparticles into a nonionic sucrose matrix and prepared their monoliths. Optical characterizations of these monoliths revealed a significant QY increase up to ~44%, while it remains ~6% in drop-casted solid films. This is the first report that makes the use of oligomer nanoparticles suitable for solid-state lighting thanks to their high efficiency. Moreover, we conducted temperature stability studies of monoliths and drop-casted films, and showed ~3-fold improvement in the emission of oligomer nanoparticles within the monoliths. In addition to these advantages, easy preparation procedure, low cost, and easy implementation to LEDs are other impressive outcomes of this study. Interestingly, the use of ionic salt matrices instead of nonionic sucrose

matrix did not show similar improvement in the emission and stability of oligomer nanoparticles.

In the next chapter, we employed the nonradiative energy transfer to increase the emission efficiency of red quantum dots. For this aim, we incorporated quantum dots into cm-scale semiconductor organic anthracene crystals. We for the first time demonstrated the nonradiative energy transfer in crystalline matrices incorporating quantum dots. In this material system, the host matrix transferred their excitons to the incorporated quantum dots. We observed shortening in photoluminescence lifetime of the donor anthracene with the increasing amounts of incorporated QDs proving strengthening energy transfer. Since anthracene has several photoluminescence peaks, we systematically investigated the NRET and lifetime decays at every peak. Interestingly, we found out that the most efficient peak is not the main photoluminescence peak at 429 nm; instead, it is at 494 nm with a ratio of 28%. We further investigated the polarization of QD emission within the anthracene crystal. Results demonstrated an increased polarization ratio from ~1.5 to ~2.5 at the collection angles of 0° and 60°, respectively. Although it is known that anthracene has anisotropic nature, this study is the first report showing isotropic to anisotropic emission change of QDs within a crystalline matrix. Finally, we employed these QD-anthracene crystal system as color converter on LEDs by benefiting their NRET concept, and demonstrated their suitability as color-converters on LEDs.

In Chapter 5, we moved to our second focus, which is on the synthesis and characterization of biocompatible contrast agents for their use in magnetic resonance imaging. Here, we successfully synthesized highly monodisperse sharp cornered-cubic iron oxide nanoparticles with the size of ~9.7 nm by decomposing iron-oleate at high temperature. Characterization studies demonstrated that the crystal structure of these nanocubes is magnetite. Moreover, we studied both T_1- and T_2-weighted imaging capabilities of these nanocubes and showed their potential for dual-modal imaging in MRI. In the literature, there are two main techniques to increase T_1-imaging property of iron oxide nanoparticles. One of these tecniques is decreasing the size of the iron oxide nanocrystals below 5 nm, while the other one is doping iron oxide nanoparticles with paramagnetic

materials such as manganese and gadolinium. However, in this study, we obtained additional T_1-imaging capability only by tuning the shape. We also investigated their *in vitro* biocompatibility and dual-modal features in the phantom and MRI experiments, and showed they are safe and good candidates for simultaneously enhanced T_1- and T_2-imaging in MRI.

In Chapter 6, we investigated the intrinsic mechanisms leading to this T_1-contrast enhancement in iron oxide nanoparticles depending on their size and shape. Generally, iron oxide nanoparticles are known as T_2 contrast agents. Although there are some reports on their T_1-imaging capability, the related mechanisms remained unclear. Prior to this work, some studies reported enhanced r_1 relaxivity with the increasing size of iron oxide nanoparticles, while others reported the opposite. To understand the underlying physics behind this difference, we synthesized both cubic and spherical nanoparticles in three different sizes using high temperature decomposition of iron-oleate. Here, we systematically studied the synthesis parameters and found out that the oleic acid concentration mainly affects shape change, while Fe-oleate amount is crtitical for the size control. Magnetic characterizations, on the other hand, showed that cubic shaped iron oxide nanoparticles possess better r_1 and r_2 relaxivities compared to the sphere counterparts. Moreover, we found out that both superparamagnetic and paramagnetic phases are present within the crystal and saturation magnetization fittings match the pattern of these phase differences. Since r_1 mechanism of iron oxide nanoparticles is not clear, we believe that this study can further help to expand the applications of these biocompatible iron oxide nanoparticles as dual-modal contrast agents in MRI.

To summarize, within the framework of this graduate thesis work, we aimed to address problems of solid-state lighting and magnetic resonance imaging and find effective solutions to these problems. We believe that the scientific contributions of this thesis to the conjugated polymer nanoparticles and quantum dots are very promising and pave the way for their potential applications as color-converters in the lighting and display fields. Moreover, our studies on the development and improvement of iron oxide-based contrast agents for dual-modal MRI may help on better diagnosis of patients using MRI in the future.

7.2 Future Outlook

Cadmium-based quantum dots are widely preferred fluorescent nanoparticles as color-converters on LEDs owing to their high quantum yields. However, possible health and environmental risks of these materials, relatively low toxic conjugated polymers hold great promise for the future solid-state lighting applications. Our study presented in Chapter 3 is based on red-emitting oligomer nanoparticles. However, it would be very promising if we additionally obtain highly efficient yellow- or green-emitting oligomer nanoparticles and use all of them for the white light applications.

Moreover, in our study, we used quantum dots as inorganic fluorescent nanoparticles. However, two-dimensional nanoplatelets are also very attractive thanks to their narrow emission spectra. However, their stability and efficiency in solid films still remain as important problems. The crystallization of these materials can be a good solution to these problems, which may make the nanoplatelets suitable for displays and lighting. Additionally, perovskite nanoparticles are another promising materials that can be employed in lighting applications. If their emission efficiency and stability can be increased to relatively higher levels by using crystallization techniques, it would be another promising approach for the optoelectronic applications.

MRI is among the most widely used non-invasive imaging tools in the clinics for the diagnosis and treatment of diseases. To date, many studies have been conducted to develop agents for improved image contrast. However, in the last decades, magnetic particle imaging (MPI) has attracted significant attention by many researchers. In this technique, the signals are obtained directly from the contrast agents. On the other hand, in MRI, contrast agents are indirectly detected by measuring the relaxation time difference of protons residing in the environmental tissues. Therefore, MPI provides high-resolution real-time imaging and it is principally a technique utilizing specifically iron oxide-based nanoparticle tracers. We believe that the well-controlled monodisperse iron oxide nanoparticle syntheses with different sizes and shapes may also step forward in this area. Moreover, for the treatment of cancer, hyperthermia is a good

alternative and the anisotropic materials possess better heat generation. Since similar contrast agents are employed for the MPI and hyperthermia studies, the idea of developing a material combining the features required by both the MPI and hyperthermia is very promising. We believe that focusing on these research fields may significantly contribute to the literature and industry in the near future.

7.3 Contributions

7.3.1 SCI Journals

1. **Z. Soran-Erdem**, V. Kumar Sharma, A. Alipour, P. L. Hernandez-Martinez, and H. V. Demir, "Direct Correlation of T_1 and T_2 Relaxivities in Highly Monodispersed Iron Oxide Nanoparticles," (2016) (*submitted*).
2. M. Adam, N. Gaponik, A. Eychmüller, T. Erdem, **Z. Soran-Erdem**, and H. V. Demir, "Colloidal Nanocrystals Embedded in Macrocrystals: Methods and Applications," *J. Phys. Chem. Lett.* 7, 4117–4123 (2016).
3. **Z. Soran-Erdem***, T. Erdem*, K. Gungor, J. Pennakalathil, D. Tuncel, H. V. Demir, "High-stability, high-efficiency organic monoliths made of oligomer nanoparticles wrapped in organic matrix," *ACS Nano* 10, 5333 (2016). *Equal contribution
4. V. K. Sharma, A. Alipour, **Z. Soran-Erdem**, Y. Kelestemur, Z. G. Aykut, and H. V. Demir, "Fluorescent Heterodoped Nanotetrapods as Synergistically Enhancing Positive and Negative Magnetic Resonance Imaging Contrast Agents", *ACS Applied Materials & Interfaces 8*, 12352–12359 (2016).
5. T. Erdem*, **Z. Soran-Erdem***, Y. Kelestemur, N. Gaponik and H. V. Demir, "Excitonic improvement of colloidal nanocrystals in salt powder matrix for quality lighting and color enrichment," *Optics Express* 24, A74 (2016). *Equal contribution
6. M. Adam, Z. Wang, A. Dubavik, G. M. Stachowski, C. Meerbach, **Z. Soran-Erdem**, C. Rengers, H. V. Demir, N. Gaponik, and A.

Eychmüller, "Liquid–Liquid Diffusion-Assisted Crystallization: A Fast and Versatile Approach Toward High Quality Mixed Quantum Dot-Salt Crystals," *Adv. Funct. Mater. 25*, 2638–2645, (2015).

7. M. Adam*, T. Erdem*, G. Stachowski, **Z. Soran-Erdem**, J. Lox, C. Bauer, J. Poppe, H. V. Demir, N. Gaponik, A. Eychmüller, "Implementation of high-quality warm-white light-emitting diodes by a model-experimental feedback approach using quantum dot-salt mixed crystals," *ACS Appl. Mater. Inter.* 7, 23364 (2015). *Equal contribution
8. V. K. Sharma, A. Alipour, **Z. Soran-Erdem**, Z. G. Aykut, and H. V. Demir, "Highly monodisperse low-magnetization magnetite nanocubes as simultaneous T_1-T_2 MRI contrast agents," *Nanoscale 8*, 7, 10519–10526, (2015).
9. **Z. Soran-Erdem***, T. Erdem*, P. L. Hernandez-Martinez, M. Z. Akgul, N. Gaponik, H. V. Demir, "Macrocrystals of colloidal quantum dots in anthracene: exciton transfer and polarized emission," *J. Phys. Chem. Lett.* 6, 1767-1772 (2015). *Equal contribution
10. T. Erdem*, **Z. Soran-Erdem***, V. K. Sharma, Y. Kelestemur, M. Adam, N. Gaponik and H. V. Demir, "Stable and efficient colour enrichment powders of nonpolar nanocrystals in LiCl," *Nanoscale* 7, 17611 (2015). *Selected as cover article*, *Equal contribution
11. T. Erdem, **Z. Soran-Erdem**, P. L. Hernandez-Martinez, V. K. Sharma, H. Akcali, I. Akcali, N. Gaponik, A. Eychmüller, H. V. Demir, "Sweet plasmonics: Sucrose macrocrystals of metal nanoparticles," *Nano Research* 8, 860-869 (2015).
12. T. Erdem, Y. Kelestemur, **Z. Soran-Erdem**, Y. Ji, H. V. Demir, "Energy-saving quality road lighting with colloidal quantum dot nanophosphors" *Nanophotonics* 3, 373-381 (2014). *Selected as cover article.*

7.3.2 International Conferences

1. **Z. Soran-Erdem**, T. Erdem, P. L. Hernandez-Martinez, M. Z. Akgul, N. Gaponik, H. V. Demir, "Macrocrystals of colloidal quantum dots in anthracene: Exciton transfer and polarized emission," *APS Meeting*, Baltimore, Maryland, USA, March 2016.
2. T. Erdem, Y. Kelestemur, **Z. Soran-Erdem**, Y. Ji, H. V. Demir, "High-efficiency high-quality street lighting with colloidal quantum dot nanophosphors," *IEEE Photonics Conferenc*e, Reston, VA, USA, October 2015.
3. **Z. Soran-Erdem**, T. Erdem, P. L. Hernandez-Martinez, M. Z. Akgul, N. Gaponik, H. V. Demir, "Exciton transfer and polarized emission in colloidal quantum dot – anthracene crystals," *IEEE Photonics Conference*, Reston, VA, USA, October 2015.
4. P. L. Hernandez-Martinez, T. Erdem, **Z. Soran-Erdem**, V. K. Sharma, H. Akcali, I. Akcali, N. Gaponik, A. Eychmüller, H. V. Demir, "Sweet plasmonics: Sucrose macrocrystals of metal nanoparticles" *APS Meeting*, San Antonio, Texas, USA, March 2015.
5. T. Erdem, **Z. Soran-Erdem**, P. L. Hernandez-Martinez, V. K. Sharma, N. Gaponik, A. Eychmüller, and H. V. Demir, "Macrocrystals of co-immobilized semiconductor nanocrystals and metal nanoparticles," *NANAX 6*, Bad Hofgastein, Salzburg, Austria, May 2014.

Bibliography

[1] M. R. Krames, O. B. Shchekin, R. Mueller-Mach, G. O. Mueller, L. Zhou, G. Harbers, and M. G. Craford, "Status and Future of High-Power Light-Emitting Diodes for Solid-State Lighting," *J. Disp. Technol.*, vol. 3, no. 2, pp. 160–175, Jun. 2007.

[2] D. Hendricks, "Mobile Use And The New Customer Experience." [Online]. Available:http://www.forbes.com/sites/drewhendricks/2014/08/06/mobile-use-and-the-new-customer-experience/#595b7b427d9b.

[3] T. Erdem and H. V. Demir, "Colloidal nanocrystals for quality lighting and displays: milestones and recent developments," *Nanophotonics*, vol. 5, no. 1, pp. 74-95, 2016.

[4] T. Erdem and H. V. Demir, "Color science of nanocrystal quantum dots for lighting and displays," *Nanophotonics*, vol. 2, no. 1, pp. 57–81, 2013.

[5] T. Erdem, S. Nizamoglu, and H. V. Demir, "Computational study of power conversion and luminous efficiency performance for semiconductor quantum dot nanophosphors on light-emitting diodes," *Opt. Express*, vol. 20, no. 3, p. 3275, 2012.

[6] O. Graydon, "The new oil?," *Nat. Photonics*, vol. 5, no. 1, p. 1, 2011.

[7] T. Erdem and H. V. Demir, "Semiconductor nanocrystals as rare-earth alternatives," *Nat. Photonics*, vol. 5, no. 1, p. 126, 2011.

[8] L. Ye, K.-T. Yong, L. Liu, I. Roy, R. Hu, J. Zhu, H. Cai, W.-C. Law, J. Liu, K. Wang, J. Liu, Y. Liu, Y. Hu, X. Zhang, M. T. Swihart, and P. N. Prasad, "A pilot study in non-human primates shows no adverse response to intravenous injection of quantum dots," *Nat. Nanotechnol.*, vol. 7, no. 7, pp. 453–458, 2012.

[9] T. Otto, M. Müller, P. Mundra, V. Lesnyak, H. V. Demir, N. Gaponik, and A. Eychmüller, "Colloidal nanocrystals embedded in macrocrystals: Robustness, photostability, and color purity," *Nano Lett.*, vol. 12, no. 10, pp. 5348–5354, 2012.

[10] T. Erdem, Z. Soran-Erdem, V. K. Sharma, Y. Kelestemur, M. Adam, N.

Gaponik, and H. V. Demir, "Stable and efficient colour enrichment powders of nonpolar nanocrystals in LiCl," *Nanoscale*, vol. 7, no. 42, pp. 17611–17616, 2015.

[11] T. Erdem, Z. Soran-Erdem, P. L. Hernandez-Martinez, V. K. Sharma, H. Akcali, I. Akcali, N. Gaponik, A. Eychmüller, and H. V. Demir, "Sweet plasmonics: Sucrose macrocrystals of metal nanoparticles," *Nano Res.*, vol. 8, no. 3, pp. 860–869, 2015.

[12] M. Adam, Z. Wang, A. Dubavik, G. M. Stachowski, C. Meerbach, Z. Soran-Erdem, C. Rengers, H. V. Demir, N. Gaponik, and A. Eychmüller, "Liquid-Liquid diffusion-assisted crystallization: A fast and versatile approach toward high quality mixed quantum dot-salt crystals," *Adv. Funct. Mater.*, vol. 25, no. 18, pp. 2638–2645, 2015.

[13] M. Müller, M. Kaiser, G. M. Stachowski, U. Resch-Genger, N. Gaponik, and A. Eychmüller, "Photoluminescence quantum yield and matrix-induced luminescence enhancement of colloidal quantum dots embedded in ionic crystals," *Chem. Mater.*, vol. 26, no. 10, pp. 3231–3237, 2014.

[14] M. Z. Iqbal, X. Ma, T. Chen, L. Zhang, W. Ren, L. Xiang, and A. Wu, "Silica-coated super-paramagnetic iron oxide nanoparticles (SPIONPs): A new type contrast agent of T_1 magnetic resonance imaging (MRI)," *J. Mater. Chem. B*, vol. 3, no. 26, pp. 5172–5181, 2015.

[15] D. Pan, A. H. Schmieder, S. A. Wickline, and G. M. Lanza, "Manganese-based MRI contrast agents: past, present and future," *Tetrahedron*, vol. 67, no. 44, pp. 8431–8444, 2011.

[16] J. S. Weinstein, C. G. Varallyay, E. Dosa, S. Gahramanov, B. Hamilton, W. D. Rooney, L. L. Muldoon, and E. A. Neuwelt, "Superparamagnetic iron oxide nanoparticles: diagnostic magnetic resonance imaging and potential therapeutic applications in neurooncology and central nervous system inflammatory pathologies, a review," *J. Cereb. Blood Flow Metab.*, vol. 30, no. 1, pp. 15–35, 2010.

[17] V. K. Sharma, A. Alipour, Z. Soran-Erdem, Z. G. Aykut, and H. V. Demir, "Highly monodisperse low-magnetization magnetite nanocubes as simultaneous T1 –T2 MRI contrast agents," *Nanoscale*, vol. 7, no. 23, pp. 10519–10526, 2015.

[18] Z. Li, P. W. Yi, Q. Sun, H. Lei, H. Li Zhao, Z. H. Zhu, S. C. Smith, M. B. Lan, and G. Q. (Max) Lu, "Ultrasmall water-soluble and Biocompatible magnetic iron oxide nanoparticles as positive and negative dual contrast agents," *Adv. Funct. Mater.*, vol. 22, no. 11, pp. 2387–2393, 2012.

[19] Z. Zhou, D. Huang, J. Bao, Q. Chen, G. Liu, Z. Chen, X. Chen, and J. Gao, "A synergistically enhanced T1-T2 dual-modal contrast agent," *Adv. Mater.*, vol. 24, no. 46, pp. 6223–6228, 2012.

[20] J. Drbohlavova, V. Adam, R. Kizek, and J. Hubalek, "Quantum dots - characterization, preparation and usage in biological systems," *Int. J. Mol. Sci.*, vol. 10, no. 2, pp. 656–673, 2009.

[21] T. Erdem, "Color science and technology of novel nanophosphors for high-efficiency high-quality LEDs," Bilkent University, 2011.

[22] A. Valizadeh, H. Mikaeili, M. Samiei, S. M. Farkhani, and N. Zarghami, M. Kouhi, A. Akbarzadeh and S. Davaran, "Quantum dots: Synthesis, bioapplications, and toxicity," *Nanoscale Res. Lett.*, vol. 7, p. 480, 2012.

[23] B. Mahler, P. Spinicelli, S. Buil, X. Quelin, J. P. Hermier, and B. Dubertret, "Towards non-blinking colloidal quantum dots," *Nat. Mater.*, vol. 7, no. 8, pp. 659–664, 2008.

[24] Y. Shi, P. He, and X. Zhu, "Photoluminescence-enhanced biocompatible quantum dots by phospholipid functionalization," *Mater. Res. Bull.*, vol. 43, no. 10, pp. 2626–2635, 2008.

[25] Hari Singh Nalwa, *Quantum Dots and Nanowires*. American Scientific Publishers, 2003.

[26] P. Reiss, "Synthesis of semiconductor nanocrystals in organic solvents," in *Semiconductor Nanocrystal Quantum Dots: Synthesis, Assembly, Spectroscopy and Applications*, A. L. Rogach, Ed. Vienna: Springer Vienna, 2008, pp. 35–72.

[27] W. W. Yu, L. Qu, W. Guo, and X. Peng, "Experimental determination of the extinction coefficient of CdTe, CdSe, and CdS nanocrystals," *Chem. Mater.*, vol. 15, no. 14, pp. 2854–2860, 2003.

[28] A. L. Rogach, T. Franzl, T. A. Klar, J. Feldmann, N. Gaponik, V.

Lesnyak, A. Shavel, A. Eychmüller, Y. P. Rakovich, and J. F. Donegan, "Aqueous synthesis of thiol-capped CdTe nanocrystals: State-of-the-art," *J. Phys. Chem. C*, vol. 111, no. 40, pp. 14628–14637, 2007.

[29] G. Iyer, F. Pinaud, J. Tsay, and S. Weiss, "Solubilization of quantum dots with a recombinant peptide from escherichia coli," *Small*, vol. 3, no. 5, pp. 793–798, 2007.

[30] C. Q. Zhu, P. Wang, X. Wang, and Y. Li, "Facile phosphine-free synthesis of CdSe/ZnS core/shell nanocrystals without precursor injection," *Nanoscale Res. Lett.*, vol. 3, no. 6, pp. 213–220, 2008.

[31] G. Zhenyu, Z. Lei, F. Zheng, Z. Weihong, and Z. Xinhua, "One-pot synthesis of highly luminescent CdTe/CdS core/shell nanocrystals in aqueous phase," *Nanotechnology*, vol. 19, no. 13, p. 135604, 2008.

[32] A. Sashchiuk, D. Yanover, A. Rubin-Brusilovski, G. I. Maikov, R. K. Čapek, R. Vaxenburg, J. Tilchin, G. Zaiats, and E. Lifshitz, "Tuning of electronic properties in IV-VI colloidal nanostructures by alloy composition and architecture," *Nanoscale*, vol. 5, no. 17, pp. 7724–45, 2013.

[33] B. O. Dabbousi, J. Rodriguez, F. V Mikulec, J. R. Heine, H. Mattoussi, R. Ober, K. F. Jensen, and M. G. Bawendi, "(CdSe)ZnS core-shell quantum dots : Synthesis and characterization of a size series of highly luminescent nanocrystallites," *J. Phys. Chem. B*, vol. 101, no. 97, pp. 9463–9475, 1997.

[34] E. Mutlugun, "Exciton Harvesting Systems of Nanocrystals," Bilkent University, 2011.

[35] O. Chen, J. Zhao, V. P. Chauhan, J. Cui, C. Wong, D. K. Harris, H. Wei, H.-S. Han, D. Fukumura, R. K. Jain, and M. G. Bawendi, "Compact high-quality CdSe-CdS core-shell nanocrystals with narrow emission linewidths and suppressed blinking," *Nat. Mater.*, vol. 12, no. 5, pp. 445–51, 2013.

[36] W. K. Bae, K. Char, H. Hur, and S. Lee, "Single-step synthesis of quantum dots with chemical composition gradients," *Chem. Mater.*, vol. 20, no. 2, pp. 531–539, 2008.

[37] J. N. Tiwari, R. N. Tiwari, and K. S. Kim, "Zero-dimensional, one-

dimensional, two-dimensional and three-dimensional nanostructured materials for advanced electrochemical energy devices," *Prog. Mater. Sci.*, vol. 57, no. 4, pp. 724–803, 2012.

[38] Y. Yuan and M. Krüger, "Polymer-nanocrystal hybrid materials for light: Conversion applications," *Polymers (Basel).*, vol. 4, no. 1, pp. 1–19, 2012.

[39] B. Guzelturk, Y. Kelestemur, K. Gungor, A. Yeltik, M. Z. Akgul, Y. Wang, R. Chen, C. Dang, H. Sun, and H. V. Demir, "Stable and low-threshold optical gain in CdSe/CdS quantum dots: An all-colloidal frequency up-converted laser," *Adv. Mater.*, vol. 27, no. 17, pp. 2741–2746, 2015.

[40] R. D. Schaller, M. a Petruska, and V. I. Klimov, "Tunable near-infrared optical gain and amplified spontaneous emission using PbSe nanocrystals," *J. Phys. Chem. B*, vol. 107, no. 50, pp. 13765–13768, 2003.

[41] V. I. Klimov, A. A. Mikhailovsky, S. Xu, A. Malko, J. A. Hollingsworth, C. A. Leatherdale, H.-J. Eisler, and M. G. Bawendi, "Optical gain and stimulated emission in nanocrystal quantum dots," *Science*, vol. 290, no. 5490, pp. 314–317, 2000.

[42] M. Ishido and N. Kasuga, "In situ real-time imaging of the satellite cells in rat intact and injured soleus muscles using quantum dots," *Histochem. Cell Biol.*, vol. 135, no. 1, pp. 21–26, 2011.

[43] P. Wu, Y. He, H. F. Wang, and X. P. Yan, "Conjugation of glucose oxidase onto Mn-doped ZnS quantum dots for phosphorescent sensing of glucose in biological fluids," *Anal. Chem.*, vol. 82, no. 4, pp. 1427–1433, 2010.

[44] C. Huang, S. Liu, T. Chen, and Y. Li, "A new approach for quantitative determination of glucose by using CdSe/ZnS quantum dots," *Sensors Actuators B Chem.*, vol. 130, no. 1, pp. 338–342, 2008.

[45] I. L. Medintz, M. H. Stewart, S. a Trammell, K. Susumu, J. B. Delehanty, B. C. Mei, J. S. Melinger, J. B. Blanco-Canosa, P. E. Dawson, and H. Mattoussi, "Quantum-dot/dopamine bioconjugates function as redox coupled assemblies for in vitro and intracellular pH sensing," *Nat. Mater.*, vol. 9, no. 8, pp. 676–684, 2010.

[46] M. Tomasulo, I. Yildiz, and F. M. Raymo, "pH-sensitive quantum dots," *J. Phys. Chem. B*, vol. 110, no. 9, pp. 3853–3855, 2006.

[47] F. Zhang, Z. Ali, F. Amin, A. Feltz, M. Oheim, and W. J. Parak, "Ion and pH sensing with colloidal nanoparticles: influence of surface charge on sensing and colloidal properties," *ChemPhysChem*, vol. 11, no. 3, pp. 730–735, 2010.

[48] K. M. Molapo, P. M. Ndangili, R. F. Ajayi, G. Mbambisa, S. M. Mailu, N. Njomo, M. Masikini, P. Baker, and E. I. Iwuoha, "Electronics of conjugated polymers (I): Polyaniline," *Int. J. Electrochem. Sci.*, vol. 7, no. 12, pp. 11859–11875, 2012.

[49] L. Feng, C. Zhu, H. Yuan, L. Liu, F. Lv, and S. Wang, "Conjugated polymer nanoparticles: preparation, properties, functionalization and biological applications.," *Chem. Soc. Rev.*, vol. 42, no. 16, pp. 6620–33, 2013.

[50] J. Pecher and S. Mecking, "Nanoparticles of conjugated polymers," *Chem. Rev.*, vol. 110, no. 10, pp. 6260–6279, 2010.

[51] N. Kurokawa, H. Yoshikawa, N. Hirota, K. Hyodo, and H. Masuhara, "Size-dependent spectroscopic properties and thermochromic behavior in poly(substituted thiophene) nanoparticles," *ChemPhysChem*, vol. 5, no. 10, pp. 1609–1615, 2004.

[52] C. Szymanski, C. Wu, J. Hooper, M. A. Salazar, A. Perdomo, A. Dukes, and J. McNeill, "Single molecule nanoparticles of the conjugated polymer MEH-PPV, preparation and characterization by near-field scanning optical microscopy," *J. Phys. Chem. B*, vol. 109, no. 18, pp. 8543–8546, 2005.

[53] J. Luo, Z. Xie, J. W. Y. Lam, L. Cheng, B. Z. Tang, H. Chen, C. Qiu, H. S. Kwok, X. Zhan, Y. Liu, and D. Zhu, "Aggregation-induced emission of 1-methyl-1,2,3,4,5-pentaphenylsilole," *Chem. Commun.*, vol. 381, no. 18, pp. 1740–1741, 2001.

[54] B. K. An, S. K. Kwon, S. D. Jung, and S. Y. Park, "Enhanced emission and its switching in fluorescent organic nanoparticles," *J. Am. Chem. Soc.*, vol. 124, no. 48, pp. 14410–14415, 2002.

[55] H. Tong, Y. Hong, Y. Dong, M. Häussler, J. W. Y. Lam, Z. Li, Z. Guo, Z. Guo, and B. Z. Tang, "Fluorescent 'light-up' bioprobes based on tetraphenylethylene derivatives with aggregation-induced emission characteristics," *Chem. Commun.*, no. 35, pp. 3705–3707, 2006.

[56] H.-H. Lin, S.-Y. Su, and C.-C. Chang, "Fluorescent organic nanoparticle formation in lysosomes for cancer cell recognition," *Org. Biomol. Chem.*, vol. 7, no. 10, pp. 2036–2039, 2009.

[57] S. Reineke, F. Lindner, G. Schwartz, N. Seidler, K. Walzer, B. Lüssem, and K. Leo, "White organic light-emitting diodes with fluorescent tube efficiency," *Nature*, vol. 459, no. 7244, pp. 234–8, 2009.

[58] L. Duan, L. Hou, T.-W. Lee, J. Qiao, D. Zhang, G. Dong, L. Wang, and Y. Qiu, "Solution processable small molecules for organic light-emitting diodes," *J. Mater. Chem.*, vol. 20, no. 31, pp. 6392 – 6407, 2010.

[59] A. Kaeser and A. P. H. J. Schenning, "Fluorescent nanoparticles based on self-assembled-conjugated systems," *Adv. Mater.*, vol. 22, no. 28, pp. 2985–2997, 2010.

[60] J. Pennakalathil, E. Jahja, E. S. Ozdemir, O. Konu, and D. Tuncel, "Red emitting, cucurbituril-capped, pH-responsive conjugated oligomer-based nanoparticles for drug delivery and cellular imaging," *Biomacromolecules*, vol. 15, pp. 3366–3374, 2014.

[61] Z. Soran-erdem, T. Erdem, K. Gungor, J. Pennakalathil, and H. V. Demir, "High-stability, high-efficiency organic monoliths made of oligomer nanoparticles wrapped in organic matrix," *ACS Nano*, vol. 10, pp. 5333-5339, 2016.

[62] C. Wu, B. Bull, C. Szymanski, K. Christensen, and J. McNeill, "Multicolor conjugated polymer dots for biological fluorescence imaging," *ACS Nano*, vol. 2, no. 11, pp. 2415–2423, 2008.

[63] J. H. Moon, W. McDaniel, P. MacLean, and L. F. Hancock, "Live-cell-permeable poly(p-phenylene ethynylene)," *Angew. Chemie*, vol. 119, no. 43, pp. 8371–8373, 2007.

[64] C. Wu, S. J. Hansen, Q. Hou, J. Yu, M. Zeigler, Y. Jin, D. R. Burnham, J. D. McNeill, J. M. Olson, and D. T. Chiu, "Design of highly emissive

polymer dot bioconjugates for in vivo tumor targeting," *Angew. Chemie - Int. Ed.*, vol. 50, no. 15, pp. 3430–3434, 2011.

[65] I. Fischer, A. Kaeser, M. A. M. Peters-Gumbs, and A. P. H. J. Schenning, "Fluorescent π-conjugated polymer dots versus self-assembled small-molecule nanoparticles: What's the difference?," *Chem. A Eur. J.*, vol. 19, no. 33, pp. 10928–10934, 2013.

[66] D. Tuncel and H. V. Demir, "Conjugated polymer nanoparticles," *Nanoscale*, vol. 2, no. 4, p. 484, 2010.

[67] B. S. Ong, Y. Wu, P. Liu, and S. Gardner, "Structurally ordered polythiophene nanoparticles for high-performance organic thin-film transistors," *Adv. Mater.*, vol. 17, no. 9, pp. 1141–1144, 2005.

[68] A. Strolio, J. Ward, J. M. Prausnitz, W. J. Parak, D. Zanchet, D. Gerion, D. Milliron, and A. P. Alivisatos, "Molecular weight, osmotic second viral coefficient, and extinction coefficient of collodial CdSe nanocrystals," *J.Phys.Chem.B*, vol. 106, pp. 5500–5505, 2002.

[69] C. A Leatherdale, W. K. Woo, F. V Mikulec, and M. G. Bawendi, "On the absorption cross section of CdSe nanocrystal quantum dots," *J. Phys. Chem. B*, vol. 106, pp. 7619–7622, 2002.

[70] K. Li, J. Pan, S. S. Feng, A. W. Wu, K. Y. Pu, Y. Liu, and B. Liu, "Generic strategy of preparing fluorescent conjugated-polymer-loaded poly(DL-lactide-co-glycolide) nanoparticles for targeted cell imaging," *Adv. Funct. Mater.*, vol. 19, no. 22, pp. 3535–3542, 2009.

[71] L. Lu, F. H. Rininsland, S. K. Wittenburg, K. E. Achyuthan, D. W. McBranch, and D. G. Whitten, "Biocidal activity of a light-absorbing fluorescent conjugated polyelectrolyte," *Langmuir*, vol. 21, no. 22, pp. 10154–10159, 2005.

[72] H. Chong, C. Nie, C. Zhu, Q. Yang, L. Liu, F. Lv, and S. Wang, "Conjugated polymer nanoparticles for light-activated anticancer and antibacterial activity with imaging capability," *Langmuir*, vol. 28, no. 4, pp. 2091–2098, 2012.

[73] A. T. Silva, A. Nguyen, C. Ye, J. Verchot, and J. H. Moon, "Conjugated polymer nanoparticles for effective siRNA delivery to tobacco BY-2

protoplasts," *BMC Plant Biol.*, vol. 10, no. 1, p. 291, 2010.

[74] X. Feng, F. Lv, L. Liu, Q. Yang, S. Wang, and G. C. Bazan, "A highly emissive conjugated polyelectrolyte vector for gene delivery and transfection," *Adv. Mater.*, vol. 24, no. 40, pp. 5428–5432, 2012.

[75] X. Feng, F. Lv, L. Liu, H. Tang, C. Xing, Q. Yang, and S. Wang, "Conjugated polymer nanoparticles for drug delivery and imaging," *ACS Appl. Mater. Interfaces*, vol. 2, no. 8, pp. 2429–2435, 2010.

[76] T. Kietzke, D. Neher, K. Landfester, R. Montenegro, R. Güntner, and U. Scherf, "Novel approaches to polymer blends based on polymer nanoparticles," *Nat. Mater.*, vol. 2, no. 6, pp. 408–12, 2003.

[77] T. Kietzke, D. Neher, M. Kumke, R. Montenegro, K. Landfester, and U. Scherf, "A nanoparticle approach to control the phase separation in polyfluorene photovoltaic devices," *Macromolecules*, vol. 37, no. 13, pp. 4882–4890, 2004.

[78] C. F. Huebner, R. D. Roeder, and S. H. Foulger, "Nanoparticle electroluminescence: Controlling emission color through förster resonance energy transfer in hybrid particles," *Adv. Funct. Mater.*, vol. 19, no. 22, pp. 3604–3609, 2009.

[79] J. Lee, I.-N. Kang, D.-H. Hwang, H.-K. Shim, S. C. Jeoung, and D. Kim, "Energy transfer in a blend of electroluminescent conjugated polymers," *Chem. Mater.*, vol. 4756, no. 20, pp. 1925–1929, 1996.

[80] I. O. Ozel, T. Ozel, H. V. Demir, and D. Tuncel, "Non-radiative resonance energy transfer in bi-polymer nanoparticles of fluorescent conjugated polymers," *Opt. Express*, vol. 18, no. 2, pp. 670–684, 2010.

[81] E.-J. Park, T. Erdem, V. Ibrahimova, S. Nizamoglu, H. V Demir, and D. Tuncel, "White-emitting conjugated polymer nanoparticles with cross-linked shell for mechanical stability and controllable photometric properties in color-conversion LED applications," *ACS Nano*, vol. 5, no. 4, pp. 2483–2492, 2011.

[82] T. Piok, S. Gamerith, C. Gadermaier, H. Plank, F. P. Wenzl, S. Patil, R. Montenegro, T. Kietzke, D. Neher, U. Scherf, K. Landfester, and E. J. W. List, "Organic light-emitting devices fabricated from semiconducting

nanospheres," *Adv. Mater.*, vol. 15, no. 10, pp. 800–804, 2003.

[83] I. O. Huyal, T. Ozel, U. Koldemir, S. Nizamoglu, D. Tuncel, and H. V. Demir, "White emitting polyfluorene functionalized with azide hybridized on near-UV light emitting diode for high color rendering index," *Opt. Express*, vol. 16, no. 2, pp. 1115–1124, 2008.

[84] I. O. Huyal, T. Ozel, D. Tuncel, and H. V. Demir, "Quantum efficiency enhancement in film by making nanoparticles of polyfluorene," *Opt. Express*, vol. 16, no. 17, pp. 13391–13397, 2008.

[85] H. V. Demir, S. Nizamoglu, T. Ozel, E. Mutlugun, I. O. Huyal, E. Sari, E. Holder, and N. Tian, "White light generation tuned by dual hybridization of nanocrystals and conjugated polymers," *New J. Phys.*, vol. 9, p. 362, 2007.

[86] A. Haugeneder, U. Lemmer, and U. Scherf, "Exciton dissociation dynamics in a conjugated polymer containing aggregate states," *Chem. Phys. Lett.*, vol. 351, pp. 354–358, 2002.

[87] J. M. Luther, J. Gao, M. T. Lloyd, O. E. Semonin, M. C. Beard, and A. J. Nozik, "Stability assessment on a 3% bilayer PbS/ZnO quantum dot heterojunction solar cell," *Adv. Mater.*, vol. 22, no. 33, pp. 3704–3707, 2010.

[88] H. Liu, J. Tang, I. J. Kramer, R. Debnath, G. I. Koleilat, X. Wang, A. Fisher, R. Li, L. Brzozowski, L. Levina, and E. H. Sargent, "Electron acceptor materials engineering in colloidal quantum dot solar cells," *Adv. Mater.*, vol. 23, no. 33, pp. 3832–3837, 2011.

[89] N. Jana, Y. Chen, and X. Peng, "Size-and shape-controlled magnetic (Cr, Mn, Fe, Co, Ni) oxide nanocrystals via a simple and general approach," *Chem. Mater.*, no. 21, pp. 3931–3935, 2004.

[90] D. L. Huber, "Synthesis, properties, and applications of iron nanoparticles," *Small*, vol. 1, no. 5, pp. 482–501, 2005.

[91] C. Kumar, Ed., *Nanomaterials for the Life Sciences Vol. 4: Magnetic Nanoparticles*. Weinheim: Wiley-VCH Verlag, 2009.

[92] D. Ling, N. Lee, and T. Hyeon, "Chemical synthesis and assembly of

uniformly sized iron oxide nanoparticles for medical applications," *Acc. Chem. Res.*, vol. 48, no. 5, pp. 1276–1285, 2015.

[93] B. H. Kim, N. Lee, H. Kim, K. An, Y. I. Park, Y. Choi, K. Shin, Y. Lee, S. G. Kwon, H. B. Na, J. G. Park, T. Y. Ahn, Y. W. Kim, W. K. Moon, S. H. Choi, and T. Hyeon, "Large-scale synthesis of uniform and extremely small-sized iron oxide nanoparticles for high-resolution T1 magnetic resonance imaging contrast agents," *J Am Chem Soc*, vol. 133, no. 32, pp. 12624–12631, 2011.

[94] J. Park, K. An, Y. Hwang, J. Park, J. I. N. Noh, J. A. E. Y. Kim, J. Park, and N. Hwang, "Ultra-large scale syntheses of monodisperse nanocrystals via a simple and inexpensive route," *Nature*, vol. 3, no. 12, pp. 1–13, 2004.

[95] D. Kim, N. Lee, M. Park, B. H. Kim, K. An, and T. Hyeon, "Synthesis of uniform ferrimagnetic magnetite nanocubes," *J. Am. Chem. Soc.*, vol. 131, no. 2, pp. 454–455, 2009.

[96] F. N. Sayed and V. Polshettiwar, "Facile and sustainable synthesis of shaped iron oxide nanoparticles: effect of iron precursor salts on the shapes of iron oxides," *Sci. Rep.*, vol. 5, p. 9733, 2015.

[97] S. Laurent, D. Forge, M. Port, A. Roch, C. Robic, L. Vander Elst, and R. N. Muller, "Magnetic iron oxide nanoparticles: Synthesis, stabilization, vectorization, physicochemical characterizations and biological applications," *Chem. Rev.*, vol. 108, no. 6, pp. 2064–2110, 2008.

[98] V. Valdiglesias, G. Kilic, C. Costa, N. Fernsndez-Bertolez, E. Pssaro, J. P. Teixeira, and B. Laffon, "Effects of iron oxide nanoparticles: Cytotoxicity, genotoxicity, developmental toxicity, and neurotoxicity," *Environ Mol Mutagen*, vol. 56, no. 2. pp. 125–148, 2015.

[99] A. K. Gupta and M. Gupta, "Synthesis and surface engineering of iron oxide nanoparticles for biomedical applications," *Biomaterials*, vol. 26, no. 18, pp. 3995–4021, 2005.

[100] Y. Matsumura and H. Maeda, "A new concept for macromolecular therapeutics in cnacer chemotherapy: mechanism of tumoritropic accumulatio of proteins and the antitumor agents Smancs," *Cancer Res.*, vol. 46, pp. 6387– 6392, 1986.

[101] N. Lee and T. Hyeon, "Designed synthesis of uniformly sized iron oxide nanoparticles for efficient magnetic resonance imaging contrast agents," *Chem. Soc. Rev.*, vol. 41, no. 7, pp. 2575–2589, 2012.

[102] J. Wan, X. Chen, Z. Wang, X. Yang, and Y. Qian, "A soft-template-assisted hydrothermal approach to single-crystal Fe3O4 nanorods," *J. Cryst. Growth*, vol. 276, no. 3–4, pp. 571–576, 2005.

[103] A. B. Chin and I. I. Yaacob, "Synthesis and characterization of magnetic iron oxide nanoparticles via w/o microemulsion and Massart's procedure," *J. Mater. Process. Technol.*, vol. 191, no. 1–3, pp. 235–237, 2007.

[104] C. Albornoz and S. E. Jacobo, "Preparation of a biocompatible magnetic film from an aqueous ferrofluid," *J. Magn. Magn. Mater.*, vol. 305, no. 1, pp. 12–15, 2006.

[105] J. Park, K. An, Y. Hwang, J.-G. Park, H.-J. Noh, J.-Y. Kim, J.-H. Park, N.-M. Hwang, and T. Hyeon, "Ultra-large-scale syntheses of monodisperse nanocrystals," *Nat. Mater.*, vol. 3, no. 12, pp. 891–895, 2004.

[106] R. Massart, "Preparation of aqueous magnetic liquids in alkaline and acidic media," *IEEE Trans. Magn.*, vol. 17, no. 2, pp. 1247–1248, 1981.

[107] E. H. Kim, H. S. Lee, B. K. Kwak, and B. K. Kim, "Synthesis of ferrofluid with magnetic nanoparticles by sonochemical method for MRI contrast agent," *J. Magn. Magn. Mater.*, vol. 289, pp. 328–330, 2005.

[108] G. Salazar-Alvarez, M. Muhammed, and A. A. Zagorodni, "Novel flow injection synthesis of iron oxide nanoparticles with narrow size distribution," *Chem. Eng. Sci.*, vol. 61, no. 14, pp. 4625–4633, 2006.

[109] S. Basak, D. R. Chen, and P. Biswas, "Electrospray of ionic precursor solutions to synthesize iron oxide nanoparticles: Modified scaling law," *Chem. Eng. Sci.*, vol. 62, no. 4, pp. 1263–1268, 2007.

[110] A. H. Lu, E. L. Salabas, and F. Schuth, "Magnetic nanoparticles: Synthesis, protection, functionalization, and application," *Angew. Chemie-Int. Ed.*, vol. 46, no. 8, pp. 1222–1244, 2007.

[111] A. S. Teja and P. Y. Koh, "Synthesis, properties, and applications of magnetic iron oxide nanoparticles," *Prog. Cryst. Growth Charact. Mater.*,

vol. 55, no. 1–2, pp. 22–45, 2009.

[112] W. Wu, Q. He, and C. Jiang, "Magnetic iron oxide nanoparticles: Synthesis and surface functionalization strategies," *Nanoscale Res. Lett.*, vol. 3, no. 11, pp. 397–415, 2008.

[113] V. Pillai, P. Kumar, M. J. Hou, P. Ayyub, and D. O. Shah, "Preparation of nanoparticles of silver halides, superconductors and magnetic materials using water-in-oil microemulsions as nano-reactors," *Adv. Colloid Interface Sci.*, vol. 55, pp. 241–269, 1995.

[114] J. A. Lopez Perez, M. A. Lopez Quintela, J. Mira, J. Rivas, and S. W. Charles, "Advances in the preparation of magnetic nanoparticles by the microemulsion method," *J. Phys. Chem. B*, vol. 101, no. 41, pp. 8045–8047, 1997.

[115] Y. Deng, L. Wang, W. Yang, S. Fu, and A. Elaïssari, "Preparation of magnetic polymeric particles via inverse microemulsion polymerization process," *J. Magn. Magn. Mater.*, vol. 257, no. 1, pp. 69–78, 2003.

[116] Z. Z. Xu, C. C. Wang, W. L. Yang, Y. H. Deng, and S. K. Fu, "Encapsulation of nanosized magnetic iron oxide by polyacrylamide via inverse miniemulsion polymerization," *J. Magn. Magn. Mater.*, vol. 277, no. 1–2, pp. 136–143, 2004.

[117] I. Capek, "Preparation of metal nanoparticles in water-in-oil (w/o) microemulsions," *Adv. Colloid Interface Sci.*, vol. 110, no. 1–2, pp. 49–74, 2004.

[118] J. Rockenberger, E. Scher, and A. Alivisatos, "A new nonhydrolytic single-precursor approach to surfactant-capped nanocrystals of transition metal oxides," *J. Am. Chem. Soc.*, vol. 121, no. 49, pp. 11595-596, 1999.

[119] T. Hyeon, S. S. Lee, J. Park, "Synthesis of highly crystalline and monodisperse maghemite nanoystallites without a size-selection process," *J. Am. Chem. Soc.*, vol. 123, no. 8, pp. 12789–12801, 2001.

[120] A. Nel, T. Xia, L. Mädler, and N. Li, "Toxic potential of materials at the nanolevel.," *Science*, vol. 311, pp. 622–627, 2006.

[121] P. B. Santhosh and N. P. Ulrih, "Multifunctional superparamagnetic iron

oxide nanoparticles: Promising tools in cancer theranostics," *Cancer Lett.*, vol. 336, no. 1, pp. 8–17, 2013.

[122] N. Lee, D. Yoo, D. Ling, M. H. Cho, T. Hyeon, and J. Cheon, "Iron oxide based nanoparticles for multimodal imaging and magnetoresponsive therapy," *Chem. Rev.*, vol. 115, no. 19, pp. 10637–10689, 2015.

[123] E. J. Van Den Bos, A. Wagner, H. Mahrholdt, R. B. Thompson, Y. Morimoto, B. S. Sutton, R. M. Judd, and D. A. Taylor, "Improved efficacy of stem cell labeling for magnetic resonance imaging studies by the use of cationic liposomes," *Cell Transplant.*, vol. 12, no. 7, pp. 743–756, 2003.

[124] A. Stroh, C. Zimmer, C. Gutzeit, M. Jakstadt, F. Marschinke, T. Jung, H. Pilgrimm, and T. Grune, "Iron oxide particles for molecular magnetic resonance imaging cause transient oxidative stress in rat macrophages," *Free Radic. Biol. Med.*, vol. 36, no. 8, pp. 976–984, 2004.

[125] O. Veiseh, J. W. Gunn, and M. Zhang, "Design and fabrication of magnetic nanoparticles for targeted drug delivery and imaging," *Adv. Drug Deliv. Rev.*, vol. 62, no. 3, pp. 284–304, 2010.

[126] Y. X. J. Wang, S. M. Hussain, and G. P. Krestin, "Superparamagnetic iron oxide contrast agents: Physicochemical characteristics and applications in MR imaging," *Eur. Radiol.*, vol. 11, no. 11, pp. 2319–2331, 2001.

[127] A. Bjørnerud and L. Johansson, "The utility of superparamagnetic contrast agents in MRI: Theoretical consideration and applications in the cardiovascular system," *NMR Biomed.*, vol. 17, no. 7, pp. 465–477, 2004.

[128] M. Yu, S. Huang, K. J. Yu, and A. M. Clyne, "Dextran and polymer polyethylene glycol (PEG) coating reduce both 5 and 30 nm iron oxide nanoparticle cytotoxicity in 2D and 3D cell culture," *Int. J. Mol. Sci.*, vol. 13, no. 5, pp. 5554–5570, 2012.

[129] R. Weissleder, H. C. Cheng, A. Bogdanova, and A. Bogdanov, "Magnetically labeled cells can be detected by MR imaging," *J. Magn. Reson. Imaging*, vol. 7, no. 1, pp. 258–263, 1997.

[130] Y. Piao, A. Burns, J. Kim, U. Wiesner, and T. Hyeon, "Designed fabrication of silica-based nanostructured particle systems for

nanomedicine applications," *Adv. Funct. Mater.*, vol. 18, no. 23, pp. 3745–3758, 2008.

[131] M. Longmire, P. L. Choyke, and H. Kobayashi, "Clearance properties of nano-sized particles and molecules as imaging agents: Considerations and caveats," *Nanomedicine*, vol. 3, no. 5, pp. 703–717, 2008.

[132] X. He, H. Nie, K. Wang, W. Tan, X. Wu, and P. Zhang, "In vivo study of biodistribution and urinary excretion of surface-modified silica nanoparticles," vol. 80, no. 24, pp. 9597–9603, 2008.

[133] C. W. Lee, K. T. Huang, P. K. Wei, and Y. D. Yao, "Conjugation of γ-Fe2O3 nanoparticles with single strand oligonucleotides," *J. Magn. Magn. Mater.*, vol. 304, no. 1, pp. 412–414, 2006.

[134] G. Palui, F. Aldeek, W. Wang, and H. Mattoussi, "Strategies for interfacing inorganic nanocrystals with biological systems based on polymer-coating," *Chem. Soc. Rev.*, vol. 44, pp. 193–227, 2014.

[135] V. K. Sharma, A. Alipour, Z. Sorsn-Erdem, Y. Kelestemur, Z. G. Aykut, and H. V Demir, "Fluorescent heterodoped nanotetrapods as synergistically enhancing positive and negative magnetic resonance imaging contrast agents," *ACS Appl. Mater. Interfaces*, vol. 8, no. 19, pp. 12352-12359, 2016.

[136] C. Xu, K. Xu, H. Gu, R. Zheng, H. Liu, X. Zhang, Z. Guo, and B. Xu, "Dopamine as a robust anchor to immobilize functional molecules on the iron oxide shell of magnetic nanoparticles," *J. Am. Chem. Soc.*, vol. 126, no. 32, pp. 9938–9939, 2004.

[137] B. L. Frankamp, N. O. Fischer, R. Hong, S. Srivastava, and V. M. Rotello, "Surface modification using cubic silsesquioxane ligands. facile synthesis of water-soluble metal oxide nanoparticles," *Chem. Mater.*, vol. 18, no. 4, pp. 956–959, 2006.

[138] M. S. AlSalhi, J. Alam, L. A. Dass, and M. Raja, "Recent advances in conjugated polymers for light emitting devices," *Int. J. Mol. Sci.*, vol. 12, no. 12, pp. 2036–2054, 2011.

[139] C. Jiang, W. Yang, J. Peng, S. Xiao, and Y. Cao, "High-efficiency, saturated red-phosphorescent polymer light-emitting diodes based on

conjugated and non-conjugated polymers doped with an Ir complex," *Adv. Mater.*, vol. 16, no. 6, pp. 537–541, 2004.

[140] M. Kuik, G.-J. A. H. Wetzelaer, H. T. Nicolai, N. I. Craciun, D. M. De Leeuw, and P. W. M. Blom, "25th anniversary article: Charge transport and recombination in polymer light-emitting diodes," *Adv. Mater.*, vol. 26, no. 4, pp. 512–531, 2014.

[141] W. J. E. Beek, M. M. Wienk, and R. A. J. Janssen, "Efficient hybrid solar cells from zinc oxide nanoparticles and a conjugated polymer," *Adv. Mater.*, vol. 16, no. 12, pp. 1009–1013, 2004.

[142] G. Li, R. Zhu, and Y. Yang, "Polymer solar cells," *Nat. Photonics*, vol. 6, no. 3, pp. 153–161, 2012.

[143] Y. Liang, Z. Xu, J. Xia, S. T. Tsai, Y. Wu, G. Li, C. Ray, and L. Yu, "For the bright future-bulk heterojunction polymer solar cells with power conversion efficiency of 7.4%," *Adv. Mater.*, vol. 22, no. 20, pp. 135–138, 2010.

[144] H.-Y. Liu, P.-J. Wu, S.-Y. Kuo, C.-P. Chen, E.-H. Chang, C.-Y. Wu, and Y.-H. Chan, "Quinoxaline-based polymer dots with ultrabright red to near-infrared fluorescence for in vivo biological imaging," *J. Am. Chem. Soc.*, vol. 137, no. 32, pp. 10420–10429, 2015.

[145] C. Wu, C. Szymanski, and J. McNeill, "Preparation and encapsulation of highly fluorescent conjugated polymer nanoparticles," *Langmuir*, vol. 22, no. 7, pp. 2956–60, 2006.

[146] Y. Park and R. C. Advincula, "Hybrid semiconductor nanoparticles: π-conjugated ligands and nanostructured films," *Chem. Mater.*, vol. 23, no. 19, pp. 4273–4294, 2011.

[147] X. Wu, H. Li, Y. Xu, B. Xu, H. Tong, and L. Wang, "Thin film fabricated from solution-dispersible porous hyperbranched conjugated polymer nanoparticles without surfactants," *Nanoscale*, vol. 6, no. 4, pp. 2375–80, 2014.

[148] J. Gierschner, H.-J. Egelhaaf, D. Oelkrug, and K. Müllen, "Electronic deactivation and energy transfer in doped oligophenylenevinylene nanoparticles," *J. Fluoresc.*, vol. 8, no. 1, pp. 37–44, 1998.

[149] I. Martini, A. Smith, and B. Schwartz, "Exciton-exciton annihilation and the production of interchain species in conjugated polymer films: Comparing the ultrafast stimulated emission and photoluminescence dynamics of MEH-PPV," *Phys. Rev. B*, vol. 69, p. 035204, 2004.

[150] J. Pennakalathil, E. Jahja, E. S. Ozdemir, O. Konu, and D. Tuncel, "Red emitting, cucurbituril-capped, pH-responsive conjugated oligomer-based nanoparticles for drug delivery and cellular imaging," *Biomacromolecules*, vol. 15, no. 9, pp. 3366–74, 2014.

[151] I. Fischer, A. Kaeser, M. a M. Peters-Gumbs, and A. P. H. J. Schenning, "Fluorescent π-conjugated polymer dots versus self-assembled small-molecule nanoparticles: What's the difference?," *Chem. Eur. J.*, vol. 19, pp. 10928–10934, 2013.

[152] Z.-M. Dang, Y. Gao, H.-P. Xu, and J. Bai, "Fabrication and characteristics of organic semiconductor nanoparticles of copper phthalocyanine oligomers," *J. Colloid Interface Sci.*, vol. 322, pp. 491–496, 2008.

[153] X. Liu, X. He, T. Jiu, M. Yuan, J. Xu, J. Lv, H. Liu, and Y. Li, "Controlled aggregation of functionalized gold nanoparticles with a novel conjugated oligomer," *ChemPhysChem*, vol. 8, no. 6, pp. 906–912, 2007.

[154] S. Kalytchuk, O. Zhovtiuk, and A. L. Rogach, "Sodium chloride protected CdTe quantum dot based solid-state luminophores with high color quality and fluorescence efficiency," *Appl. Phys. Lett.*, vol. 103, no. 10, p. 103105, 2013.

[155] M. Adam, T. Erdem, G. M. Stachowski, Z. Soran-Erdem, J. Lox, C. Bauer, J. Poppe, H. V. Demir, N. Gaponik, and A. Eychmueller, "Implementation of high-quality warm-white light-emitting diodes by a model-experimental feedback approach using quantum dot-salt mixed crystals," *ACS Appl. Mater. Interfaces*, no. 7, pp. 23364—23371, 2015.

[156] J. C. de Mello, H. F. Wittmannn, and R. H. Friend, "An improved experimental determination of external photoluminescence quantum efficiency," *Adv. Mater.*, vol. 9, no. 3, p. 230, 1997.

[157] OSRAM OptoSemiconductors, "LED Fundamentals. Thermal Characteristics of LEDs," 2011. [Online]. Available: http://ledlight.osram-

os.com/wp-content/uploads/2013/01/OSRAM-OS_LED-FUNDAMENTALS_Thermal-Characteristics-of-LEDs_v2_08-16-11_SCRIPT.pdf. [Accessed: 07-Jan-2016].

[158] Z. Soran-Erdem, T. Erdem, P. L. Hernandez-Martinez, M. Z. Akgul, N. Gaponik, and H. V. Demir, "Macrocrystals of colloidal quantum dots in anthracene: Exciton transfer and polarized emission," *J. Phys. Chem. Lett.*, vol. 6, no. 9, pp. 1767–1772, 2015.

[159] H. V. Demir, S. Nizamoglu, T. Erdem, E. Mutlugun, N. Gaponik, and A. Eychmuller, "Quantum dot integrated LEDs using photonic and excitonic color conversion," *Nano Today*, vol. 6, no. 6. pp. 632–647, 2011.

[160] J. Y. Kim, O. Voznyy, D. Zhitomirsky, and E. H. Sargent, "25th anniversary article: Colloidal quantum dot materials and devices: A quarter-century of advances," *Advanced Materials*, vol. 25, no. 36. pp. 4986–5010, 2013.

[161] Y. Shirasaki, G. J. Supran, M. G. Bawendi, and V. Bulović, "Emergence of colloidal quantum-dot light-emitting technologies," *Nat. Photonics*, vol. 7, no. 1, pp. 13–23, 2013.

[162] E. Mutlugun, B. Guzelturk, A. P. Abiyasa, Y. Gao, X. W. Sun, and H. V. Demir, "Colloidal quantum dot light-emitting diodes employing phosphorescent small organic molecules as efficient exciton harvesters," *J. Phys. Chem. Lett.*, vol. 5, no. 16, pp. 2802–2807, 2014.

[163] B. Guzelturk, Y. Kelestemur, M. Z. Akgul, V. K. Sharma, and H. V. Demir, "Ultralow threshold one-photon- and two-photon-pumped optical gain media of blue-emitting colloidal quantum dot films," *J. Phys. Chem. Lett.*, vol. 5, no. 13, pp. 2214–2218, 2014.

[164] V. Sukhovatkin, S. Hinds, L. Brzozowski, and E. H. Sargent, "Colloidal quantum-dot photodetectors exploiting multiexciton generation," *Science*, vol. 324, no. 5934, pp. 1542–1544, 2009.

[165] P. V. Kamat, "Quantum dot solar cells. Semiconductor nanocrystals as light harvesters," *J. Phys. Chem. C*, vol. 112, no. 48, pp. 18737–18753, 2008.

[166] B. Guzelturk, P. L. H. Martinez, Q. Zhang, Q. Xiong, H. Sun, X. W. Sun,

A. O. Govorov, and H. V. Demir, "Excitonics of semiconductor quantum dots and wires for lighting and displays," *Laser and Photonics Reviews*, vol. 8, no. 1. pp. 73–93, 2014.

[167] E. Mutlugun, O. Samarskaya, T. Ozel, N. Cicek, N. Gaponik, A. Eychmüller, and H. V. Demir, "Highly efficient nonradiative energy transfer mediated light harvesting in water using aqueous CdTe quantum dot antennas," *Opt. Express*, vol. 18, no. 10, pp. 10720–30, 2010.

[168] A. Yeltik, B. Guzelturk, P. L. Hernandez-Martinez, A. O. Govorov, and H. V. Demir, "Phonon-assisted exciton transfer into silicon using nanoemitters: The role of phonons and temperature effects in forster resonance energy transfer," *ACS Nano*, vol. 7, no. 12, pp. 10492–10501, 2013.

[169] N. Cicek, S. Nizamoglu, T. Ozel, E. Mutlugun, D. U. Karatay, V. Lesnyak, T. Otto, N. Gaponik, A. Eychmuller, and H. V. Demir, "Structural tuning of color chromaticity through nonradiative energy transfer by interspacing CdTe nanocrystal monolayers," *Appl. Phys. Lett.*, vol. 94, no. 6, 2009.

[170] A. L. Briseno, S. C. B. Mannsfeld, M. M. Ling, S. Liu, R. J. Tseng, C. Reese, M. E. Roberts, Y. Yang, F. Wudl, and Z. Bao, "Patterning organic single-crystal transistor arrays," *Nature*, vol. 444, no. 7121, pp. 913–917, 2006.

[171] P. Raghunath, M. A. Reddy, C. Gouri, K. Bhanuprakash, and V. J. Rao, "Electronic properties of anthracene derivatives for blue light emitting electroluminescent layers in organic light emitting diodes: A density functional theory study," *J. Phys. Chem. A*, vol. 110, no. 3, pp. 1152–1162, 2006.

[172] S. Tao, Y. Zhou, C.-S. Lee, S.-T. Lee, D. Huang, and X. Zhang, "Highly efficient nondoped blue organic light-emitting diodes based on anthracene-triphenylamine derivatives," *J. Phys. Chem. C*, vol. 112, no. 37, pp. 14603–14606, 2008.

[173] H. Benmansour, T. Shioya, Y. Sato, and G. C. Bazan, "Anthracene-containing binaphthol chromophores for light-emitting diode (LED) fabrication," *Adv. Funct. Mater.*, vol. 13, no. 11, pp. 883–886, 2003.

[174] A. L. Briseno, J. Aizenberg, Y. J. Han, R. A. Penkala, H. Moon, A. J.

Lovinger, C. Kloc, and Z. Bao, "Patterned growth of large oriented organic semiconductor single crystals on self-assembled monolayer templates," *J. Am. Chem. Soc.*, vol. 127, no. 35, pp. 12164–12165, 2005.

[175] J. R. Lakowicz, *Principles of Fluorescence Spectroscopy Principles of Fluorescence Spectroscopy*. 2006.

[176] J. N. Sherwood and S. J. Thomson, "Growth of single crystals of anthracene," *J. Sci. Instrum.*, vol. 37, no. 7, p. 242, 1960.

[177] C. Uran, T. Erdem, B. Guzelturk, N. K. Perkgöz, S. Jun, E. Jang, and H. V. Demir, "Highly polarized light emission by isotropic quantum dots integrated with magnetically aligned segmented nanowires," *Appl. Phys. Lett.*, vol. 105, no. 14, p. 141116, 2014.

[178] F. R. Lipsett, "On the production of single crystals of naphthalene and anthracene," *Can. J. Phys.*, vol. 35, no. 3, pp. 284–298, 1957.

[179] S. Kalytchuk, O. Zhovtiuk, A. L. Rogach, "Sodium chloride protected CdTe quantum dot based solid-state luminophores with high color quality and fluorescence efficiency," *Appl. Phys. Lett.*, vol. 103, no. 3, pp. 817–818, 2013.

[180] S. Jo, H. Yoshikawa, A. Fujii, and M. Takenaga, "Surface morphologies of anthracene single crystals grown from vapor phase," *Appl. Surf. Sci.*, vol. 252, no. 10, pp. 3514–3519, 2006.

[181] H. Wu and J. Zhou, "Optical properties of anthracene single crystals grown by a simple solution technique," *Int. J. Mod. Phys. B*, vol. 27, no. 8, p. 1350022, 2013.

[182] R. Koeppe and N. S. Sariciftci, "Photoinduced charge and energy transfer involving fullerene derivatives," *Photochem. Photobiol. Sci.*, vol. 5, no. 12, pp. 1122–31, 2006.

[183] S. Nizamoglu, E. Sari, J. H. Baek, I. H. Lee, and H. V. Demir, "Nonradiative resonance energy transfer directed from colloidal CdSe/ZnS quantum dots to epitaxial ingan/gan quantum wells for solar cells," *Phys. Status Solidi - Rapid Res. Lett.*, vol. 4, no. 7, pp. 178–180, 2010.

[184] S. Lindhoud, A. H. Westphal, C. P. M. Van Mierlo, A. J. W. G. Visser,

and J. W. Borst, "Rise-time of FRET-acceptor fluorescence tracks protein folding," *Int. J. Mol. Sci.*, vol. 15, no. 12, pp. 23836–23850, 2014.

[185] I. Nakada, "The optical properties of anthracene single crystals," *J. Phys. Soc. Japan*, vol. 17, no. 1, pp. 113–118, 1962.

[186] M. A. Lasheen and I.H. Ibrahim, "Optical Anisotropies of Some Organic Molecules," *Acta Cryst.*, A31, pp. 136–141, 1975.

[187] V. K. Sharma, A. Alipour, Z. Soran-Erdem, Z. G. Aykut, and H. V. Demir, "Highly monodisperse low-magnetization magnetite nanocubes as simultaneous T_1–T_2 MRI contrast agents," *Nanoscale*, vol. 7, no. 23, pp. 10519–10526, 2015.

[188] M. Srinivas, E. H. J. G. Aarntzen, J. W. M. Bulte, W. J. Oyen, A. Heerschap, I. J. M. de Vries, and C. G. Figdor, "Imaging of cellular therapies," *Adv. Drug Deliv. Rev.*, vol. 62, no. 11, pp. 1080–1093, 2010.

[189] Y. Piao, J. Kim, H. Bin Na, D. Kim, J. S. Baek, M. K. Ko, J. H. Lee, M. Shokouhimehr, and T. Hyeon, "Wrap-bake-peel process for nanostructural transformation from [beta]-FeOOH nanorods to biocompatible iron oxide nanocapsules," *Nat Mater*, vol. 7, no. 3, pp. 242–247, 2008.

[190] E. I. Galanzha, E. V Shashkov, T. Kelly, J.-W. Kim, L. Yang, and V. P. Zharov, "In vivo magnetic enrichment and multiplex photoacoustic detection of circulating tumour cells," *Nat Nano*, vol. 4, no. 12, pp. 855–860, Dec. 2009.

[191] H. Bin Na, I. C. Song, and T. Hyeon, "Inorganic nanoparticles for MRI contrast agents," *Adv. Mater.*, vol. 21, no. 21, pp. 2133–2148, 2009.

[192] Scott A. Huettel; Allen W. Song; Gregory McCarthy, A. Huettel, Scott; Song, C. F. Beckmann, S. M. Smith, S. A. Huettel, A. W. Song, and G. McCarthy, *Functional Magnetic Resonance Imaging*, vol. 23, no. 2. 2004.

[193] Y.-X. J. Wang, "Superparamagnetic iron oxide based MRI contrast agents: Current status of clinical application," *Quant. Imaging Med. Surg.*, vol. 1, no. 1, pp. 35–40, 2011.

[194] D. Pan, A. Schmieder, S. Wickline, and G. Lanza, "Manganese-based MRI contrast agents: past, present and future," *Tetrahedron*, vol. 67, no. 44,

pp. 8431–8444, 2011.

[195] Peter Caravan, Jeffrey J. Ellison, Thomas J. McMurry, and Randall B. Lauffer, "Gadolinium(III) Chelates as MRI Contrast Agents: Structure, Dynamics, and Applications," *Chem. Rev.*, vol. 99, no. 9, pp. 2293–2352, 1999.

[196] D. Choi, A. Han, J. P. Park, J. K. Kim, J. H. Lee, T. H. Kim, and S. W. Kim, "Fabrication of MnxFe1-xO colloidal solid solution as a dual magnetic-resonance-contrast agent," *Small*, vol. 5, no. 5, pp. 571–573, 2009.

[197] W. Chen, F. Lu, C.-C. V Chen, K.-C. Mo, Y. Hung, Z.-X. Guo, C.-H. Lin, M.-H. Lin, Y.-H. Lin, C. Chang, and C.-Y. Mou, "Manganese-enhanced MRI of rat brain based on slow cerebral delivery of manganese(II) with silica-encapsulated MnxFe1–xO nanoparticles," *NMR Biomed.*, vol. 26, no. 9, pp. 1176–1185, 2013.

[198] K. H. Bae, Y. B. Kim, Y. Lee, J. Hwang, H. Park, and T. G. Park, "Bioinspired Synthesis and Characterization of Gadolinium-Labeled Magnetite Nanoparticles for Dual Contrast T1- and T2-Weighted Magnetic Resonance Imaging," *Bioconjug. Chem.*, vol. 21, no. 3, pp. 505–512, 2010.

[199] F. Hu, Q. Jia, Y. Li, and M. Gao, "Facile synthesis of ultrasmall PEGylated iron oxide nanoparticles for dual-contrast T1- and T2-weighted magnetic resonance imaging," *Nanotechnology*, vol. 22, no. 24, p. 245604, 2011.

[200] G. Huang, H. Li, J. Chen, Z. Zhao, L. Yang, X. Chi, Z. Chen, X. Wang, and J. Gao, "Tunable T1 and T2 contrast abilities of manganese-engineered iron oxide nanoparticles through size control," *Nanoscale*, vol. 6, pp. 10404–12, 2014.

[201] J. Choi, J.-H. Lee, T.-H. Shin, H.-T. Song, E. Y. Kim, and J. Cheon, "Self-Confirming 'AND' Logic Nanoparticles for Fault-Free MRI," *J. Am. Chem. Soc.*, vol. 132, no. 32, pp. 11015–11017, 2010.

[202] M. Cho, R. Sethi, J. S. A. Narayanan, S. S. Lee, D. N. Benoit, N. Taheri, P. Decuzzi, and V. L. Colvin, "Gadolinium oxide nanoplates with high longitudinal relaxivity for magnetic resonance imaging," *Nanoscale*, vol.

6, no. 22, pp. 13637–45, 2014.

[203] G. Huang, X. Zhu, H. Li, L. Wang, X. Chi, J. Chen, X. Wang, Z. Chen, and J. Gao, "Facile integration of multiple magnetite nanoparticles for theranostics combining efficient MRI and thermal therapy," *Nanoscale*, vol. 7, no. 6, pp. 2667–2675, 2015.

[204] E. A. Neuwelt, P. Várallyay, A. G. Bagó, L. L. Muldoon, G. Nesbit, and R. Nixon, "Imaging of iron oxide nanoparticles by MR and light microscopy in patients with malignant brain tumours," *Neuropathol. Appl. Neurobiol.*, vol. 30, no. 5, pp. 456–471, 2004.

[205] A. H. Kaim, T. Wischer, T. O'Reilly, G. Jundt, J. Fröhlich, G. K. von Schulthess, and P. R. Allegrini, "MR imaging with ultrasmall superparamagnetic iron oxide particles in experimental soft-tissue infections in rats," *Radiology*, vol. 225, no. 3, pp. 808–14, 2002.

[206] K. H. Bae, M. Park, M. J. Do, N. Lee, J. H. Ryu, G. W. Kim, C. Kim, T. G. Park, and T. Hyeon, "Chitosan Oligosaccharide-Stabilized Ferrimagnetic Iron Oxide Nanocubes for Magnetically Modulated Cancer Hyperthermia," *ACS Nano*, vol. 6, no. 6, pp. 5266–5273, 2012.

[207] N. Lee, Y. Choi, Y. Lee, M. Park, W. K. Moon, S. H. Choi, and T. Hyeon, "Water-dispersible ferrimagnetic iron oxide nanocubes with extremely high r2 relaxivity for highly sensitive in vivo MRI of tumors," *Nano Lett.*, vol. 12, no. 6, pp. 3127–3131, 2012.

[208] B. H. Kim, N. Lee, H. Kim, K. An, Y. Il Park, Y. Choi, K. Shin, Y. Lee, S. G. Kwon, H. Bin Na, J.-G. Park, T.-Y. Ahn, Y.-W. Kim, W. K. Moon, S. H. Choi, and T. Hyeon, "Large-scale synthesis of uniform and extremely small-sized iron oxide nanoparticles for high-resolution T1 magnetic resonance imaging contrast agents," *J. Am. Chem. Soc.*, vol. 133, no. 32, pp. 12624–12631, 2011.

[209] G. Zhen, B. W. Muir, B. A. Moffat, P. Harbour, K. S. Murray, B. Moubaraki, K. Suzuki, I. Madsen, N. Agron-Olshina, L. Waddington, P. Mulvaney, and P. G. Hartley, "Comparative Study of the Magnetic Behavior of Spherical and Cubic Superparamagnetic Iron Oxide Nanoparticles," *J. Phys. Chem. C*, vol. 115, no. 2, pp. 327–334, 2011.

[210] Z. Zhou, Z. Zhao, H. Zhang, Z. Wang, X. Chen, R. Wang, Z. Chen, and

J. Gao, "Interplay between longitudinal and transverse contrasts in Fe3O4 nanoplates with (111) exposed surfaces," *ACS Nano*, vol. 8, no. 8, pp. 7976–7985, 2014.

[211] J. Huang, L. Bu, J. Xie, K. Chen, Z. Cheng, X. Li, and X. Chen, "Effects of nanoparticle size on cellular uptake and liver MRI with polyvinylpyrrolidone-coated iron oxide nanoparticles," *ACS Nano*, vol. 4, no. 12, pp. 7151–7160, 2010.

[212] A. Shavel, B. Rodríguez-González, M. Spasova, M. Farle, and L. M. Liz-Marzán, "Synthesis and characterization of iron/iron oxide core/shell nanocubes," *Adv. Funct. Mater.*, vol. 17, no. 18, pp. 3870–3876, 2007.

[213] X. Liang, X. Wang, J. Zhuang, Y. Chen, D. Wang, and Y. Li, "Synthesis of nearly monodisperse iron oxide and oxyhydroxide nanocrystals," *Adv. Funct. Mater.*, vol. 16, no. 14, pp. 1805–1813, 2006.

[214] A. A. Khaleel, "Nanostructured pure γ-Fe2O3 via forced precipitation in an organic solvent," *Chem. Eur. J.*, vol. 10, no. 4, pp. 925–932, 2004.

[215] Y. W. Jun, Y. M. Huh, J. Choi, J. H. Lee, H. T. Song, S. Kim, S. Yoon, K. S. Kim, J. S. Shin, J. S. Suh, and J. Cheon, "Nanoscale size effect of magnetic nanocrystals and their utilization for cancer diagnosis via magnetic resonance imaging," *J. Am. Chem. Soc.*, vol. 127, no. 16, pp. 5732–5733, 2005.

[216] F. Hu, Z. Li, C. Tu, and M. Gao, "Preparation of magnetite nanocrystals with surface reactive moieties by one-pot reaction," *J. Colloid Interface Sci.*, vol. 311, no. 2, p. 469—474, 2007.

[217] D. Caruntu, G. Caruntu, and C. J. O'Connor, "Magnetic properties of variable-sized Fe3O4 nanoparticles synthesized from non-aqueous homogeneous solutions of polyols," *J. Phys. D. Appl. Phys.*, vol. 40, no. 19, pp. 5801–5809, 2007.

[218] M. P. Morales, S. Veintemillas-Verdaguer, M. I. Montero, and C. J. Serna, A. Roig, Ll. Casas, B. Martínez, and and F. Sandiumenge, "Surface and Internal Spin Canting in γ-Fe2O3 Nanoparticles," *Chem. Mater.*, vol. 11, no. 11, pp. 3058–3064, 1999.

[219] G. F. Goya, T. S. Berquó, F. C. Fonseca, and M. P. Morales, "Static and

dynamic magnetic properties of spherical magnetite nanoparticles," *J. Appl. Phys.*, vol. 94, no. 5, 2003.

[220] L. Suber, P. Imperatori, G. Ausanio, F. Fabbri, and H. Hofmeister, "Synthesis, morphology, and magnetic characterization of iron oxide nanowires and nanotubes," *J. Phys. Chem. B*, vol. 109, no. 15, pp. 7103–7109, 2005.

[221] E. M. Hutter, F. Pietra, R. J. A. van Dijk-Moes, D. Mitoraj, J. D. Meeldijk, C. de Mello Donegá, and D. Vanmaekelbergh, "Method to incorporate anisotropic semiconductor nanocrystals of all shapes in an ultrathin and uniform silica shell," *Chem. Mater.*, vol. 26, no. 5, pp. 1905–1911, 2014.

[222] E. A. Weitz, C. Lewandowski, E. D. Smolensky, M. Marjańska, and V. C. Pierre, "A magnetoplasmonic imaging agent for copper(I) with dual response by MRI and dark field microscopy," *ACS Nano*, vol. 7, no. 7, pp. 5842–5849, 2013.

[223] L. Zeng, W. Ren, J. Zheng, and A. Wu, "Ultrasmall water-soluble metal-iron oxide nanoparticles as T1-weighted contrast agents for magnetic resonance imaging," *Phys Chem Chem Phys.*, vol. 14, no. 8, pp. 2631–2636, 2012.

[224] L. Wortmann, S. Ilyas, D. Niznansky, M. Valldor, K. Arroub, N. Berger, K. Rahme, J. Holmes, and S. Mathur, "Bioconjugated iron oxide nanocubes: Synthesis, functionalization, and vectorization," *ACS Appl. Mater. Interfaces*, vol. 6, no. 19, pp. 16631–16642, 2014.

[225] V. Mamaeva, C. Sahlgren, and M. Lindén, "Mesoporous silica nanoparticles in medicine—Recent advances," *Adv. Drug Deliv. Rev.*, vol. 65, no. 5, pp. 689–702, 2013.

[226] J. Lu, M. Liong, Z. Li, J. I. Zink, and F. Tamanoi, "Biocompatibility, biodistribution, and drug-delivery efficiency of mesoporous silica nanoparticles for cancer therapy in animals," *Small*, vol. 6, no. 16, pp. 1794–1805, 2010.

[227] E. Taboada, E. Rodríguez, A. Roig, J. Oró, A. Roch, and R. N. Muller, "Relaxometric and magnetic characterization of ultrasmall iron oxide nanoparticles with high magnetization. Evaluation as potential T1

magnetic resonance imaging contrast agents for molecular imaging," *Langmuir*, vol. 23, no. 14, pp. 4583–4588, 2007.

[228] Z. Zhao, Z. Zhou, J. Bao, Z. Wang, J. Hu, X. Chi, K. Ni, R. Wang, X. Chen, Z. Chen, and J. Gao, "Octapod iron oxide nanoparticles as high-performance T_2 contrast agents for magnetic resonance imaging," *Nat. Commun.*, vol. 4, p. 2266, 2013.

[229] A. Deo, M. Fogel, and S. E. Cowper, "Nephrogenic systemic fibrosis: A population study examining the relationship of disease development to gadolinium exposure," *Clin. J. Am. Soc. Nephrol.*, vol. 2, no. 2, pp. 264–267, 2007.

[230] U. I. Tromsdorf, O. T. Bruns, S. C. Salmen, U. Beisiegel, and H. Weller, "A highly effective, nontoxic T1 MR contrast agent based on ultrasmall PEGylated iron oxide nanoparticles," *Nano Lett.*, vol. 9, no. 12, pp. 4434–4440, 2009.

[231] P. Drake, H.-J. Cho, P.-S. Shih, C.-H. Kao, K.-F. Lee, C.-H. Kuo, X.-Z. Lin, and Y.-J. Lin, "Gd-doped iron-oxide nanoparticles for tumour therapy via magnetic field hyperthermia," *J. Mater. Chem.*, vol. 17, no. 46, p. 4914, 2007.

[232] R. Chalasani and S. Vasudevan, "Form, Content, and Magnetism in Iron Oxide Nanocrystals," *J. Phys. Chem. C*, vol. 115, no. 37, pp. 18088–18093, 2011.

[233] F. Jiang, X. Li, Y. Zhu, and Z. Tang, "Synthesis and magnetic characterizations of uniform iron oxide nanoparticles," *Phys. B Condens. Matter*, vol. 443, pp. 1–5, 2014.

[234] S. Sheng-Nan, W. Chao, Z. Zan-Zan, H. Yang-Long, S. S. Venkatraman, and X. Zhi-Chuan, "Magnetic iron oxide nanoparticles: Synthesis and surface coating techniques for biomedical applications," *Chin. Phys. B*, vol. 2346, no. 3, pp. 81–16, 2014.

[235] L. Bronstein, X. Huang, J. Retrum, A. Schmucker, M. Pink, B. D. Stein, and B. Dragnea, "Influence of iron oleate complex structure on iron oxide nanoparticle formation," *Chem. Mater.*, vol. 19, no. 15, pp. 3624–3632, 2007.

[236] M. V Kovalenko, M. I. Bodnarchuk, R. T. Lechner, G. Nter Hesser, F. Schä, and W. Heiss, "Fatty acid salts as stabilizers in size-and shape-controlled nanocrystal synthesis: The case of inverse spinel iron oxide," *J. Am. Chem. Soc.*, vol. 129, pp. 6352–6353, 2007.

[237] G. Singh, H. Chan, A. Baskin, E. Gelman, N. Repnin, P. Král, and R. Klajn, "Self-assembly of magnetite nanocubes into helical superstructures," *Science*, vol. 345, no. 6201, pp. 1149-1153, 2014.

[238] J. Qin, S. Laurent, Y. S. Jo, A. Roch, M. Mikhaylova, Z. M. Bhujwalla, R. N. Müller, and M. Muhammed, "A high-performance magnetic resonance imaging T2 contrast agent," *Adv. Mater.*, vol. 19, no. 14, pp. 1874–1878, 2007.

[239] H. Yang, Y. Zhuang, Y. Sun, A. Dai, X. Shi Xiangyang, D. Wu, F. Li, H. Hu, and S. Yang, "Targeted dual-contrast T1- and T2-weighted magnetic resonance imaging of tumors using multifunctional gadolinium-labeled superparamagnetic iron oxide nanoparticles," *Biomaterials*, vol. 32, no. 20, pp. 4584–4593, 2011.

[240] Z. Zhou, Z. Zhao, H. Zhang, Z. Wang, X. Chen, R. Wang, Z. Chen, J. Gao, "Interplay between longitudinal and transverse contrasts in Fe3O4 nanoplates with (111) exposed surfaces," *ACS Nano*, vol. 8, no. 8, pp. 7976–7985, 2014.

[241] G. Salazar-Alvarez, J. Qin, V. Sepelak, I. Bergmann, M. Vasilakaki, K. N. Trohidou, J. D. Ardisson, W. A. A. Macedo, M. Mikhaylova, M. Muhammed, M. D. Baro, and J. Nogues, "Cubic versus spherical magnetic nanoparticles: The role of surface anisotropy," *J. Am. Chem. Soc.*, vol. 130, no. 40, pp. 13234–13239, 2008.